



HAL
open science

Regional terrestrial water storage and sea level variations inferred from satellite gravimetry

Wei W. Feng

► **To cite this version:**

Wei W. Feng. Regional terrestrial water storage and sea level variations inferred from satellite gravimetry. Earth Sciences. Université Toulouse III Paul Sabatier, 2014. English. NNT: . tel-01178195

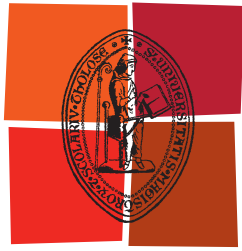
HAL Id: tel-01178195

<https://theses.hal.science/tel-01178195>

Submitted on 17 Jul 2015

HAL is a multi-disciplinary open access archive for the deposit and dissemination of scientific research documents, whether they are published or not. The documents may come from teaching and research institutions in France or abroad, or from public or private research centers.

L'archive ouverte pluridisciplinaire **HAL**, est destinée au dépôt et à la diffusion de documents scientifiques de niveau recherche, publiés ou non, émanant des établissements d'enseignement et de recherche français ou étrangers, des laboratoires publics ou privés.



Université
de Toulouse

THÈSE

En vue de l'obtention du

DOCTORAT DE L'UNIVERSITÉ DE TOULOUSE

Délivré par :

Université Toulouse 3 Paul Sabatier (UT3 Paul Sabatier)

Cotutelle internationale avec :

Institut de Géodésie et de Géophysique de l'Académie chinoise des sciences

Présentée et soutenue par :

Wei Feng

Le 14 Novembre 2014

Titre :

VARIATIONS RÉGIONALES DE STOCKAGE D'EAU TERRESTRE ET DE NIVEAU DE
LA MER DÉTECTÉES PAR GRAVIMÉTRIE SPATIALE

ED SDU2E : Sciences de la Terre et des Planètes Solides

Unité de recherche :

Géosciences Environnement Toulouse UMR 5563

Directeur(s) de Thèse :

Richard Biancale

Rapporteurs :

Pierre Exertier

Che-Kwan Shum

Autre(s) membre(s) du jury :

Isabelle Dadou (Présidente de Jury)

Isabelle Panet (Examinatrice)

Laurent Longuevergne (Examineur)

Richard Biancale (Directeur de Thèse) et Min Zhong (co-Directeur de Thèse)

Dedicated to my parents and my wife.

ACKNOWLEDGEMENTS

Firstly, I would like to thank my supervisors, Richard Biancale and Min Zhong, for their continuous encouragement, beneficial discussions and constructive suggestions throughout this research. I would like to thank Jean-Michel Lemoine for serving as a mentor and friend during my stay in Toulouse and throughout this research. It has been a privilege to work with him. His patience and guidance helped shape my research to a great extent. I would like to extend my gratitude and genuine appreciation to Prof. Houze Xu, another mentor in my research, for his patience and beneficial suggestions. I am very thankful to Benjamin Fong Chao, Che-Kwan Shum, Haoming Yan, Genyou Liu and Xiaoguang Hao for their expertise and help with various aspects of my study. I would like to thank Nicole Lestieu, Felix Perosanz and Stephane Bourgoigne for their help during my stay in CNES/GRGS. Thanks also go to Guoliang Cao and Chunmiao Zheng of Peking University, who provided me with their groundwater modeling results in the North China Plain. Additionally, Laurent Longuevergne of University of Rennes 1, Jiu Xia of Wuhan University, Jun Luo and Zebin Zhou of Huazhong University of Science and Technology, are acknowledged for their valuable suggestions and continuous support.

I would like to express my deepest appreciation and gratitude to my parents for their continuous support, encouragement and understanding over the years. Last but not least, I would like to thank my wife, Jianshuang for her endless support and love. Without her support, I could not have finished this thesis.

ABSTRACT

The Gravity Recovery and Climate Experiment (GRACE) is a joint satellite gravimetry mission between the National Aeronautics and Space Administration (NASA) and the German Aerospace Center (DLR), which provides the mean and time-varying global gravity fields. Since its launch in 2002, GRACE has proven to be an invaluable tool for monitoring the mass transport and redistribution in the Earth's fluid envelopes.

In this thesis, regional terrestrial water storage and sea level variations from GRACE are investigated. Groundwater storage variations (GWS) in North China are estimated from GRACE, and compared with in situ water table observations, groundwater model, and groundwater bulletins. Based on GWS estimates from GRACE and ground observations, seasonal groundwater variations in North China respond to the combined effect of anthropogenic irrigation (discharge of groundwater aquifers from spring to summer) and natural precipitation (recharge of groundwater aquifers from summer to winter). Interannual changes of groundwater from GRACE and ground observations agree well with year-over-year precipitation anomalies. The rate of groundwater depletion in North China based on GRACE and land surface models is 15.7 ± 2.4 mm/yr from 2003 to 2010, which is equivalent to a volume of 7.1 ± 1.0 km³/yr. However, the groundwater depletion rates in shallow aquifers according to in situ water table observations and groundwater bulletins are 1.2 and 2.0 km³/yr, respectively, which are significantly lower than the GRACE estimate. The difference in groundwater depletion rates estimated from GRACE, ground observations, and bulletins indicates the important contribution from deep aquifers in the plain and piedmont regions of North China, which has been underestimated until now.

In addition, GRACE detects obvious seasonal variations of seawater mass in the northern

shallow water of South China Sea (SCS), with an annual amplitude of 5.0 ± 0.4 cm. This seasonal variability of seawater mass is also validated by steric-corrected altimetry. In the deep ocean basin at the eastern part of SCS, to the west Luzon Island, seasonal sea level variations (SLV) observed by altimetry are dominated by the thermosteric SLV. The observed SLV in the East China Sea (ECS) and the Yellow Sea (YS) are also dominated by the thermosteric effect on seasonal timescales. Additionally, intra-seasonal mass variations in the ECS and YS are detected by GRACE, which also agree with steric-corrected altimetry. On interannual timescales, sea level fluctuations in the SCS are dominated by the thermosteric effect and driven by El Niño-Southern Oscillation (ENSO) events. By comparing the three observing systems over the SCS, i.e., altimetry, GRACE, and oceanographic measurements, a systematic drift problem after 2008 is identified in oceanographic datasets, which might result from the underestimation of steric SLV due to the poor sampling of temperature and salinity measurements in the shallow water of SCS. Especially, the problem would significantly hamper the steric SLV estimation when the ocean heating migrates from deep ocean basin to shallow coastal waters.

In the Red Sea, an annual amplitude of ~ 18 cm mass-induced SLV is detected from GRACE and steric-corrected altimetry from 2003 to 2011. The annual mass variations in the region dominate the mean SLV, and generally reach maximum in late January/early February. This seasonal variability of seawater mass is well explained by the water exchange between the Red Sea and the Gulf of Aden, which is driven by the seasonal reversal of monsoon. The annual steric component of the mean SLV in the Red Sea is relatively small and out of phase of the mass-induced SLV. In-situ bottom pressure records at the eastern coast of the Red Sea validate the high mass variability observed by steric-corrected altimetry and GRACE. In addition, the horizontal water mass flux of the Red Sea estimated from GRACE and steric-corrected altimetry is validated by hydrographic observations.

RÉSUMÉ

La mission GRACE (Gravity Recovery and Climate Experiment) est une mission spatiale conjointe entre la National Aeronautics and Space Administration (NASA) et le Centre aérospatial allemand (DLR), dédiée à l'observation du champ de gravité terrestre et de ses variations temporelles. Depuis son lancement en 2002, GRACE s'est avéré être un outil précieux pour la surveillance, à la fréquence mensuelle voire décadaire, des transferts de masse au sein du système Terre et de leur redistribution dans ses enveloppes fluides.

Dans cette thèse, les variations régionales de niveau d'eau sur des domaines continentaux et océaniques sont étudiées à l'aide de GRACE et d'autres types d'observations.

Pour ce qui est de la partie continentale, nous avons étudié les variations de stockage de l'eau souterraine dans les plaines du nord de la Chine. Les variations estimées à partir de GRACE sont comparées aux observations in situ de la nappe phréatique, à des modèles hydrologiques et aux bulletins officiels des organismes hydrographiques chinois. À partir de ces observations, nous établissons que les variations saisonnières des eaux souterraines en Chine du Nord répondent à l'effet combiné de l'irrigation d'origine anthropique (décharge des nappes aquifères du printemps à l'été) et des précipitations naturelles (recharge des nappes aquifères de l'été à l'hiver). Les modifications interannuelles des eaux souterraines vues par GRACE et les observations au sol sont en bon accord avec les anomalies de précipitations enregistrées sur cette zone. Le taux de déplétion des eaux souterraines dans le nord de la Chine, sur la base des modèles GRACE et des modèles hydrologiques, est de 15.7 ± 2.4 m/an de 2003 à 2010, ce qui équivaut à un volume de 7.1 ± 1.0 km³/an. Cependant, les taux d'épuisement des eaux souterraines dans les aquifères peu profonds, selon les observations in situ de la nappe phréatique et les bulletins officiels sur les eaux souterraines, sont seulement

de 1.2 et 2.0 km³/an respectivement, ce qui est nettement inférieur à l'estimation de GRACE. La différence dans les taux d'épuisement des eaux souterraines estimées à partir de GRACE, des observations au sol, et des bulletins indique la contribution importante des aquifères profonds dans les régions de plaine et de piémont de la Chine du Nord, qui était sous-estimée auparavant.

Pour ce qui est de la partie océanique, notre étude a porté sur deux zones bien distinctes : les mers de Chine et la mer Rouge. GRACE détecte d'évidentes variations saisonnières de la masse d'eau de mer dans la partie peu profonde du nord de la mer de Chine du Sud (SCS), avec une amplitude annuelle de 5.0 ± 0.4 cm. Cette variabilité saisonnière de la masse d'eau de mer est également corroborée par l'altimétrie corrigée de l'effet stérique. Dans la partie profonde de la SCS, en particulier à l'ouest de l'île de Luçon, les variations du niveau de la mer (SLV) saisonnières observées par altimétrie sont dominées par les SLV thermostériques. La SLV observée dans la mer de Chine orientale (ECS) et la mer Jaune (YS) sont également dominées par l'effet thermostérique aux échelles saisonnières. En outre, les variations de masse intra-saisonnières dans l'ECS et YS sont détectées par GRACE, en bonne corrélation avec l'altimétrie corrigée de l'effet stérique. Sur des échelles de temps interannuelles, les fluctuations du niveau de la mer dans la SCS sont dominées par l'effet thermostérique et entraînées par l'oscillation El Niño. En comparant les trois systèmes d'observation sur cette zone, c'est à dire l'altimétrie, GRACE et les mesures océanographiques, un problème de dérive systématique après 2008 a été identifié dans les données océanographiques. Cela pourrait résulter de la sous-estimation de la composante stérique en raison du mauvais échantillonnage de température et de salinité dans les eaux peu profondes de la SCS. En particulier, le problème pourrait affecter de manière significative l'estimation de la SLV stérique lorsque le chauffage de l'océan profond migre vers les eaux côtières peu profondes.

Pour la mer Rouge, une amplitude annuelle de SLV de ~ 18 cm d'origine massique est détectée à partir de GRACE et de l'altimétrie corrigée de l'effet stérique sur la période 2003-2011. La SLV dans la région est dominée par les variations de masse annuelles, le maximum étant généralement atteint fin janvier/début février. Cette variabilité saisonnière de la masse d'eau de mer est bien expliquée par l'échange d'eau entre la mer Rouge et le golfe d'Aden

qui est entraînée par le renversement saisonnier de la mousson. La composante stérique annuelle de la SLV dans la mer Rouge est relativement petite et en opposition de phase avec la composante massique. Les enregistrements des capteurs de pression fond de mer sur la côte orientale de la mer Rouge permettent de valider les variations élevées de masse observées par l'altimétrie et GRACE. En outre, le flux horizontal de masse d'eau de la Mer Rouge estimé à partir de GRACE et de l'altimétrie corrigée de l'effet stérique est corroboré par des observations courantométriques in situ dans le détroit de Bab-el-Mandeb.

TABLE OF CONTENTS

Table of contents	xiii
List of figures	xvii
List of tables	xxi
1 Introduction	1
1.1 Terrestrial Water Storage Variations from GRACE	4
1.2 Global Sea Level Variations from Altimetry and GRACE	8
1.3 Outline of the Thesis	12
2 Methodology	15
2.1 Basics of Temporal Gravity Field	15
2.2 Post-processing Methods	17
2.2.1 Gaussian Smoothing	17
2.2.2 Destriping Methods	21
2.2.3 GRACE Measurement Error	23
2.2.4 Basin-scale Mass Variations from Temporal Gravity Field	24
2.3 Combination of Altimetry, GRACE and Oceanographic Data	30
2.3.1 Steric Sea Level Variations	30
2.3.2 Glacial Isostatic Adjustment	31
2.3.3 Elastic Loading Deformation	32
2.3.4 Inverted Barometer Corrections	33

Table of contents

2.3.5	Boussinesq Approximation	35
2.4	Summary	36
3	Groundwater Storage Variations in North China from GRACE	37
3.1	Introduction	37
3.2	Data and Methods	39
3.2.1	GRACE Data and Processing	39
3.2.2	Land Surface Models	42
3.2.3	Ground-based Measurements	43
3.2.4	Groundwater Model	44
3.3	Results	44
3.3.1	Seasonal GWS Variations	47
3.3.2	Interannual GWS Variations	48
3.3.3	Long-term GWS Variations	58
3.3.4	Error Estimation of GRACE-based GWS Variations	62
3.3.5	Discussion	67
3.3.6	Summary	70
4	Regional Sea Level Variations from GRACE	73
4.1	Introduction	73
4.2	Sea Level Variations in China Seas	74
4.2.1	Data	74
4.2.2	Study Region	77
4.2.3	Spatial Patterns of Seasonal Sea Level Variations in China Seas	78
4.2.4	Sea Level Variations in the South China Sea	82
4.2.5	Sea Level Variations in the East China Sea and Yellow Sea	97
4.2.6	Discussion and Summary	102
4.3	Sea Level Variations in the Red Sea	105
4.3.1	Introduction	105
4.3.2	Data and Processing	107

4.3.3	GRACE Data	107
4.3.4	Steric-corrected Altimetry Data	110
4.3.5	Bottom Pressure Records	111
4.3.6	Results and Discussion	111
4.3.7	Summary	120
5	Conclusions and Future Work	121
5.1	Conclusions	121
5.2	Future Work	122
	References	125

LIST OF FIGURES

1.1	An overview of mass transport, mass variations, and mass exchange in the Earth system	2
1.2	A schematic diagram of the twin GRACE satellites in orbit and internal view of GRACE satellite instruments	2
1.3	Global trend map of mass variations during 2003-2012 from GRACE	3
1.4	The area equipped for irrigation with groundwater	7
1.5	Estimated, observed, and projected global sea level rise from 1800 to 2100	10
1.6	Spatial trend pattern of global sea level change observed by satellite altimetry from 1993 to 2013	10
1.7	Global sea level variations from altimetry, GRACE, and Argo during 2005-2012	12
2.1	Relations among filtered/unfiltered changes of surface mass density in terms of EWH, filtered/unfiltered geoid, and their SH coefficients.	20
2.2	Spatial pattern of mass variations in October 2013 from GRACE Stokes coefficients	23
2.3	Spatial patterns of GRACE measurement error in November 2011	24
2.4	Standard deviation of ocean mass changes from GRACE during 2003-2011	29
2.5	Synthesis of basin-scale mass variation estimation and error estimation from Stokes coefficients of GRACE temporal gravity fields	30
2.6	GIA mass rate and uplift rate with SH expansion up to degree 100	32
2.7	Vertical loading deformation in the sea bottom in January 2003 based on GRACE-observed ocean mass variations in the same month	33

List of figures

2.8	Time-varying mass of the atmosphere averaged over the ocean based on GRACE GAD data	35
2.9	Boussinesq correction for the steric SLV based on the temperature and salinity data from the ECCO ocean model	36
3.1	Location and shaded relief topography of North China	39
3.2	Trend map of TWS changes in China and its surrounding regions from GRACE during 2002-2013	45
3.3	The area equipped for irrigation with groundwater in North China	46
3.4	TWS variations estimated from GRACE and SMS+SWES variations estimated from LSMs	46
3.5	Monthly GWS variations estimated from GRACE minus LSMs and monthly groundwater level changes observed by monitoring wells	47
3.6	Seasonal monthly variations of groundwater storage, groundwater level, and precipitation in the study region	48
3.7	Interannual GWS variations from GRACE minus LSMs and groundwater level changes observed by monitoring wells	49
3.8	Yearly GWS variations, GWS depletion and precipitation anomalies	50
3.9	Spatial patterns of yearly groundwater level variations from groundwater monitoring wells	53
3.10	Spatial pattern of specific yields in the North China Plain	54
3.11	Spatial patterns of yearly GWS variations from groundwater monitoring wells	55
3.12	Spatial patterns of yearly GWS variations from groundwater monitoring wells at GRACE resolution	56
3.13	Spatial patterns of yearly GWS variations from GRACE minus LSMs	57
3.14	Spatial patterns of yearly GWS variations from groundwater model	58
3.15	Spatial patterns of GWS trends over 2002-2013	59
3.16	Spatial patterns of GWS trends over 2002-2008	60
3.17	Locations of cities in the North China Plain	61
3.18	Groundwater level changes in cities of the North China Plain	61

3.19	Interannual GWS variations from CSR, GFZ, JPL, and GRGS GRACE minus LSMs	66
3.20	Spatial patterns of GWS trends estimated from CSR, GFZ, and JPL GRACE products from 2002 to 2013	67
3.21	Spatial patterns of GWS trends from CSR and GRGS GRACE products from 2003 to 2012	67
4.1	Spatial pattern of annual global ocean mass change observed by GRACE from 2003 to 2012	74
4.2	Selected study regions in China seas	77
4.3	Annual amplitude and phase of SLV from altimetry, Ishii, and GRACE during 2003-2012	79
4.4	Spatial patterns of correlation coefficients	80
4.5	Spatial patterns of seasonal SLV in China seas from altimetry, Ishii, GRACE, and “Ishii+GRACE” during 2003-2012	81
4.6	Time series of SLV in the SCS during 1993-2012	84
4.7	Time series of SLV in the NSCS during 1993-2012	85
4.8	Time series of SLV in the NSCS during 1993-2012	86
4.9	Interannual time series of SLV in the SCS during 1993-2012 and lagged correlation coefficients between SLV and NINO4 index	89
4.10	Interannual time series of SLV in the SCS during 1993-2012	92
4.11	Trend maps of total SLV from altimetry and steric SLV from Ishii in the SCS over three different time periods	93
4.12	Interannual time series of SLV in the SCS during 2003-2012	95
4.13	Trend maps of total SLV, steric SLV, and mass-induced SLV in the SCS during 2003-2012	96
4.14	Time series of SLV in the ECS during 1993-2012	99
4.15	Time series of SLV in the YS during 1993-2012	100
4.16	Interannual time series of SLV in the ECS and YS during 1993-2012	101
4.17	Map of Red Sea and its seasonal exchange regime	107

List of figures

4.18	Annual amplitude of mass-induced SLV in the Red Sea from steric-corrected altimetry and GRACE	112
4.19	Time series of seawater mass variations in the Red Sea from steric-corrected altimetry and GRACE	114
4.20	Coherences between steric-corrected altimetry and GRGS, steric-corrected altimetry and CSR, and GRGS and CSR at different frequencies	115
4.21	Time series of OBP along the Saudi Arabian coast of Red Sea measured by BPRs and GRACE	117
4.22	The climatological monthly horizontal water mass fluxes in the Red Sea estimated from steric-corrected altimetry, GRACE, and hydrographic observations	119

LIST OF TABLES

3.1	Groundwater depletion rates in the North China Plain	51
3.2	Yearly precipitation anomalies and yearly groundwater depletion in the North China Plain	51
3.3	Scaling factors for rescaling TWS time series	64
3.4	GRACE data processing error of applying Gaussian smoothing with different radii and applying different destriping methods	65
3.5	Scaling factors for rescaling GWS time series	65
3.6	Different error components in the final error budget	66
4.1	Annual amplitudes and phases of SLV in the SCS, NSCS, and ESCS during 1993-2012	87
4.2	Annual amplitudes and phases of SLV in the SCS, NSCS, and ESCS during 2003-2012	87
4.3	Trends of total SLV from altimetry and steric SLV from Ishii in the SCS in different time periods	93
4.4	Trends of SLV in the SCS, NSCS, and ESCS during 2003-2012	97
4.5	Annual amplitudes and phases of SLV in the ECS and YS during 1993-2012 .	102
4.6	Annual amplitudes and phases of different SLV components in the Red Sea from 2003 to 2011	116

INTRODUCTION

Sea level variations (SLV), melting of polar ice caps and mountain glaciers, extreme droughts and floods - these and those issues of global climate change are closely related to the mass variations on the Globe. Detailed knowledge on mass transport and redistribution among continents, oceans, atmosphere and cryosphere will help us better understand the physics of global climate change (Figure 1.1). Since the last two decades, modern space geodesy have developed dramatically. A series of altimetry satellites (e.g., TOPEX/Poseidon, Jason-1/2, ERS-1/2, Envisat) bring the revolutionary changes in understanding the spatial and temporal variations of global sea surface height [Fu and Cazenave, 2001]. High-precision GPS observations not only record the displacement information of ground motion, but also provide the surface water storage variations based on the elastic loading theory [Argus et al., 2014; Kusche and Schrama, 2005; Wu et al., 2003]. The Ice, Cloud and land Elevation Satellite (ICESat) mission provides the surface height observations of ice caps and mountain glaciers in different laser altimeter campaigns, which can be used to deduce the surface mass variations with the firn density data [Gunter et al., 2009; Schutz et al., 2005].

Launched in March 2002, the Gravity Recovery and Climate Experiment (GRACE) satellite mission has provided the direct observations of global gravity field and its temporal variations with an unprecedented accuracy [Tapley et al., 2004]. As a joint satellite mission between the National Aeronautics and Space Administration (NASA) and the German Aerospace Center (DLR), GRACE has proven to be an invaluable tool for monitoring the mass transport and redistribution in the Earth's fluid envelopes. To measure the Earth's gravity field from space,

Introduction

two GRACE satellites fly at an altitude of ~ 450 km in the same near polar orbit with one 220 km ahead of the other. Any mass variation in the Earth's surface, in principle, will cause the change of distance between two GRACE satellites, which will be detected at μm precision. Thus, by observing the distance between two satellites by the K-band ranging (KBR) instrument and orbit perturbations by GPS tracking, GRACE satellites can "sense" the gravity field and its variations in a direct way. Figure 1.2 demonstrates the schematic diagram of GRACE satellites and the instruments.

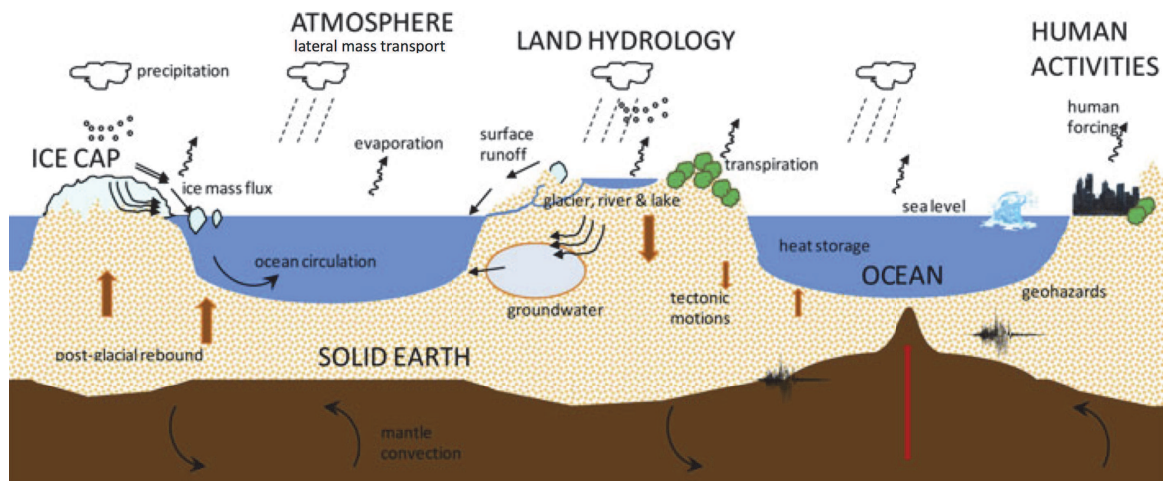


Figure 1.1: An overview of mass transport, mass variations, and mass exchange in the Earth system (From: Panet et al. [2013]).

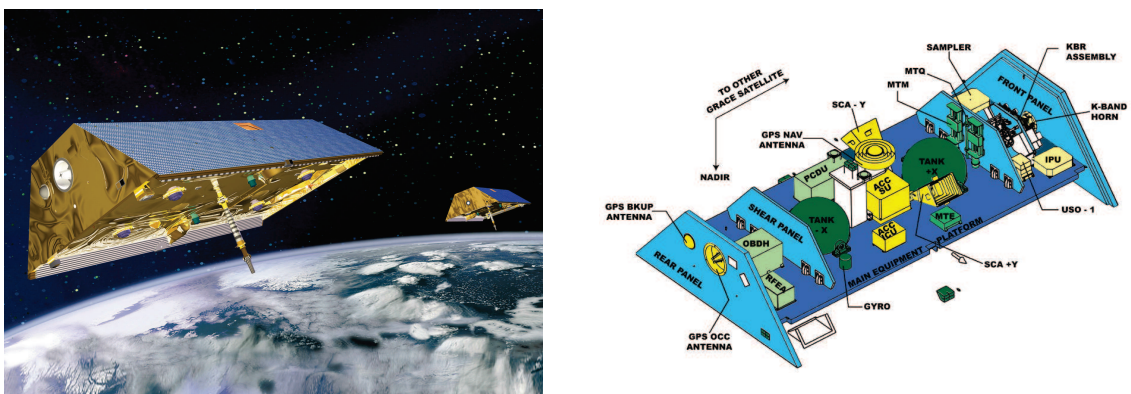


Figure 1.2: (Left) A schematic diagram of the twin GRACE satellites in orbit. (Right) Internal view of GRACE satellite instruments. (From: <http://www.csr.utexas.edu/grace/>)

Figure 1.3 shows the global trend map of mass variations observed by GRACE during 2003-2012. Numerous studies have demonstrated that GRACE has gained many achievements in Earth science, e.g., terrestrial water storage (TWS) variations and relevant droughts and floods in the Amazon River basin [Becker et al., 2011; Chen et al., 2010a, 2009b; Frappart et al., 2012; Tapley et al., 2004], ice sheet mass balance in Antarctica and Greenland [Chen et al., 2009a; King et al., 2012; Ramillien et al., 2006; Schrama et al., 2014; Shepherd et al., 2012; Velicogna and Wahr, 2006a,b; Williams et al., 2014], mass balance in High Mountain Asia [Jacob et al., 2012; Matsuo and Heki, 2010; Yi and Sun, 2014], groundwater storage depletion in northern India [Rodell et al., 2009; Tiwari et al., 2009], mass-induced global sea level variations [Boening et al., 2012; Cazenave et al., 2009; Chambers, 2006; Fasullo et al., 2013; Leuliette and Miller, 2009; Willis et al., 2008], and coseismic and post-seismic gravity change caused by the 2004 Sumatra-Andaman Earthquake [Chen et al., 2007a; Han et al., 2006; Panet et al., 2007]. Considering the tremendous success of GRACE mission and its unique contribution to geodesy, hydrology, oceanography, and glaciology, the new U.S.-German GRACE Follow-On satellites are scheduled to launch in 2017, to ensure the continuity of the GRACE data with a potential higher accuracy by taking advanced laser ranging instruments (<http://gracefo.jpl.nasa.gov/>).

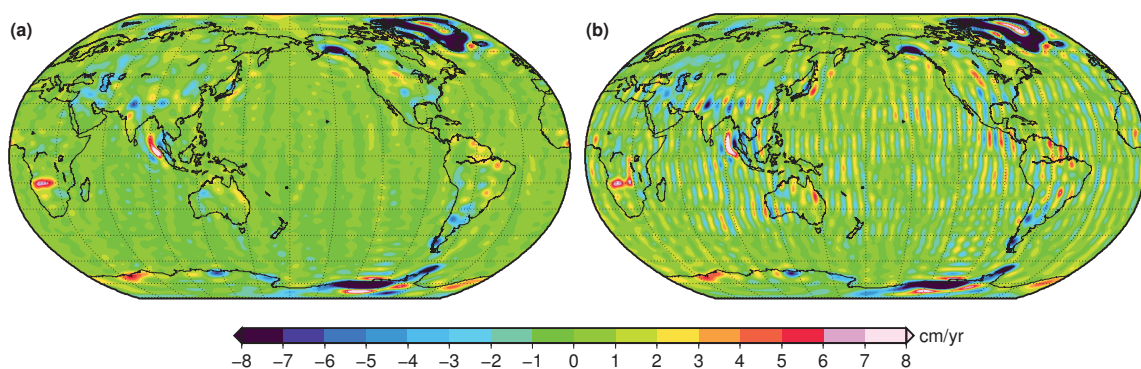


Figure 1.3: Global trend map of mass variations during 2003-2012 from (a) GRGS RL03 and (b) CSR RL05 GRACE solutions. North-south “strips” caused by correlated errors in GRACE Stokes coefficients are suppressed in GRGS solutions thanks to the stabilization applied in the gravity inversion [Bruinsma et al., 2010; Lemoine et al., 2007]. Glacial Isostatic Adjustment (GIA) effect has been removed.

1.1 Terrestrial Water Storage Variations from GRACE

As a major component of global water cycle, terrestrial water is defined as an integrated measure of all forms of water stored on and below the surface of the Earth, which includes surface water, soil moisture and permafrost, groundwater, snow and ice, and wet biomass. Early, based on some simulations from hydrological, oceanic, and atmospheric models, Wahr et al. [1998] validated the detectability of TWS variation signal using GRACE and proposed the basic method for constructing mass variations from the GRACE gravity coefficients. Later, Swenson and Wahr [2002] devised spatial averaging kernels to extract regional mass variations from GRACE. Since its launch in 2002, GRACE has proven to be an extremely useful tool for observing TWS variations [Tapley et al., 2004; Wahr et al., 2004]. As the largest drainage basin in the world, Amazon River basin exhibits large-scale TWS variations, which is prone to be observed by GRACE firstly [Tapley et al., 2004]. Significant seasonal variability of TWS in the Amazon River basin was detected by GRACE, and was in general agreement with the predictions of a hydrological model [Wahr et al., 2004]. With the increase of GRACE observations and the improvement of data processing methods, interannual variations of TWS in the Amazon River basin are further validated based on GRACE observations. The drought events in 2005 and 2010 and the flood in 2009 in the Amazon River basin are detected by GRACE [Chen et al., 2010a, 2009b; Feng et al., 2012; Frappart et al., 2012]. By comparing with in situ river level records, precipitation observations, and hydrological models, GRACE has proven to successfully capture both seasonal and interannual variations of TWS in the Amazon River basin [Alsdorf et al., 2010; Becker et al., 2011; Xavier et al., 2010; Zeng et al., 2008]. Additionally, GRACE-observed TWS variations even have the potential to improve the fire forecasts for the southern Amazon [Chen et al., 2013]. Besides the Amazon river basin, GRACE also detects hydrological signals in many parts of the world, e.g., the Congo River basin [Crowley et al., 2006], the Lower Ob basin [Frappart et al., 2010], the Yangtze River basin [Hu et al., 2006; Zhong et al., 2009], the Illinois and Texas of U.S. [Long et al., 2013; Swenson et al., 2006], the East African great lakes region [Becker et al., 2010], the North America and Scandinavia [Wang et al., 2013], and the central Europe [Andersen et al., 2005].

Groundwater, soil water and surface water are three main components of terrestrial water. With the development of remote sensing and the increase of ground observation data, surface water and soil water can be observed or modeled at different spatial and temporal resolutions [Crétau et al., 2011; Famiglietti, 2004; Kerr et al., 2001; Rodell et al., 2004; Sheffield et al., 2009]. As an important component of global water cycle, groundwater is a vital source of fresh water for agriculture, industry, public supply, and ecosystems in many parts of the world. However, there are no extensive ground-based networks for monitoring large-scale groundwater storage (GWS) variations. Globally, groundwater provides more than 50% of drinking water, 40% of industrial water, and 20% of irrigation water [Zektser and Everett Lorne, 2004]. Over-exploitation of groundwater has resulted in groundwater depletion and pollution as well as soil salinization and land subsidence, particularly in places where groundwater-based irrigation is intensive, such as in the North China Plain (NCP), northern India, and the central United States [Scanlon et al., 2007; Shah et al., 2000; Wada et al., 2010]. However, information regarding the spatial and temporal variability of GWS is extremely limited [Shah et al., 2000]. The impact of groundwater on global water cycle is still veiled. Preliminary study indicates that global groundwater depletion rate since 2000 is $\sim 145 \text{ km}^3/\text{yr}$ (equivalent to 0.40 mm/yr of sea-level rise, or 13% of the reported rate of 3.1 mm/yr) [Konikow, 2011]. However, Wada et al. [2012]'s results show that the contribution of groundwater depletion to sea-level rise is about $0.57 \pm 0.09 \text{ mm/yr}$ in 2000, which is significant larger than that from Konikow [2011]. The latest estimate based on WaterGAP global hydrological model from Döll et al. [2014] is $113 \text{ km}^3/\text{yr}$ (equivalent to 0.31 mm/yr of sea-level rise) for the period 2000-2009, which is smaller than other two estimates derived from different global hydrological modeling [Konikow, 2011; Wada et al., 2012]. So the modeling uncertainties of global groundwater depletion rate remain high.

In a prelaunch study, Rodell and Famiglietti [2002] evaluated the GRACE's potential for isolating changes in the groundwater component of TWS in the High Plains aquifer of the central United States. After its launch, numerous studies have shown that GRACE can be used to detect large-scale GWS changes in many parts of the world. Rodell et al. [2007] and Strassberg et al. [2007] isolated GWS anomalies from GRACE-derived total TWS and soil

moisture storage variations simulated from Land Surface Models (LSMs) for the Mississippi River basin and High Plains Aquifer. They found good correspondence in these areas between GRACE-LSMs estimates and those derived from monitoring well-based observations. When ground soil moisture measurements are available, GWS can be estimated more independently after removing monitored SM from GRACE-derived TWS. Yeh et al. [2006], Swenson et al. [2008a] and Strassberg et al. [2009] estimated GWS variations in Illinois, Oklahoma and High Plains using GRACE and ground soil moisture measurements, and found good agreement between GRACE-derived GWS and monitoring well level data.

The early studies mainly focus on seasonal GWS variations using GRACE. However, with the increase of GRACE observations, more attention are paid to long-term large-scale GWS variations. In northern Indian, more than 75% of irrigation water stems from groundwater. Rodell et al. [2009] found that groundwater in this region was being depleted at a mean rate of 4.0 ± 1.0 cm/yr during 2002-2008, which is equivalent to 17.7 ± 4.5 km³/yr in volume. They concluded that this unsustainable consumption of groundwater resulted from irrigation and other anthropogenic uses in this region. Tiwari et al. [2009] extended the study area to the whole northern India, and found a GWS loss at a rate of 54 ± 9 km³/yr during 2002-2008. California's Central Valley is one of the most highly-productive agricultural areas in US, where groundwater supplies the bulk of the irrigation water. In particular during the drought conditions prevailing in the Central Valley over 2006-2009, groundwater is over-exploited. Although the area of the Central Valley (52,000 km²) is below spatial resolution of GRACE footprint ($\sim 200,000$ km²), the large GW mass variations in the aquifer are still detected by GRACE [Famiglietti et al., 2011; Scanlon et al., 2012]. From 2006 to 2010, the annual decline rate of GWS in the Central Valley is about 8.9 ± 0.8 km³/yr [Scanlon et al., 2012]. Additionally, in the Middle East, where ground observations are severely limited, GRACE is able to provide valuable GWS estimates. From 2003 to 2009, GWS declined by 91.3 ± 10.9 km³ in the north-central Middle East [Voss et al., 2013]. In this region, the largest groundwater depletion occurs in Iran, with a decline rate of 25 ± 3 km³/yr [Joodaki et al., 2014]. Based on a priori spatial patterns of TWS variations from hydrological models and surface reservoir water storage variations from altimetry, Forootan et al. [2014] further studied the GRACE-based

GWS variations over six basins of Iran using the Independent Component Analysis (ICA) method. They concluded that the largest GWS decline was located in the Urmia basin, i.e., the northwestern Iran.

Figure 1.4 shows the percentage of each 5 arc min grid cell equipped for irrigation with groundwater globally [Siebert et al., 2010]. As mentioned above, numerous studies have demonstrated that GRACE can detect seasonal and long-term GWS changes in many heavily groundwater-based irrigated areas shown in Figure 1.4, such as in northern India and Pakistan [Rodell et al., 2009; Tiwari et al., 2009], the High Plains aquifer [Strassberg et al., 2007, 2009], the Central Valley [Famiglietti et al., 2011; Scanlon et al., 2012], and the alluvial aquifer along the Mississippi River in the United States [Rodell et al., 2007]. In Figure 1.4, irrigation in North China also heavily relies on groundwater, which motivates us to study the GWS variations in North China from GRACE in depth.

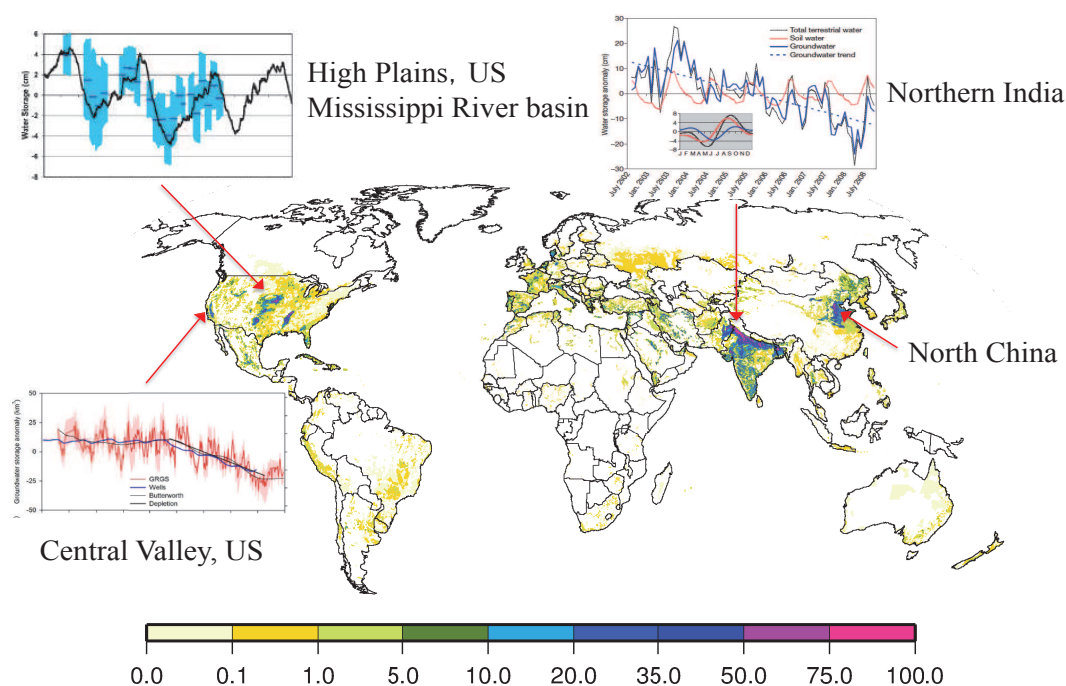


Figure 1.4: The area equipped for irrigation with groundwater, given as a percentage of cell area, for $5' \times 5'$ cells [Siebert et al., 2010]. The high percentages of area equipped for irrigation with groundwater are shown in Central Vally, High Plains, Mississippi River basin, northern India, and North China.

1.2 Global Sea Level Variations from Altimetry and GRACE

By defining the sea level relative to the Earth's geocenter (i.e., geocentric sea level), the physical causes of sea level change can be expressed as either the ocean volume change or ocean-basin shape change [Willis et al., 2010]. Changes of ocean-basin shape mainly result from the Glacial Isostatic Adjustment (GIA) effect, which is the Earth's viscoelastic response to the last deglaciation [Lambeck and Nakiboglu, 1984; Peltier, 1986]. GIA effect causes a net sinking of ocean basin relative to the Earth's geocenter, which would imply, if the surface of the sea remained at a constant distance to the center of the Earth, a globally averaged sea level rise rate of 0.3 mm/yr [Peltier, 2009]. Usually, this effect is therefore added to global sea level change observed by altimetry and tide gauges. So, in a general sense, global sea level change refers to the changes in the ocean's volume.

Global mean sea level (GMSL) change results from two major processes: (i) thermal expansion caused by heating of the global ocean (i.e., thermosteric sea level), and (ii) ocean mass change caused by the exchange of water between oceans and other reservoirs (i.e., glaciers and ice caps, ice sheets, and other land water reservoirs) [IPCC AR5, 2013]. Although haline effects might be significant in some regional ocean, the globally averaged salinity content stay relatively constant [Antonov et al., 2002; Munk, 2003]. Thus, the net increase of ocean heat content and the freshwater imports from continents are the two dominant reasons of global sea level rise.

Based on tide gauge measurements, global sea level rise rate over the 20th century is about 2 mm/yr, as released by the latest IPCC Fifth Assessment Report (AR5) [2013]. However, the number and spatial distribution of tide gauge observations are highly limited [Mitchum et al., 2010]. In addition, since tide gauge observes the sea level variations relative to the land, the crustal deformation in the tide gauge station need to be estimated, which is still difficult for many tide gauge stations. Figure 1.5 shows the estimated, observed, and projected global sea level rise from 1800 to 2100 [Shum et al., 2008; Willis et al., 2010], which exhibits a significant acceleration in sea level rise since about 1900. Since early 1990s, satellite altimetry provides a high coverage of the spatial and temporal variations of the sea level globally. The GMSL rise

rate during 1993-2013 observed by satellite altimetry is about 3.2 mm/yr. This GMSL rise rate is relatively stable since 1993 [Ablain et al., 2009; Cazenave et al., 2009; Kuo, 2006; Leuliette and Scharroo, 2010; Nerem et al., 2010; Shum et al., 2008; Willis et al., 2010]. Although the quality and quantity of sea level observations have improved significantly in recent two decades, the projected sea level rise remains controversial, especially from semi-empirical models [Gregory et al., 2006; Grinsted et al., 2010; Holgate et al., 2007; Rahmstorf, 2007; Schmith et al., 2007; Taboada and Anadon, 2010; Vermeer and Rahmstorf, 2009, 2010].

It is worth noting that the global sea level rise rate is inhomogeneous in spatial domain [Cazenave and Llovel, 2010]. As shown in Figure 1.6a, in some regions, such as the Western Pacific Ocean, sea level rises rapidly; while in the eastern coast of Northern Pacific Ocean, sea level falls. Additionally, sea level exhibit rise and drop alternately in oceans, where there are high-speed currents, e.g., Kuroshio Current, Gulf Stream, and Antarctic Circumpolar Current. When the global mean sea level rise rate of 3.2 mm/yr is removed, the nonuniform distribution of regional sea level trends relative to GMSL rise is further highlighted (Figure 1.6b). For example, sea level rise rate in the warm pool region of the Western Pacific Ocean is significantly larger than the global mean value. Keep in mind that this inhomogeneous pattern of sea level rise rate also contains the response of sea level to climate change events on interannual to decadal timescales, e.g., El Niño-Southern Oscillation (ENSO), North Atlantic Oscillation (NAO), and Pacific Decadal Oscillation (PDO). Thus, it is worthwhile to analyze the nonuniform sea level change in different ocean regions.

Although altimetry provides the temporal and spatial variations of global sea level, it is not able to isolate the steric sea level variations (SLV) and mass-induced SLV. Steric SLV can be calculated from ocean temperature and salinity data based on oceanographic observations or ocean models [Fukumori, 2002; Ishii et al., 2006; Levitus et al., 2005]. The Argo project is a global ocean observing system for measuring temperature and salinity in the Earth's oceans since the early 2000s [Guinehut et al., 2004; Hadfield et al., 2007; Roemmich and Owens, 2000]. Since 2007, the Argo array contains more than 3000 high-quality temperature and salinity profiles in or near real time, which significantly improve the coverage of global oceanographic observations (<http://www.argo.ucsd.edu/>).

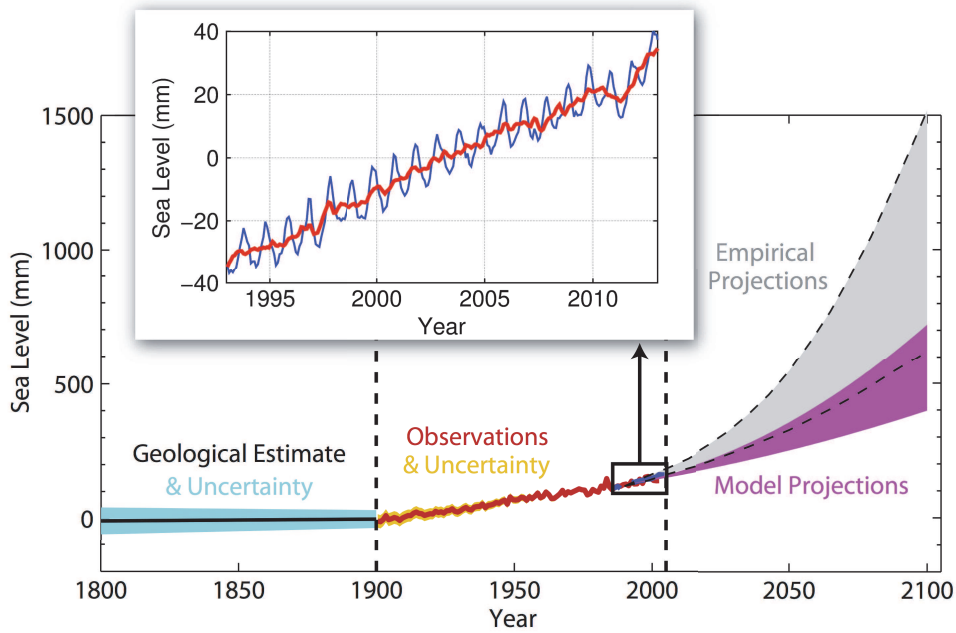


Figure 1.5: Estimated, observed, and projected global sea level rise from 1800 to 2100, modified from Willis et al. [2010] and Shum et al. [2008]. Pre-1900 estimates are based on geological interpretations [Lambeck et al., 2002]. The tide gauge record is shown from 1900 to 2005 (red, from Church and White [2006]), and the satellite altimetry record is shown from 1985 to 2005 (blue, from Kuo [2006]). The projected twenty-first century sea level rise of 26-59 cm is based on coupled climate models using the A1F1 scenario (pink envelope, from IPCC, [2007]). The projected sea level rise from semi-empirical methods (50-140 cm) is much higher than that from IPCC AR4 [Rahmstorf, 2007]. The inset shows global mean sea level rise from satellite altimetry from 1993 to 2013 (blue). Red curve shows interannual variations of global mean sea level with seasonal cycles removed and a 3-month moving average applied. GIA correction of -0.3 mm/yr is removed.

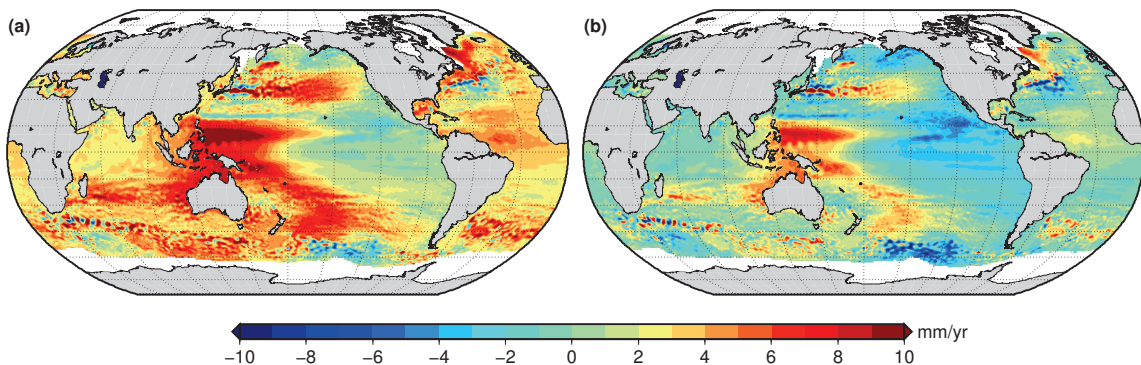


Figure 1.6: (a) Spatial trend pattern of global sea level change observed by satellite altimetry from 1993 to 2013. (b) Same as (a), but a uniform global mean sea level rise rate of 3.2 mm/yr is removed.

Besides the steric SLV, the mass-induced SLV is the other important component of global sea level change. The way to directly observe ocean mass variations is to measure the pressure of the water column and the overlaying atmosphere on the ocean floor, i.e., the ocean bottom pressure (OBP) [Ponte, 1999]. However, the sparse distribution of in situ OBP observations in the ocean and the systematic drift problem over time extremely limit the application of OBP records in estimating long-term ocean mass variations [Chambers and Schroter, 2011]. Since 2002, GRACE provides the direct observations of mass-induced SLV from space. Firstly, Chambers et al. [2004] estimated the seasonal ocean mass variations from GRACE, and validated this seasonal variability with steric-corrected altimetry and model results [Chen et al., 1998; Minster et al., 1999]. With the increase of observations from altimetry, GRACE, and Argo, subsequent studies have mainly focused on the global sea level budget, i.e., total SLV from altimetry should equal the sum of the steric SLV from Argo and mass-induced SLV from GRACE. Lombard et al. [2007] found that the rate of global steric SLV inferred from altimetry minus GRACE was 1.9 ± 0.2 mm/yr over the period 2002-2006. However, in contrast, the steric SLV estimated from the Ishii oceanographic dataset exhibits a negative slope, i.e., -2.8 ± 0.2 mm/yr, over the same period. A net loss of $3.2 (\pm 1.1) \times 10^{22}$ J of ocean heat content is also claimed to be found between 2003 and 2005 from in situ oceanographic measurements [Lyman et al., 2006]. Later, further studies indicate that there exist systematic errors in Argo profiles and expendable BathyThermograph (XBT) data [Ishii and Kimoto, 2009; Willis et al., 2007, 2009]. However, after removing these errors from oceanographic observations, Willis et al. [2008] still found significant trend differences among the three observing systems, i.e., altimetry, GRACE, and Argo. In their study, the observed GMSL rise rate from altimetry was 3.6 ± 0.8 mm/yr from 2003 to 2007; however, the estimate from GRACE and Argo was 0.3 ± 0.6 mm/yr for the same period. However, Leuliette and Miller [2009] found a closed sea level rise budget from 2004 to 2007. Their analysis showed that a sum of steric SLV and mass-induced SLV has a trend of 1.5 ± 1.0 mm/yr, in agreement with the total sea level rise rate observed by altimetry (2.4 ± 1.1 mm/yr). Leuliette and Miller [2009] concluded that the poor Argo sampling before mid-2004 may result in the underestimation of steric sea level rise rate in the study of Willis et al. [2008]. Cazenave et al. [2009] also found a closed sea level bud-

get from 2003 to 2008, but adopted a GIA correction of 2 mm/yr from Peltier [2009], which was proved to be overestimated [Chambers et al., 2010]. [Chambers et al., 2010] concluded that the Paulson et al. [2007] GIA model is more appropriate for correcting GRACE-observed ocean mass variations. After adopting this GIA model and the latest altimetry, GRACE, and Argo data, the sea level budget is closed in most recent studies [Boening et al., 2012; Chambers et al., 2010; Leuliette and Willis, 2011]. As shown in Figure 1.7, the sum of ocean mass variations from GRACE and steric SLV from Argo agrees closely with the observed GMSL change from altimetry. It is important noting that there is a V-shaped GMSL change from 2010 to 2011, which is mainly caused by terrestrial water storage anomalies related to the 2010/11 La Niña event [Boening et al., 2012; Fasullo et al., 2013].

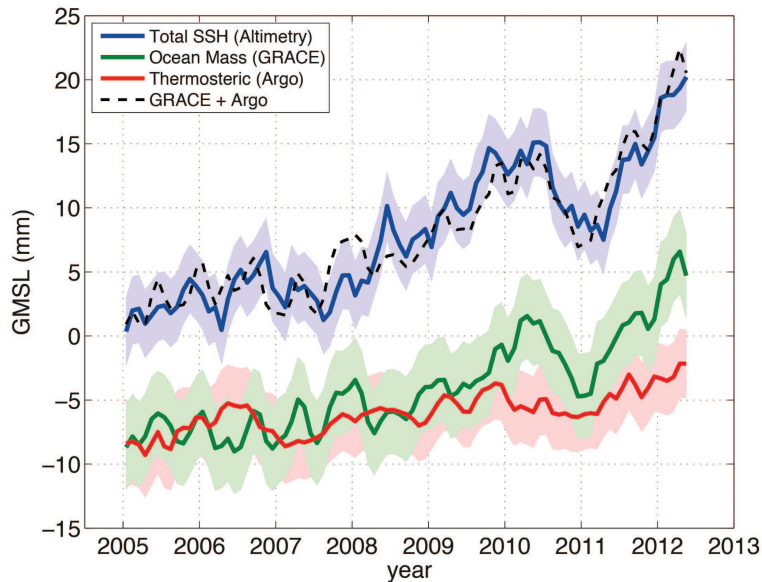


Figure 1.7: Global mean sea level from altimetry during 2005-2012 (blue). Ocean mass variations from GRACE are shown in green and steric SLV from Argo are shown in red. The black dash line shows the sum of ocean mass variations and steric SLV. (Updated from Boening et al. [2012])

1.3 Outline of the Thesis

This thesis comprises five chapters. Besides the current Introduction Chapter, the rest of the thesis is organized as follows.

Chapter 2 introduces the basic principle of temporal gravity fields and describes the post-processing methods for GRACE Stokes coefficients. Regional mass variation estimation, leakage and bias corrections, and error assessment are summarized as well. In addition, the steric sea level variations calculation and relevant notice in combining altimetry, GRACE and oceanographic data are described.

Chapter 3 evaluates the groundwater storage variations (GWS) in North China from GRACE, and compares the estimates with in situ water table observations, groundwater bulletins and groundwater model. Effects of anthropogenic irrigation and natural precipitation to GWS variations are discussed on seasonal and interannual timescales. The uncertainty of GRACE-based GWS variations is assessed in detail.

Chapter 4 discusses sea level variations in China seas (i.e., South China Sea, East China Sea and Yellow Sea) and in the Red Sea from altimetry, GRACE and oceanographic observations.

Chapter 5 concludes the study with recommendations for future studies.

METHODOLOGY

2.1 Basics of Temporal Gravity Field

In general, global gravity field is defined as the shape of geoid, which is the equipotential surface that coincides with mean sea surface height. The geoid can be expressed as a sum of spherical harmonics [see, e.g., Chao and Gross, 1987]:

$$N(\theta, \lambda) = a \sum_{l=0}^{\infty} \sum_{m=0}^l \tilde{P}_{lm}(\cos \theta) [C_{lm} \cos(m\lambda) + S_{lm} \sin(m\lambda)] \quad (2.1)$$

where a , θ , λ are Earth's radius, co-latitude and longitude, respectively; l , m are degree and order; C_{lm} , S_{lm} are spherical harmonic (SH) coefficients (i.e., Stokes coefficients); and $\tilde{P}_{lm}(\cos \theta)$ are fully normalized associated Legendre functions.

The temporal variation of geoid (ΔN) can also be represented as changes of SH coefficients (ΔC_{lm} , ΔS_{lm}):

$$\Delta N(\theta, \lambda) = a \sum_{l=0}^{\infty} \sum_{m=0}^l \tilde{P}_{lm}(\cos \theta) [\Delta C_{lm} \cos(m\lambda) + \Delta S_{lm} \sin(m\lambda)] \quad (2.2)$$

We define $\Delta \sigma$ as the variation of mass density in a thin layer of the Earth's surface:

$$\Delta \sigma(\theta, \lambda) = \int_{\text{thin layer}} \Delta \rho(r, \theta, \lambda) dr \quad (2.3)$$

which is the radial integral of density redistribution $\Delta\rho$.

We expand $\Delta\sigma$ as a sum of SH coefficients:

$$\Delta\sigma(\theta, \lambda) = a\rho_w \sum_{l=0}^{\infty} \sum_{m=0}^l \tilde{P}_{lm}(\cos\theta) [\Delta\hat{C}_{lm} \cos(m\lambda) + \Delta\hat{S}_{lm} \sin(m\lambda)] \quad (2.4)$$

where ρ_w is the density of water (1000 kg m^{-3}). The ratio $\Delta\sigma/\rho_w$ is defined as the equivalent water thickness (EWT), which is often used for GRACE applications.

Suppose the observable mass redistribution of the Earth occurs within the thin surface layer, the SH coefficients of geoid change is a combination of direct gravitational attraction of surface mass change and an additional contribution caused by the solid Earth's loading effect [Chao, 1994; Farrell, 1972; Wahr et al., 1998]:

$$\begin{Bmatrix} \Delta C_{lm} \\ \Delta S_{lm} \end{Bmatrix} = \frac{3(1+k_l)}{4\pi a\rho_E(2l+1)} \int \Delta\sigma(\theta, \lambda) \tilde{P}_{lm}(\cos\theta) \begin{Bmatrix} \cos(m\lambda) \\ \sin(m\lambda) \end{Bmatrix} \sin\theta d\theta d\lambda \quad (2.5)$$

where k_l is the load Love number of degree l , ρ_E is the average density of the Earth (5517 kg m^{-3}).

By comparing equation 2.4 and 2.5, it is easy to find the relation between $(\Delta C_{lm}, \Delta S_{lm})$ and $(\Delta\hat{C}_{lm}, \Delta\hat{S}_{lm})$:

$$\begin{Bmatrix} \Delta C_{lm} \\ \Delta S_{lm} \end{Bmatrix} = \frac{3\rho_w}{\rho_E} \frac{1+k_l}{2l+1} \begin{Bmatrix} \Delta\hat{C}_{lm} \\ \Delta\hat{S}_{lm} \end{Bmatrix} \quad (2.6)$$

Or, conversely,

$$\begin{Bmatrix} \Delta\hat{C}_{lm} \\ \Delta\hat{S}_{lm} \end{Bmatrix} = \frac{\rho_E}{3\rho_w} \frac{2l+1}{1+k_l} \begin{Bmatrix} \Delta C_{lm} \\ \Delta S_{lm} \end{Bmatrix} \quad (2.7)$$

Finally, we can find the change of surface mass density from changes of geoid SH coefficients $(\Delta C_{lm}, \Delta S_{lm})$:

$$\Delta\sigma(\theta, \lambda) = \frac{a\rho_E}{3} \sum_{l=0}^{\infty} \sum_{m=0}^l \tilde{P}_{lm}(\cos\theta) \frac{2l+1}{1+k_l} [\Delta C_{lm} \cos(m\lambda) + \Delta S_{lm} \sin(m\lambda)] \quad (2.8)$$

Equation 2.8 is widely used to estimate the change of surface mass density (or in EWT) from geoid SH coefficients provided by GRACE gravity field solutions. Keep in mind we

assume that all temporal gravity signals originates from the Earth's surface. Since most mass fluctuations of the Earth occurs in atmosphere, cryosphere, ocean and upper crust within a 10-15 km layer, thin layer assumption is reasonable. Additionally, it is worthwhile to note that, considering the term $2l + 1$ in equation 2.8, the errors in high degree terms of geoid Stokes coefficients will be amplified significantly in estimation of change of surface mass density. In other words, although high degree SH coefficients can give more details of gravity field, the corresponding signals may be significantly suppressed by the potential errors in high degree SH coefficients. The methods to reduce errors in high degree SH coefficients will be discussed in the next section.

2.2 Post-processing Methods

2.2.1 Gaussian Smoothing

Gaussian filter on the sphere was firstly developed by Jekeli [1981] to smooth the Earth's gravity field. Then, Wahr et al. [1998] adopted Jekeli's Gaussian smoothing method to process Stokes coefficients of GRACE temporal gravity fields. In this method, the spatial averages of the surface mass density is expressed as:

$$\overline{\Delta\sigma}(\theta, \lambda) = \int \sin \theta' d\theta' d\lambda' \Delta\sigma(\theta', \lambda') W(\theta, \lambda, \theta', \lambda') \quad (2.9)$$

where $W(\theta, \lambda, \theta', \lambda')$ is an averaging function. Using equation 2.8 in the above equation gives

$$\begin{aligned} \overline{\Delta\sigma}(\theta, \lambda) = & \frac{a\rho_E}{12\pi} \sum_{l,m} \tilde{P}_{lm}(\cos \theta) \sum_{l',m'} \frac{2l'+1}{1+k_{l'}} [(\Delta C_{l'm'} W_{lmc}^{l'm'c} + \Delta S_{l'm'} W_{lmc}^{l'm's}) \cos(m\lambda) \\ & + (\Delta C_{l'm'} W_{lms}^{l'm'c} + \Delta S_{l'm'} W_{lms}^{l'm's}) \sin(m\lambda)] \end{aligned} \quad (2.10)$$

where

$$\begin{pmatrix} W_{lmc}^{l'm'c} \\ W_{lms}^{l'm'c} \\ W_{lmc}^{l'm's} \\ W_{lms}^{l'm's} \end{pmatrix} = \int \sin \theta d\theta d\lambda \int \sin \theta' d\theta' d\lambda' \begin{pmatrix} \cos(m'\lambda') \cos(m\lambda) \\ \cos(m'\lambda') \sin(m\lambda) \\ \sin(m'\lambda') \cos(m\lambda) \\ \sin(m'\lambda') \sin(m\lambda) \end{pmatrix} \times W(\theta, \lambda, \theta', \lambda') \tilde{P}_{lm}(\cos \theta) \tilde{P}_{l'm'}(\cos \theta') \quad (2.11)$$

If W is defined as a function of angle α between points (θ, λ) and (θ', λ') , equation 2.10 can be simplified to

$$\overline{\Delta\sigma}(\theta, \lambda) = \frac{2a\rho_E\pi}{3} \sum_{l=0}^{\infty} \sum_{m=0}^l \frac{2l+1}{1+k_l} W_l \tilde{P}_{lm}(\cos \theta) [\Delta C_{lm} \cos(m\lambda) + \Delta S_{lm} \sin(m\lambda)] \quad (2.12)$$

where

$$W_l = \int_0^\pi W(\alpha) P_l(\cos \alpha) \sin \alpha d\alpha \quad (2.13)$$

where $P_l = \tilde{P}_{lm=0}/\sqrt{2l+1}$ are the Legendre polynomials.

We adopt Jekeli's Gaussian averaging function [Jekeli, 1981] but normalize it so that global integral of W is 1:

$$W(\alpha) = \frac{b}{2\pi} \frac{\exp[-b(1 - \cos \alpha)]}{1 - e^{-2b}} \quad (2.14)$$

$$b = \frac{\ln(2)}{1 - \cos(r/a)} \quad (2.15)$$

where a is the Earth's radius, r is the Gaussian averaging radius which is the distance on the Earth's surface at which W drops to half of its value at $\alpha = 0$. The recursion relations

among W_l are:

$$\begin{aligned}
 W_0 &= \frac{1}{2\pi} \\
 W_1 &= \frac{1}{2\pi} \left[\frac{1+e^{-2b}}{1-e^{-2b}} - \frac{1}{b} \right] \\
 W_{l+1} &= -\frac{2l+1}{b} W_l + W_{l-1}
 \end{aligned} \tag{2.16}$$

In Figure 2.1, we summarize the relations among filtered/unfiltered changes of surface mass density in terms of EWH ($\overline{\Delta\sigma}$, $\Delta\sigma$), filtered/unfiltered geoid ($\overline{\Delta N}$, ΔN), and their SH coefficients ($[\overline{\Delta\hat{C}_{lm}}, \overline{\Delta\hat{S}_{lm}}]$, $[\Delta\hat{C}_{lm}, \Delta\hat{S}_{lm}]$, $[\overline{\Delta C_{lm}}, \overline{\Delta S_{lm}}]$ and $[\Delta C_{lm}, \Delta S_{lm}]$).

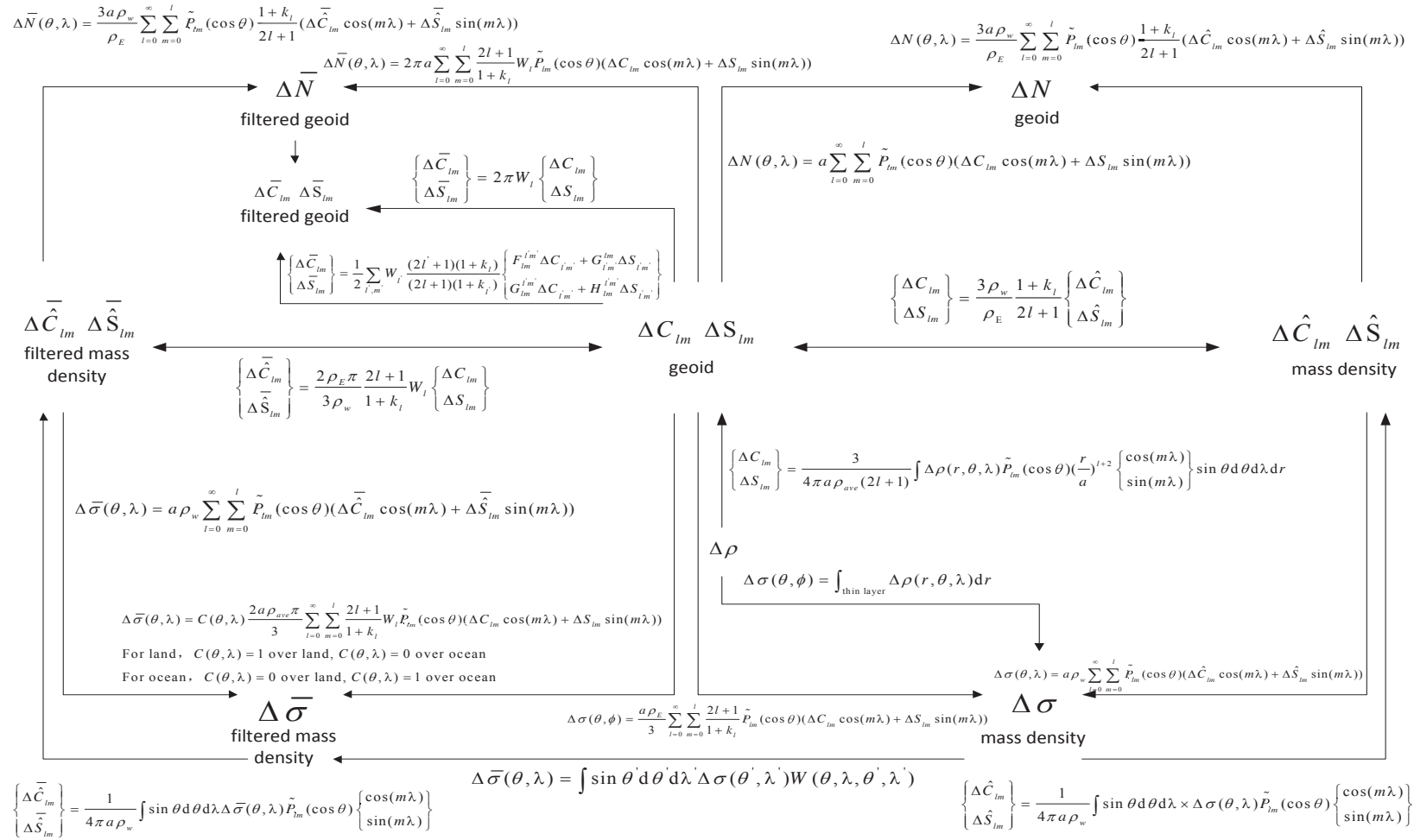


Figure 2.1: Relations among filtered/unfiltered changes of surface mass density in terms of EWH, filtered/unfiltered geoid, and their SH coefficients.

2.2.2 Destriping Methods

In spatial domain, original unconstrained monthly gravity field observed by GRACE shows north-south stripes, which represent the correlated errors in the gravity coefficients. As an example, spatial pattern of mass variations in October 2013 from original GRACE Stokes coefficients is shown in Figure 2.2. Swenson and Wahr [2006] found that, for a given order m , Stokes coefficients of the same parity are correlated with each other. They proposed a method to reduce this correlation by using quadratic polynomial in a moving window of width w centered at degree l . For example, for $C_{l,m}$, they used the Stokes coefficients $C_{l-2\alpha,m}, \dots, C_{l-2,m}, C_{l,m}, C_{l+2,m}, \dots, C_{l+2\alpha,m}$ to fit a quadratic polynomial, and removed the fitted value from original $C_{l,m}$ to derive the de-correlated $C_{l,m}$. The relation between the width of moving window w (i.e., the number of coefficients used for quadratic polynomial fitting) and α is $w = 2\alpha + 1$. In Swenson and Wahr [2006]’s paper, the detailed algorithm to determine the width of moving window was not provided. Referring to Swenson and Wahr’s unpublished results, Duan et al. [2009] provided the window width in the form of

$$w = \max(Ae^{-\frac{m}{K}} + 1, 5) \quad (2.17)$$

where m is order (≥ 5), $\max()$ takes the larger one of the two arguments. Swenson and Wahr [2006] have empirically chose $A = 30$ and $K = 10$ based on a trial-and-error procedure.

To estimate ocean mass change using GRACE, Chambers [2006] modified the algorithm described above. For RL02 GRACE solutions, they keep 7×7 portion of the coefficients unchanged, and fit a 7th order polynomial to the remaining coefficients to degrees with the same parity for each order up to 50. In their method, only one polynomial is used for each odd or even set for a given order, unlike the method from Swenson and Wahr [2006]. For RL04 GRACE solutions, they keep 11×11 portion of the coefficients unchanged, and a 5th order polynomial is applied. For latest RL05 GRACE solutions, the optimal parameterization based on the model test is to start filtering at degree 15, and adopt a 4th polynomial [Chambers and Bonin, 2012]. This processing method is denoted as P4M15.

Chen et al. [2007a] used the P3M6 method to process GRACE data and estimated co-

seismic and post-seismic deformation from the Sumatra-Andaman earthquake using GRACE. Later, they adopted the P4M6 method to estimate mass balance in ice caps, mountain glaciers, and terrestrial water storage change [Chen et al., 2009a, 2010a, 2007b, 2008, 2009b, 2010b].

Different from the above methods, Duan et al. [2009] determined the unchanged portion of coefficients based on the error pattern of the coefficients. Their unchanged portion of coefficients and the width of moving window depend on both degree and order in a more complex way. As an example, Figure 2.2 shows the global mass variations in October 2013 from GRACE Stokes coefficients based on different destriping methods. As shown in Figure 2.2(c-f), there is a general agreement among results from different destriping methods. In addition, destriping process suppresses the north-south stripes more efficiently, comparing the results with only the Gaussian smoothing applied.

In summary, the parameterization of destriping (or decorrelation) method for GRACE is dependent on the following criterion: (i) Determination of unchanged portion of coefficients: Swenson and Wahr [2006], Chambers and Bonin [2012] and Chen et al. [2007a] keep the first 4, 14 and 5 degree and order unchanged respectively; while Duan et al. [2009] determined the unchanged portion of coefficients based on their error pattern, which depends on both degree and order. (ii) Choice of the degree of polynomial fitting; (iii) How to apply the polynomial fitting to coefficients (moving window vs. fixed window): Swenson and Wahr [2006] adopted a moving window with the width, which depends on the degree; while Duan et al. [2009] determined the width of moving window as a function of both degree and order. In addition, Chambers [2006] and Chen et al. [2007a] do not move the window, but use a fixed window to fit the polynomial.

In addition, many filters are devised to reduce the noise of GRACE solutions, e.g., classic Gaussian filter [Jekeli, 1981; Wahr et al., 1998], non-isotropic filter [Han et al., 2005], statistical filter [Davis et al., 2008], DDK filter [Kusche, 2007], wavelet filter [Schmidt et al., 2006], wiener filter [Sasgen et al., 2007], fan filter [Zhang et al., 2009], and so on. In this thesis, we mainly adopt Swenson and Wahr [2006]'s destriping method to estimate regional terrestrial water storage variations and Chambers and Bonin [2012]'s destriping method to estimate regional ocean mass change inferred from GRACE.

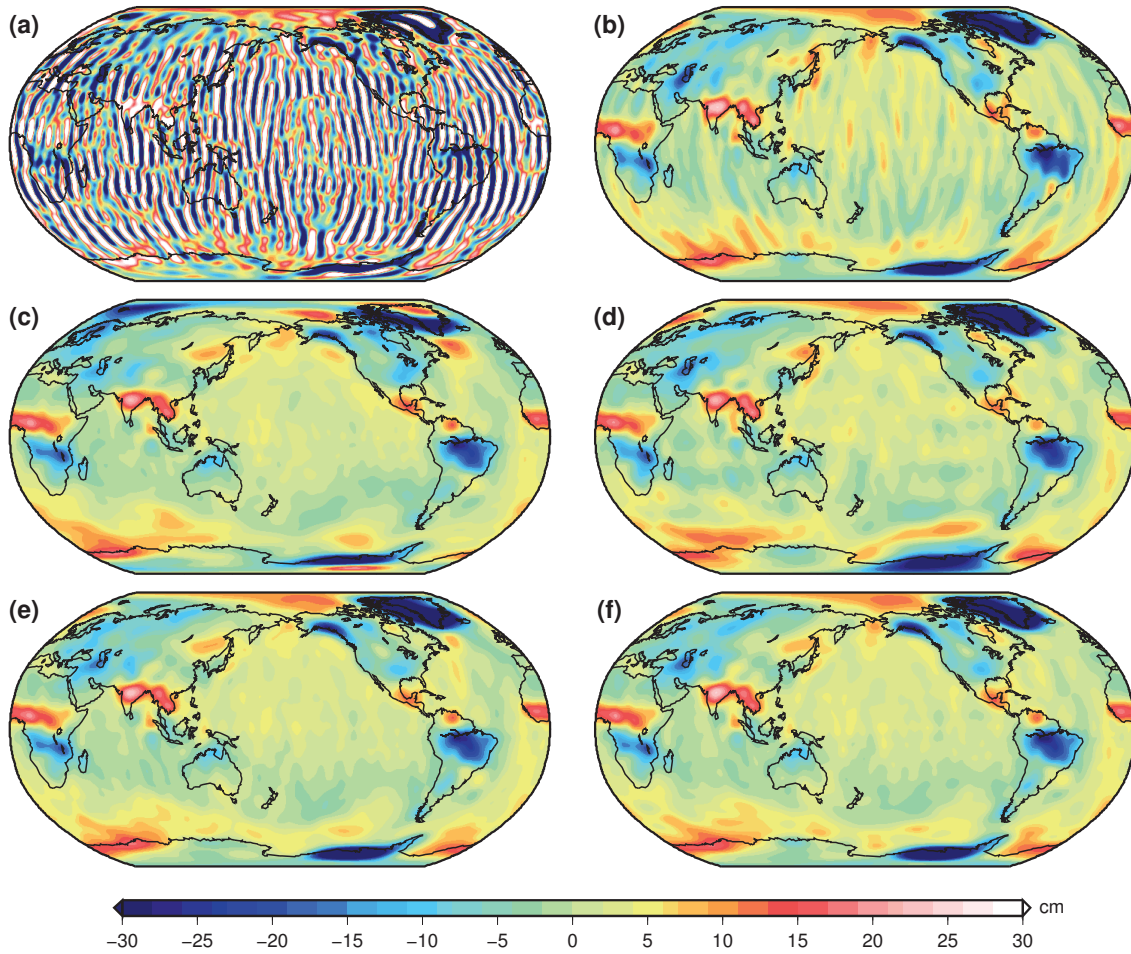


Figure 2.2: (a) Spatial pattern of mass variations in October 2013 from GRACE Stokes coefficients, no destriping and Gaussian smoothing applied. (b) Same as (a), but a 400 km Gaussian smoothing applied. (c-f) Same as (b), but destriping methods from Swenson and Wahr [2006], Chambers and Bonin [2012], Chen et al. [2007b], and Duan et al. [2009] applied.

2.2.3 GRACE Measurement Error

Wahr et al. [2006] determined the uncertainties in the GRACE Stokes coefficients as the standard deviation of the residuals of coefficients when seasonal cycles are removed. This method may overestimate the GRACE measurement error, since we assume that all non-seasonal variability of Stokes coefficients results from the measurement error. We randomly take the CSR RL05 GRACE solution in November 2011 for example. Figure 2.3 shows the spatial patterns of GRACE measurement error from original Stokes coefficients and from filtered Stokes coefficients with 300 km Gaussian smoothing. As shown in the figure, the GRACE measurement

errors depend on latitude and show high uncertainties in tropics and low uncertainties in polar regions. It is fairly reasonable since there are more GRACE observations in polar regions due to its near-polar orbit. In Figure 2.3b, when a 300 km Gaussian smoothing is applied, the magnitude of GRACE measurement error decreases significantly.

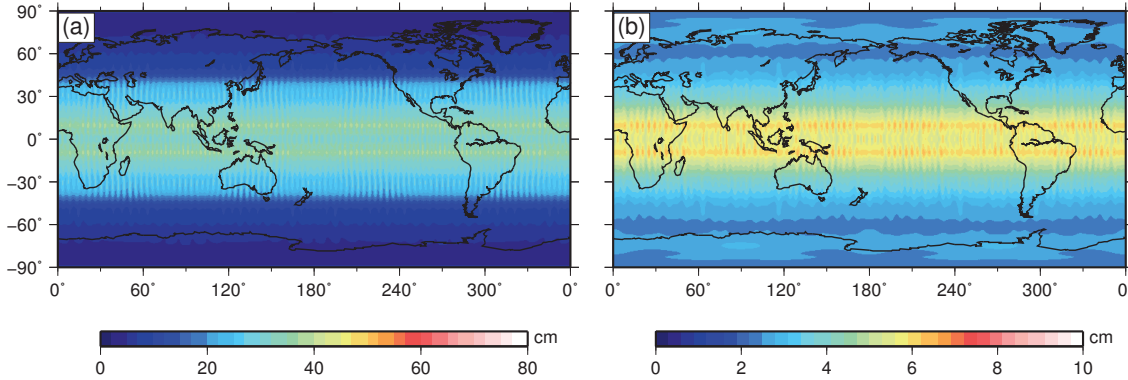


Figure 2.3: Spatial patterns of GRACE measurement error in November 2011 (a) without Gaussian smoothing and (b) with a 300 km Gaussian smoothing.

In addition, Chen et al. [2009b] proposed a simple approach to estimate the GRACE measurement error when they analyzed the terrestrial water storage variations in the Amazon River basin. Chen et al. [2009b] estimated the measurement error as root-mean-square variability over the oceans at the same latitude as the study region on land. If the ocean and atmosphere models perfectly simulate the mass change over the oceans, after the de-aliasing processing, there will be no mass change detected by GRACE. Therefore the residuals over the ocean can approximately represent the GRACE measurement error. Keep in mind that ocean variability and the deficiencies in de-aliasing products might be included in estimates of GRACE error. So this approach might overestimate the GRACE error too.

2.2.4 Basin-scale Mass Variations from Temporal Gravity Field

For a given region, we define the following basin kernel function:

$$\vartheta(\theta, \lambda) = \begin{cases} 1, & \text{inside the basin} \\ 0, & \text{outside the basin} \end{cases} \quad (2.18)$$

The spherical harmonics of the above kernel function can be expressed as:

$$\vartheta(\theta, \lambda) = \frac{1}{4\pi} \sum_{l'=0}^{\infty} \sum_{m'=0}^{l'} \tilde{P}_{l'm'}(\cos \theta) [\vartheta_{l'm'}^c \cos(m\lambda) + \vartheta_{l'm'}^s \sin(m\lambda)] \quad (2.19)$$

$$\begin{Bmatrix} \vartheta_{l'm'}^c \\ \vartheta_{l'm'}^s \end{Bmatrix} = \int \vartheta(\theta, \lambda) \tilde{P}_{l'm'}(\cos \theta) \begin{Bmatrix} \cos(m\lambda) \\ \sin(m\lambda) \end{Bmatrix} d\Omega \quad (2.20)$$

By using equation 2.4 in the above two equations, we find

$$\begin{aligned} \overline{\Delta\sigma}_{region} &= \frac{1}{\Omega_{region}} \int \Delta\sigma \vartheta d\Omega \\ &= \frac{a\rho_w}{\Omega_{region}} \frac{1}{4\pi} \sum_{l=0}^{\infty} \sum_{m=0}^l \tilde{P}_{l,m}^2(\cos \theta) (\Delta\hat{C}_{lm} \vartheta_{lm}^c + \Delta\hat{S}_{lm} \vartheta_{lm}^s) \\ &= \frac{a\rho_w}{\Omega_{region}} \sum_{l=0}^{\infty} \sum_{m=0}^l (\Delta\hat{C}_{lm} \vartheta_{lm}^c + \Delta\hat{S}_{lm} \vartheta_{lm}^s) \end{aligned} \quad (2.21)$$

where Ω_{region} is angular area of the given region (ratio of area of the given region to the Earth's radius squared).

With equation 2.6, equation 2.21 becomes

$$\overline{\Delta\sigma}_{region} = \frac{a\rho_E}{3\Omega_{region}} \sum_{l=0}^{\infty} \sum_{m=0}^l \frac{2l+1}{1+k_l} (\vartheta_{lm}^c \Delta C_{lm} + \vartheta_{lm}^s \Delta S_{lm}) \quad (2.22)$$

Mass change in terms of EWT in a given region can be expressed as:

$$\overline{\Delta h}_{region} = \frac{a\rho_E}{3\Omega_{region}\rho_w} \sum_{l=0}^{\infty} \sum_{m=0}^l \frac{2l+1}{1+k_l} (\vartheta_{lm}^c \Delta C_{lm} + \vartheta_{lm}^s \Delta S_{lm}) \quad (2.23)$$

Mass change in volume in a given region can be expressed as:

$$\overline{\Delta V}_{region} = \frac{a^3\rho_E}{3\rho_w} \sum_{l=0}^{\infty} \sum_{m=0}^l \frac{2l+1}{1+k_l} (\vartheta_{lm}^c \Delta C_{lm} + \vartheta_{lm}^s \Delta S_{lm}) \quad (2.24)$$

To reduce the GRACE measurement error, Gaussian smoothing kernel is often applied to

equation 2.23 and 2.24.

Leakage and Bias

Considering the limitation of GRACE observation accuracy, the Stokes coefficients of GRACE solutions are truncated to a limited degree l_{max} . So, the spatial resolution of GRACE products is limited to $20000/l_{max}$ km. Truncation of spherical harmonic coefficients in spectral domain is a low-pass filter in spatial domain. The real mass variation signal in a given region might be dampened due to the truncation of SH coefficients. In addition, the destriping, Gaussian smoothing, and regional averaging might make the estimate biased in a given region. The signal in the target region might leak out to the surrounding areas, which would cause an amplitude damping in the region (leakage out). Meanwhile, the signal from the surrounding areas might leak into the target region too (leakage in). Wahr et al. [1998] and Swenson and Wahr [2002] considered “leakage” to include both the signal leaking out of the target region and the signal leaking into the target region from the surrounding areas. However, Klees et al. [2007] and Longuevergne et al. [2010] considered the leakage out effect as “bias”, and the leakage in effect as “leakage”. In their naming convention, “leakage” only represents the contamination from the outside of the target region in a narrow sense. In this study, if not mentioned specifically, we refer to the latter name convention.

Suppose the function S describes the real mass variations on the Earth’s surface, then the mean value of mass variations over the region of interest R is

$$\bar{S}_0 = \frac{1}{R_0} \int_{\Omega} S h d\Omega \quad (2.25)$$

where R_0 is the area of the region, h is the ideal basin kernel function (1 inside the basin, 0 outside), Ω represents the entire Earth surface.

The GRACE estimate of mean value over the region of interest R is

$$\hat{\bar{S}}_0 = \frac{1}{R_0} \int_{\Omega} \hat{S} h d\Omega \quad (2.26)$$

where \hat{S} represents the filtered GRACE estimate of mass variation.

To recover the real average mass variation signal \bar{S}_0 in a given region from the GRACE estimate \hat{S}_0 , there are two following methods. In the first method, real average mass variation signal \bar{S}_0 in a given region is re-written as [Klees et al., 2007]

$$\bar{S}_0 = \hat{S}_0 - S_{leakage} + S_{bias} \quad (2.27)$$

with

$$S_{leakage} = \frac{1}{R_0} \int_{\Omega-R} S_{out} \hat{h} d\Omega \quad (2.28)$$

$$S_{bias} = \frac{1}{R_0} \int_R S_{in} (h - \hat{h}) d\Omega \quad (2.29)$$

where S_{in} and S_{out} represent the real mass variations in the region of interest and outside, \hat{h} represents the averaging kernel function applied to GRACE data.

In this method, we need to remove the leakage $S_{leakage}$ from the GRACE estimate \hat{S}_0 first, then add the bias S_{bias} back. To calculate the leakage and bias for a given region, a priori information about mass variations both in the region of interest and outside should be available, which usually comes from hydrological models and ocean models. Based on a calibrated regional hydrological model for Southern Africa, Klees et al. [2007] estimated the leakage and bias effect to GRACE-based terrestrial water storage variations in the Zambezi river basin. They found that, after applying leakage and bias corrections from a priori hydrological model, the fit between GRACE and the hydrological model is improved significantly. Even if another independent hydrological model is used to estimate leakage and bias corrections, the agreement between GRACE and the original hydrological model is still significant. Therefore, it is necessary to apply leakage and bias corrections to the GRACE estimate, if a priori information about mass variations is available. Keep in mind that the uncertainty of the priori information would cause the overestimation or underestimation of the leakage and bias.

In the other method, we give the following equation:

$$\bar{S}_0 = k(\hat{S}_0 - S_{leakage}) \quad (2.30)$$

where k is the scaling factor (or multiplicative factor), which is expressed as

$$k = \frac{\int_R S_{in} h d\Omega}{\int_R S_{in} \hat{h} d\Omega} \quad (2.31)$$

If the reliable mass variations over the study region are available, we can use the above equation to estimate the scaling factor. However, it is not always the case. Assuming that a uniform distribution of mass within the region of interest, k can be simplified to

$$k = \frac{1}{\int_R \hat{h} d\Omega} \quad (2.32)$$

Based on equation 2.32, to estimate the scaling factor, we need to construct a ideal kernel function for the region of interest (1 inside and 0 outside), decompose it into truncated spherical harmonics, then apply the destriping and smoothing to these spherical harmonics. After that, the reciprocal of the signal left within the region is considered as the scaling factor. To calibrate GRACE estimate in the study of mass balance in Antarctica, Velicogna and Wahr [2006b] applied the averaging function to a uniform mass variation over the ice sheet, and the left signal inside the region was 0.62. Thus, they applied the GRACE estimate with a scaling factor 1/0.62 to recover the real mass variation signal over the whole ice sheet. In addition, a scaling factor of 1.95 is obtained when they studied the ice mass loss in Greenland [Velicogna and Wahr, 2006a]. To obtain the mass variations in the Mediterranean Sea using GRACE, Fenoglio-Marc et al. [2006] estimated a scaling factor of 1/0.56 based on original and filtered mass variations from steric-corrected altimetry. In the Caspian Sea, a scaling factor of 1/0.37 is multiplied with GRACE original estimate to analyze the water storage variations [Swenson and Wahr, 2007]. A scaling factor of 1.95 is determined to recover the magnitude damping of GRACE-based groundwater storage variations in northern India [Rodell et al., 2009].

The above two methods are widely used to estimate time series of regional mass variations from GRACE. In addition, the leakage effect can be estimated and removed in spatial domain. We proposed a modification of Wahr et al. [1998]'s method to reduce the leakage using GRACE observations as follows: (i) Convert the original GRACE SH coefficients into grids; (ii) Keep the values over land unchanged, and set the values over ocean to zeros; (iii) Then,

convert the grids to SH coefficients and do the specified destriping and Gaussian smoothing; (iv) After that, convert the filtered coefficients to grids again. The values over ocean in these grids, to first order, represent the leakage effect from the continent, which should be removed from GRACE results. This method is carried out in spatial domain, but is equivalent to Wahr et al. [1998]’s method which is employed in spectral domain. As shown in Figure 2.4, the standard deviation of ocean mass changes from GRACE is significantly reduced near the coast of large river basins (e.g., the Amazon basin), when leakage corrections are applied.

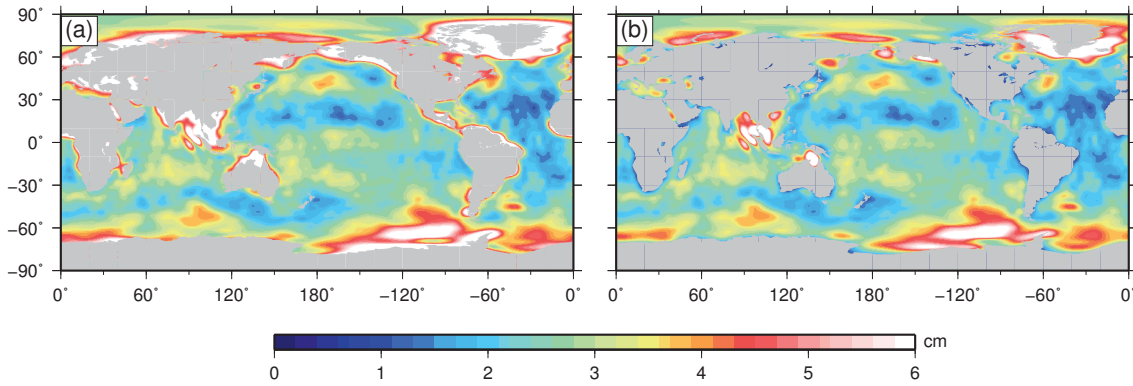


Figure 2.4: Standard deviation of ocean mass changes from GRACE (CSR RL05) during 2003-2011 (a) without leakage correction and (b) with leakage correction.

Error Estimation for Basin-scale Mass Variations

As summarized by Longuevergne et al. [2010], when we estimate basin-scale mass variations using the scaling factor method, the total error induced by the GRACE data processing ΔS_{total} can be written as

$$\Delta S_{total} = k\Delta\hat{S}_0 + \Delta k(\hat{S}_0 + S_{leakage}) + k\Delta S_{leakage} \quad (2.33)$$

where $k\Delta\hat{S}_0$ is the scaled GRACE measurement error, $\Delta k(\hat{S}_0 + S_{leakage})$ represent the errors caused by the uncertainty of the scaling factor estimation, and $k\Delta S_{leakage}$ is the error due to the uncertainty of the leakage correction.

As a summary, Figure 2.5 shows the processing flow of the basin-scale mass variation estimation and error estimation from GRACE.

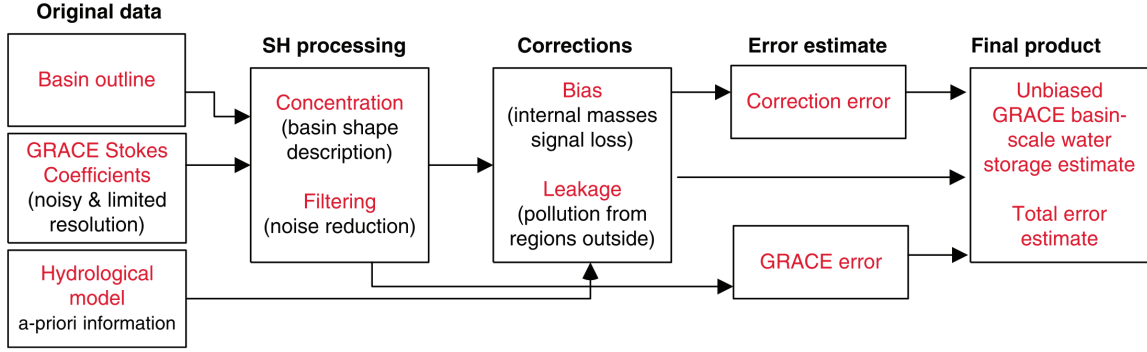


Figure 2.5: Synthesis of basin-scale mass variation estimation and error estimation from Stokes coefficients of GRACE temporal gravity fields. (From Longuevergne et al. [2010])

2.3 Combination of Altimetry, GRACE and Oceanographic Data

Satellite altimetry can observe the total SLV over the global ocean, while GRACE and oceanographic data can be used to estimate mass-induced SLV and steric SLV respectively. Nevertheless, to study the global sea level budget using these three independent observations, some attention should be paid to make these observations in a self-consistent way.

2.3.1 Steric Sea Level Variations

Steric sea level variations (SLV) is produced by the expansion and contraction of the water column due to seawater density change, which can be expressed as [Gill and Niiler, 1973; Pattullo et al., 1955; Tomczak and Godfrey, 1994]

$$\eta'_{st}(\theta, \lambda, t) = -\frac{1}{\rho_0} \left[\int_{-h}^{\eta} \frac{\partial \rho}{\partial T} T'(\theta, \lambda, z, t) dz + \int_{-h}^{\eta} \frac{\partial \rho}{\partial S} S'(\theta, \lambda, z, t) dz \right] \quad (2.34)$$

where ρ_0 is the reference seawater density, θ , λ and z are the latitude, longitude and depth of a given point respectively, t is time, $\partial \rho / \partial T$ and $\partial \rho / \partial S$ is the partial derivatives of density to temperature and salinity at a given point, T' and S' are changes of temperature and salinity at the point, η represents the sea surface height (SSH) relative to the reference bottom of the

upper layer in a two layer fluid, $-h$ represents the depth of the lower layer.

The equation 2.34 can be simplified to

$$\eta'_{st}(\theta, \lambda, t) = \int_{-h}^{\eta} \alpha(\theta, \lambda, z, t) T'(\theta, \lambda, z, t) dz + \int_{-h}^{\eta} \beta(\theta, \lambda, z, t) S'(\theta, \lambda, z, t) dz \quad (2.35)$$

where $\alpha = -\frac{1}{\rho_0} \frac{\partial \rho}{\partial T}$ is the thermal expansion coefficient of seawater, $\beta = -\frac{1}{\rho_0} \frac{\partial \rho}{\partial S}$ is the salinity expansion coefficient of seawater. The first term on the right-hand side of equation is thermosteric SLV, while the second term represents the halosteric SLV.

In general, the haline contribution to global steric sea level variation is negligible, although it might be significant in some regional ocean, such as the subpolar Atlantic Ocean [Antonov et al., 2002]. Neglecting the halosteric SLV leaves,

$$\eta'_{st}(\theta, \lambda, t) = \int_{-h}^{\eta} \alpha(\theta, \lambda, z, t) T'(\theta, \lambda, z, t) dz \quad (2.36)$$

Furthermore, assuming that the thermal expansion coefficient α is constant over the depth, we obtain the relation between the steric SLV and seawater temperature anomalies:

$$\eta'_{st}(\theta, \lambda, t) = \alpha_0(\theta, \lambda, t) \int_{-h}^{\eta} T'(\theta, \lambda, z, t) dz \quad (2.37)$$

2.3.2 Glacial Isostatic Adjustment

Glacial Isostatic Adjustment is the Earth's viscoelastic response to the last deglaciation following the last glacial maximum (LGM) [Lambeck and Nakiboglu, 1984; Peltier, 1986]. To estimate ocean mass trends from GRACE observations, the long-term gravitational signal caused by GIA should be removed. In addition, the long-term sea bottom deformation caused by GIA should be removed from geocentric sea level variations observed by satellite altimetry. In this thesis, we adopt the GIA model from A et al. [2013], which is an update of the GIA model from Paulson et al. [2007] and uses the ICE-5G deglaciation history and the PREM-based Earth model [Dziewonski and Anderson, 1981; Peltier, 2004]. Figure 2.6 demonstrates the GIA mass rate and uplift rate with SH expansion up to degree 100.

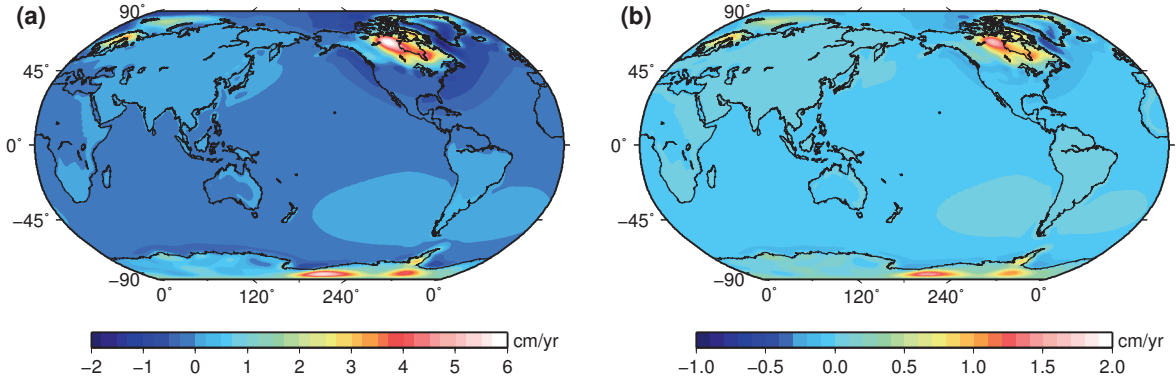


Figure 2.6: (a) GIA mass rate in terms of equivalent water thickness and (b) GIA uplift rate with SH expansion up to degree 100. (Adapted from A et al. [2013])

2.3.3 Elastic Loading Deformation

Owing to the elastic loading effect, mass change in the water column produces a vertical displacement in the ocean bottom, which may not be negligible in some regional ocean [Kuo et al., 2008]. This elastic loading deformation should be removed from altimetry, when comparing with GRACE results. The following equation is used to calculate this loading deformation:

$$\Delta H(\theta, \lambda) = a \sum_{l=0}^{\infty} \sum_{m=0}^l \tilde{P}_{lm}(\cos \theta) \frac{h_l}{1+k_l} [\Delta C_{lm} \cos(m\lambda) + \Delta S_{lm} \sin(m\lambda)] \quad (2.38)$$

where a is the Earth's radius, θ , λ are co-latitude and longitude respectively, l is degree and m is order, $\tilde{P}_{lm}(\cos \theta)$ is the fully normalized associated Legendre function, ΔC_{lm} , ΔS_{lm} are geopotential spherical harmonics respectively, k_l is potential Love number, and h_l is vertical Love number.

Stokes coefficients from GRACE products are employed to compute the vertical loading deformation in the ocean bottom. Figure 2.7 shows the vertical loading deformation in the ocean bottom in January 2003 based on GRACE-observed ocean mass variations in the same month.

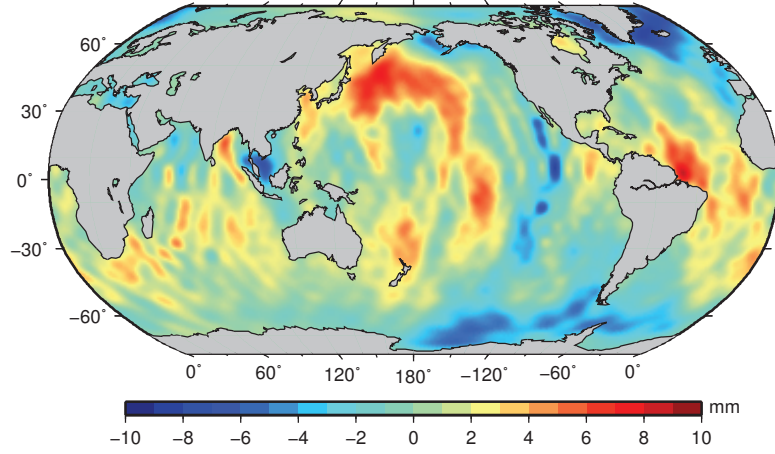


Figure 2.7: Vertical loading deformation in the sea bottom in January 2003 based on GRACE-observed ocean mass variations in the same month. A 300 km Gaussian smoothing is applied to GRACE data.

2.3.4 Inverted Barometer Corrections

In this study, inverse-barometer (IB) corrected gridded altimetry data from the Archiving, Validation and Interpretation of Satellite Oceanographic (AVISO) data are used. When comparing IB-corrected altimetry with GRACE, the time-varying mass of the atmosphere averaged over the ocean should be considered and removed from GRACE results. From integration of the hydrostatic equation over the whole water column, the ocean bottom pressure (OBP) P_{bot} is a sum of the atmosphere pressure and the pressure from the water column [Ponte, 1993]:

$$P_{bot} = P_{atm} + g \int_{-H}^{\eta} \rho dz \approx P_{atm} + g\rho_0\eta + g \int_{-H}^0 \rho dz \quad (2.39)$$

where P_{bot} is ocean bottom pressure, P_{atm} is surface atmospheric pressure, g is gravity constant, ρ is seawater density, ρ_0 is mean seawater density (1025 kg m^{-3}), and η is the sea surface height (SSH) with respect to the geoid. The OBP anomaly at a given point at time t_1 is

$$\Delta P_{bot,1} = \Delta P_{atm,1} + g\rho_0(\eta_1 - \bar{\eta}) + g \int_{-H}^0 (\rho_1 - \bar{\rho}) dz \quad (2.40)$$

where $\Delta P_{atm,1}$ is the surface atmospheric pressure anomaly at the given point, $\bar{\eta}$ is the mean SSH at the given point, $\bar{\rho}$ is the mean density at a given depth.

According to the definition of IB effect, IB-corrected SSH at this point at t_1 can be written as

$$\eta_{IB,1} = \eta_1 + \frac{P_{atm,1} - \bar{P}_{ocean,1}}{\rho_0 g} \quad (2.41)$$

where $P_{atm,1}$ is surface atmospheric pressure at the given point at t_1 and $\bar{P}_{ocean,1}$ is the average atmospheric pressure over the ocean at t_1 .

Considering the average of IB-corrected SSH at the given point for the period from t_1 to t_n , we have

$$\bar{\eta}_{IB} = \bar{\eta} + \frac{\bar{P}_{atm} - \bar{P}_{ocean}}{\rho_0 g} \quad (2.42)$$

where $\bar{P}_{atm} = \frac{\sum_i P_{atm,i}}{n}$ and $\bar{P}_{ocean} = \frac{\sum_i \bar{P}_{ocean,i}}{n}$.

From equation 2.41 and 2.42, we get

$$\frac{\Delta P_{atm,1} - \Delta \bar{P}_{ocean,1}}{g\rho} = (\eta_{IB,1} - \bar{\eta}_{IB}) - (\eta_1 - \bar{\eta}) \quad (2.43)$$

Introducing equation 2.43 into 2.40, we get

$$\frac{\Delta P_{bot,1}}{g\rho_0} = \frac{\Delta \bar{P}_{ocean,1}}{g\rho_0} - (\eta_{IB,1} - \bar{\eta}_{IB}) - \left[-\frac{1}{\rho_0} \int_{-H}^0 (\rho_1 - \bar{\rho}) dz \right] \quad (2.44)$$

Equation 2.44 reveals the relation between IB-corrected altimetry and GRACE. The left-hand side of equation 2.44 represents the OBP anomaly in terms of EWT observed by GRACE, when the the atmosphere/ocean de-aliasing model (GAD) is added back to GRACE Stokes coefficients. On the right-hand side of equation 2.44, the first term represents the anomaly of atmosphere pressure averaged over the ocean at time t_1 , the second term is the anomaly of IB-corrected SSH from altimetry, and the last one is the steric sea level variations. Thus, to be consistent with IB-corrected altimetry, the time-varying mass of the atmosphere averaged over the ocean should be removed from GRACE-observed OBP anomaly. This can be easily calculated from the atmosphere/ocean de-aliasing model provided by GRACE products. As shown in Figure 2.8, the annual amplitude of this correction is about 6 mm.

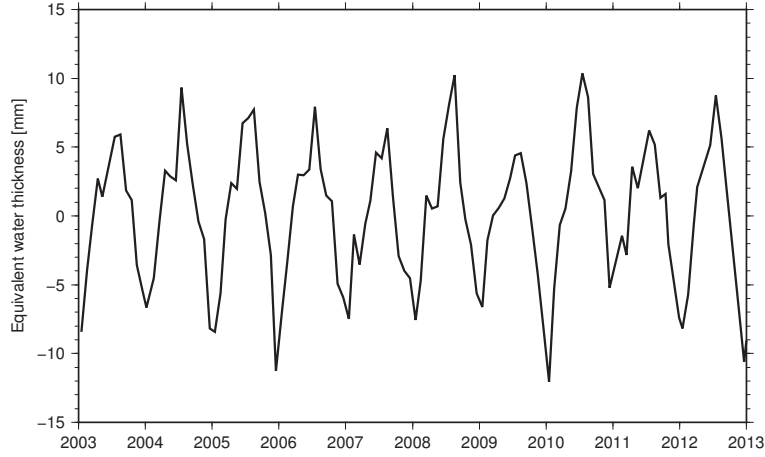


Figure 2.8: Time-varying mass of the atmosphere averaged over the ocean based on GRACE GAD data.

2.3.5 Boussinesq Approximation

In most ocean models (e.g., ECCO), Boussinesq approximation is widely used. With this approximation, most ocean models conserve the volume of the ocean unchanged. However, actually, ocean volume is not strictly conserved. For example, a global warming of the ocean will decrease the seawater density, and the volume of the ocean will increase, but no changes in mass involved. However, with the Boussinesq approximation, since the volume of the ocean keeps constant, the decrease of seawater density will cause a negative OBP anomaly, i.e., the loss of ocean mass, which is unreal. To correct for the missing physics, a spatially homogeneous sea level signal should be added to the steric SLV calculated from Boussinesq ocean models, as corrections for the unmodeled volume changes [Ponte, 1999]:

$$\delta\bar{\eta}_\rho = -\frac{1}{A} \int_V \frac{\delta\rho}{\rho_0} dV \quad (2.45)$$

where A and V are the surface area and volume of the ocean respectively, $\delta\rho$ is the seawater density anomaly relative to the reference density ρ_0 . Based on the temperature and salinity data from the ECCO ocean model, we calculated the time series of the Boussinesq correction (Figure 2.9).

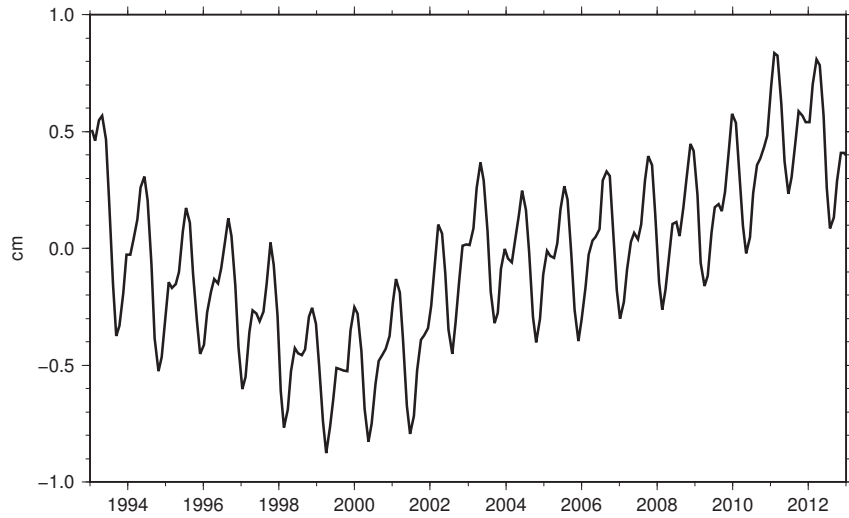


Figure 2.9: Boussinesq correction for the steric SLV based on the temperature and salinity data from the ECCO ocean model.

2.4 Summary

In this chapter, we introduced the basics of temporal gravity fields and described the post-processing methods for GRACE level-2 Stokes coefficients. Especially, the regional mass variation estimation from GRACE temporal gravity fields, related leakage and bias corrections, and error assessment are given in detail. The steric sea level variations calculation and relevant notice in combining altimetry, GRACE and oceanographic data are described.

GROUNDWATER STORAGE VARIATIONS IN NORTH CHINA FROM GRACE

3.1 Introduction

Groundwater in the North China Plain (NCP), the largest wheat/maize production zone in China, is of great importance for water resources management, agricultural development, and ecosystem health in the region. The NCP includes one shallow unconfined aquifer and three deep confined aquifers of different depths (40-60 m, 120-170 m, 250-350 m, and 400-600 m) [Sakura et al., 2003]. The aquifers consist of sand, gravel, clay, and silt. The region belongs to the littoral and semi-arid climatic zone with nearly 70% of the rainfall occurring from June to September and 10% from March to May. Annual rainfall in this area ranges from approximately 400-600 mm/yr, whereas the evaporation rate is approximately 1,000 mm/yr [Liu et al., 2002]. Since the 1970s, rapid agricultural and industrial development has resulted in great demand for water resources. Nearly all of the major rivers in North China, including the Hai River, are dammed for hydro-electric power generation and urban water use. The Yellow River flows through the western and southern parts of the study region. However, only a small percentage of surface water here is used for agricultural irrigation [Yang et al., 2010]. Instead groundwater is pumped for use in agricultural irrigation. In the NCP, more than 60% of fresh water comes from groundwater [Ministry of Water Resources of China (MWR), 2010], and agricultural irrigation in this area relies heavily on groundwater [Kendy et al., 2003; Yang

et al., 2010]. In the piedmont region of the Taihang Mountains where irrigation requirements are high, shallow groundwater level differences between 1958 and 1998 are as high as 50 m, whereas deep groundwater level differences over the same time period are as high as 90 m [World Bank, 2001]. By 2004, there were more than 7.6 million tube wells in North China, and 68% of irrigation here came from groundwater [Wang et al., 2007]. In 2009, groundwater accounted for 61% of the total water supply in Beijing, 26% in Tianjin, 80% in the Hebei province, and 58% in the Shanxi province [Ministry of Water Resources of China (MWR), 2010]. With continued groundwater consumption, large depression cones have formed in the NCP [Liu et al., 2001]. Based on the hydrogeological dataset for North China, Foster et al. [2004] concluded that the excessive abstraction of groundwater has led to severe groundwater depletion in the piedmont and flood plain regions of the NCP.

As mentioned in the Introduction chapter, the GRACE mission presents a new opportunity to monitor groundwater storage (GWS) variations. GRACE-observed terrestrial water storage (TWS) change is the vertically integrated measure of groundwater storage (GWS), soil moisture storage (SMS), snow water equivalent storage (SWES), and surface water reservoir storage (RESS). To isolate GWS from total TWS, other components must be estimated from land surface models (LSMs) or observations: $\Delta GWS = \Delta TWS - \Delta SWES - \Delta RESS - \Delta SMS$.

Recently, two studies have reported the water mass loss in the NCP from GRACE. Zhong et al. [2009] studied TWS trends in China using early GRACE data (level 2, Release 04) and found a TWS loss in Beijing, Hebei, and Tianjin at a rate of 2.4 cm/yr from 2003-2007. Su et al. [2011] also found a decline TWS rate of 1.1 cm/yr in North China. Moiwu et al. [2009] estimated TWS changes in the Hai River basin of North China based on gridded GRACE data (level 3, Release 04) collected over 4 years and compared the results with in situ hydrological measurements. They found a TWS loss in the range of 1.3-2.4 cm/yr for the period from 2003-2006. However, the regional TWS time series based on level 3 GRACE data are potentially contaminated by leakage and amplitude-damping effects in GRACE data processing. In this study, we use the latest level 2 GRACE products and consider the leakage and amplitude-damping effects to make the estimate more reliable. We explore the potential of GRACE to monitor groundwater storage variations in North China, and compare the GRACE

estimates with those from ground observations, groundwater modeling, and government reports. As shown in Figure 3.1, our study region includes Beijing, Tianjin, Hebei province, Shanxi province, and parts of Henan province and Shandong province. The boundaries of Hai River basin and North China Plain are also shown in Figure 3.1. Our study region includes the whole North China Plain and nearly the whole Hai River basin. The area of our study region is large enough ($\sim 434,000 \text{ km}^2$) to be observed by the GRACE satellites.

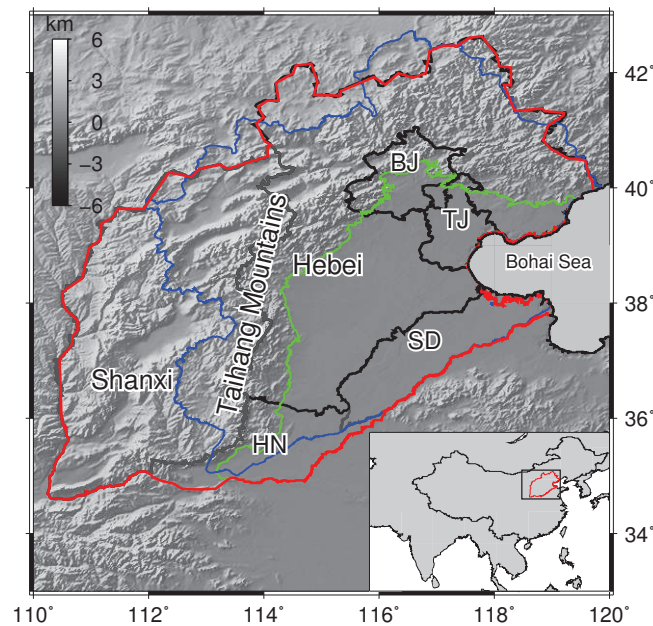


Figure 3.1: Location and shaded relief topography of North China. Boundaries of Beijing (BJ), Tianjin (TJ), Hebei province and Shanxi province are shown in black lines. Blue and green lines show the boundaries of Hai River basin and North China Plain respectively. Parts of Henan (HN) province and Shandong (SD) province are also included in our study region (red boundaries), since they belong to the NCP.

3.2 Data and Methods

3.2.1 GRACE Data and Processing

We used the monthly Release 05 GRACE solutions provided by the Center for Space Research (CSR) at the University of Texas at Austin. The solutions were expressed in the form of spherical harmonic (SH) coefficients truncated to degree and order (d/o) 60. The degree

2 order 0 (C_{20}) coefficients in the GRACE data were replaced by estimates obtained from satellite laser ranging [Cheng and Tapley, 2004]. Monthly geocenter estimates calculated by Swenson et al. [2008b] were used to account for the degree 1 coefficients of the gravity field, which GRACE does not observe. The GRACE data were corrected for glacial isostatic adjustment (GIA) based on the model of Paulson et al. [2007], which was updated by A et al. [2013]. The SH coefficients were filtered to remove north-south stripes [Swenson and Wahr, 2006] and to reduce high frequency noise (200 km Gaussian smoothing). Furthermore, we applied the following regional kernel function to these SH coefficients to obtain the TWS in the study area [Swenson and Wahr, 2002]:

$$\hat{S}_0 = \frac{4\pi a^3 \rho_E}{3R_0} \sum_{l=0}^{L_{max}} \sum_{m=0}^l \frac{2l+1}{1+k_l'} (\vartheta_{lm}^c \Delta C_{lm} + \vartheta_{lm}^s \Delta S_{lm}) \quad (3.1)$$

where R_0 is the area of the region, a and ρ_E are the mean radius and density of the Earth, k_l' is the l th load potential Love number, ΔC_{lm} and ΔS_{lm} are the SH coefficients anomalies with respect to the mean gravity field for the period ranging from 2003-2010, and ϑ_{lm}^c and ϑ_{lm}^s are the SH coefficients of the kernel function \hat{h} . We constructed the kernel function by decomposing the mask grid (1 at points inside the region and 0 at those outside) into SH coefficients, which were truncated to degree $L_{max}=60$.

All of the processes mentioned above (i.e., truncation of SH coefficients to d/o 60, de-striping, smoothing, and applying the kernel function) could make the TWS estimate biased within a given region. The signal in the target area might leak out to the surrounding areas, which would cause an amplitude damping in the area (bias). Meanwhile, the signal from the surrounding areas might leak into the target area (leakage). In theory, the regional water storage value \bar{S}_0 estimated by the above method can be presented in the following integral forms [Klees et al., 2007]:

$$\begin{aligned} \bar{S}_0 &= \frac{1}{R_0} \int_{\Omega} S_0 \hat{h} d\Omega \\ &= \frac{1}{R_0} \int_R S_{in} \hat{h} d\Omega + \frac{1}{R_0} \int_{\Omega-R} S_{out} \hat{h} d\Omega \end{aligned} \quad (3.2)$$

where S_0 is the true water storage variation field, S_{in} and S_{out} are the true variations inside and outside the basin, and \bar{S}_0 is the original regional estimate before bias and leakage corrections are applied. The first item on the right side of the equation is the biased estimate, and the second item is the leakage effect from outside of the basin. The true value in the basin is $\frac{1}{R_0} \int_R S_{in} h d\Omega$, where h is the exact kernel (1 inside the basin, 0 outside). To recover this true value in the basin, we removed the leakage effect from the original estimate and corrected the biased estimate.

The time series for leakage around the basin can only be estimated from mass change models, because there are no reliable observations of global large-scale mass variations except from GRACE. To estimate this “leakage in” signal, we constructed the synthetic global mass change from four hydrological models (see next section) and ocean bottom pressure data from a Jet Propulsion Laboratory (JPL) version of the Estimating Circulation and Climate of the Ocean general circulation model [Lee et al., 2002]. We added a uniform layer to the global ocean to conserve the total land and ocean mass at every time step [Velicogna and Wahr, 2006a,b]. The average values and standard deviations of the leakage time series from four models were calculated as our final leakage corrections and uncertainties.

Furthermore, we used the scaling factor method to restore the amplitude-damped TWS time series. Many researchers have applied this method to study ice sheet mass loss in Greenland and Antarctica [Velicogna and Wahr, 2006a,b], mass-induced sea level variations in the Mediterranean Sea and the Caspian Sea [Fenoglio-Marc et al., 2006; Swenson and Wahr, 2007], and seasonal water storage variations in major drainage basins of the world [Chen et al., 2007c]. We used a scaling factor of 2.51 (corresponding to 200 km Gaussian smoothing) to restore the TWS time series (more details, see Section 3.3.4).

In this study, we did not use the TWS and SMS time series to estimate GWS anomalies directly. Instead, we used a new method proposed by Scanlon et al. [2012], in which SMS data are filtered in the same way as GRACE data initially (i.e., projection of model grids to SH coefficients, truncation to d/o 60, application of a 200 km Gaussian smoothing). Next we removed this filtered SMS value from the GRACE-derived TWS value to obtain the filtered GWS value. Because we assumed that GWS changes are concentrated inside the area of

interest, restoring the filtered GWS only requires bias correction (i.e., applying scaling factor) and no leakage correction (no external groundwater masses leaking into the area of interest) is needed. Therefore, errors of leakage corrections outside the area should be minimized. The scaling factor could be estimated using information on the spatial distribution of GWS changes, which is generally estimated from groundwater models or groundwater observations. Note that because the scaling factor is a parameter describing the relative change, the possible underestimates from groundwater models or statistical data will not affect the scaling factor estimate. We applied the gridded groundwater observations released by the Ministry of Water Resources of China (MWR) to estimate the scaling factor for GWS changes (1.99, see Section 3.3.4).

3.2.2 Land Surface Models

We used seven land surface models (LSMs): four versions (NOAH, VIC, CLM and MOSAIC) of the GLDAS model from NASA [Dai and Zeng, 1997; Ek et al., 2003; Koster and Suarez, 1992; Liang et al., 1994; Rodell et al., 2004], the Climate Prediction Center (CPC) model from the National Oceanic and Atmospheric Administration (NOAA) [Fan and van den Dool, 2004], the WaterGAP Hydrology Model (WGHM) [Döll et al., 2003], and the version 4.5 of Community Land Model (CLM4.5) [Oleson et al., 2013]. Soil water outputs from seven LSMs and snow water equivalents from GLDAS models are averaged to get the best estimates of natural water change. The snow water component is typically small, and its contribution to the long-term TWS trend of North China is negligible ($<0.01 \text{ km}^3/\text{yr}$). WGHM and CLM2.5 models end in 2010. GLDAS and CPC models do not include the groundwater or surface water storage components. In WGHM, the effect of water use (e.g., irrigation) to soil water is taken into account. WGHM and CLM4.5 also model the groundwater storage variations. However, WGHM still fails to simulate GWS variations in North China [Döll et al., 2014]. The GWS change in North China derived from CLM4.5 is very small and not taken into account in our study, since we aim to isolate total GWS change from GRACE-derived TWS change. The average values and standard deviations of the different hydrological models were calculated as the best estimates and uncertainties of SMS. To isolate the GWS changes from the TWS

changes, we also need to remove the contribution from the surface water reservoir storage. Nearly all of the major rivers in North China are dammed for municipal and industrial use. Although surface water storage changes is unlikely to contribute significantly to long-term TWS changes in North China during the study time period, we still estimate it using data from Water Resources Bulletins of Hai River Basin (available at: <http://www.hwcc.gov.cn>).

3.2.3 Ground-based Measurements

Gridded groundwater table depth maps of shallow aquifers in North China Plain were obtained from contour maps released by Ministry of Water Resources of China (available at: <http://sqqx.hydroinfo.gov.cn/shuiziyuan/>). Released monthly contour map is the relative changes compared to the map in the same month of previous year. We digitized these maps into gridded ones with the resolution of $0.25^\circ \times 0.25^\circ$. These maps show the changes of groundwater table depth in the plains of Huang-Huai-Hai basin, which contains the North China Plain.

Time series of monthly groundwater table depth changes of 19 cities in our study region were also obtained from the website of MWR. We get the area-weighted mean groundwater level change series in the NCP from these time series.

To convert the gridded groundwater table depth change to the GWS change, the spatial pattern of specific yields has to be estimated. In the NCP, the specific yield of shallow aquifers increases westwards from <0.05 in the coastal plain around the margin of the Bohai Sea to >0.2 in the piedmont region of the Taihang Mountains. We digitized the contour map of specific yields in the NCP provided by Zhang and Fei [2009]. The mean value of specific yields in the NCP is 0.059, which we used to estimate mean GWS changes in the study region.

We also used the GWS statistics of shallow aquifers from the Groundwater Bulletin of China Northern Plains (GBCNP), which is issued annually by the Ministry of Water Resources of China (MWR), and the Groundwater Bulletin of Hebei Plain (GBHP), which is issued quarterly by the Department of Water Resources in the Hebei Province (DWRHP) [MWR, 2010; DWRHP, 2010].

In addition, monthly precipitation data of China were obtained from China Meteorological Data Sharing Service System (CMDSSS) (available at: <http://cdc.cma.gov.cn/>). The spatial

resolution of the precipitation data is $0.5^\circ \times 0.5^\circ$.

3.2.4 Groundwater Model

Cao et al. [2013] built a multilayer, heterogeneous and anisotropic groundwater model to simulate the flow system in the NCP using MODFLOW-2000. This groundwater model was calibrated by historical groundwater level contour maps from 1960 to 1992 and monitoring water level time series from 1993 to 2008. Yearly GWS anomaly in shallow and deep aquifers were estimated in this groundwater model. Generally, extensive groundwater pumpage from deep aquifers will cause the ground subsidence, which can be used as the important constrains of groundwater modeling. However, considering the lack of land subsidence monitoring data in the NCP, the GWS anomaly in deep aquifers estimated by the model is significantly smaller than that in shallow aquifers, which might be significantly underestimated (personal communication, G. L. Cao). The time period of the model is from 1970 to 2008.

3.3 Results

The spatial pattern of TWS trends estimated from GRACE data for China and its surrounding regions from 2002-2013 is shown in Figure 3.2. The most obvious negative trend is located in northern India and Pakistan, which is believed to be caused by groundwater depletion [Rodell et al., 2009; Tiwari et al., 2009]. GRACE-derived glacial mass loss in the Himalayas and Tian Shan shown in the figure was discussed by Matsuo and Heki [2010]. As shown in Figure 3.2, the water impoundment in the Three Gorges Reservoir of China was also detected by GRACE [Wang et al., 2011]. Figure 3.2 also shows the obvious TWS loss in North China, specifically in Beijing, Tianjin, Hebei province, and Shanxi province.

Figure 3.3 shows the percentage of each 5-arc-minute grid cell equipped for irrigation with groundwater in North China [Siebert et al., 2010]. As shown in Figure 3.3, the high percentage of area equipped for irrigation with groundwater is mapped for the North China Plain, especially in the plains of Hebei province. We further investigated how much of the GRACE-derived TWS loss in North China is caused by groundwater depletion.

Figure 3.4 illustrates the time series of GRACE-derived TWS changes in North China, which show an obvious seasonal and interannual water storage variations. The TWS increase is detected in two different time periods, i.e., 2002-2004 and 2012-2013. A persistent mass loss is observed from 2004 to 2012. The averaged SMS+SWES changes from the land surface models showed a smaller amplitude than the GRACE-derived TWS changes. The time series from LSMs reflects rainfall anomalies rather well during the period (see precipitation data in Figure 3.7). The trend of SMS+SWES time series is 0.2 ± 0.1 cm/yr during 2002-2013, which is significantly smaller than that of TWS (-2.2 ± 0.3 cm/yr). On seasonal timescales, the highest TWS occurs in November, which lags SMS+SWES about 25 days.

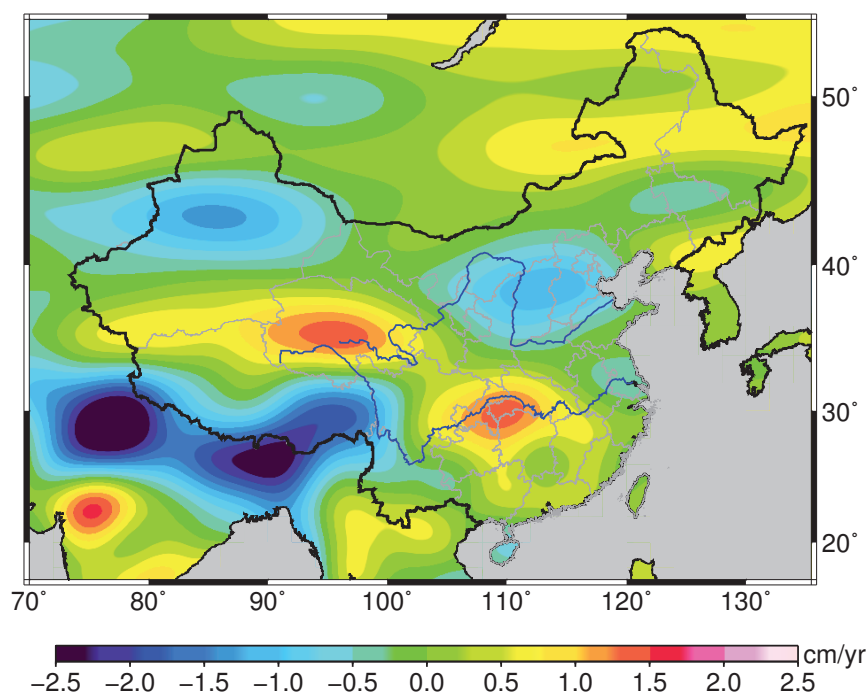


Figure 3.2: Trend map of terrestrial water storage (TWS) changes in China and its surrounding regions from GRACE during 2002-2013. Destriping and 200 km Gaussian smoothing were applied. In addition to the TWS loss in northern India and Pakistan, the figure shows the obvious TWS loss in North China.

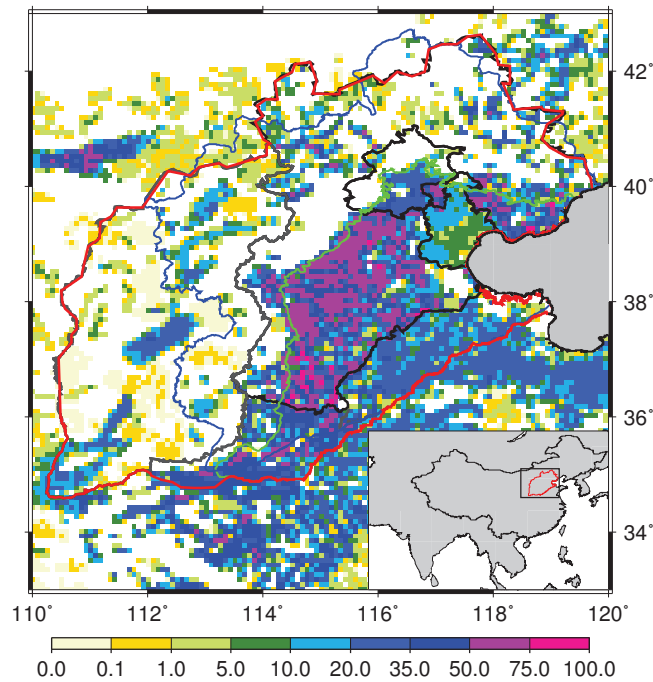


Figure 3.3: The area equipped for irrigation with groundwater in North China, given as a percentage of cell area, for $5' \times 5'$ cells [Siebert et al., 2010]. The high percentage of area equipped for irrigation with groundwater is mapped for the North China Plain.

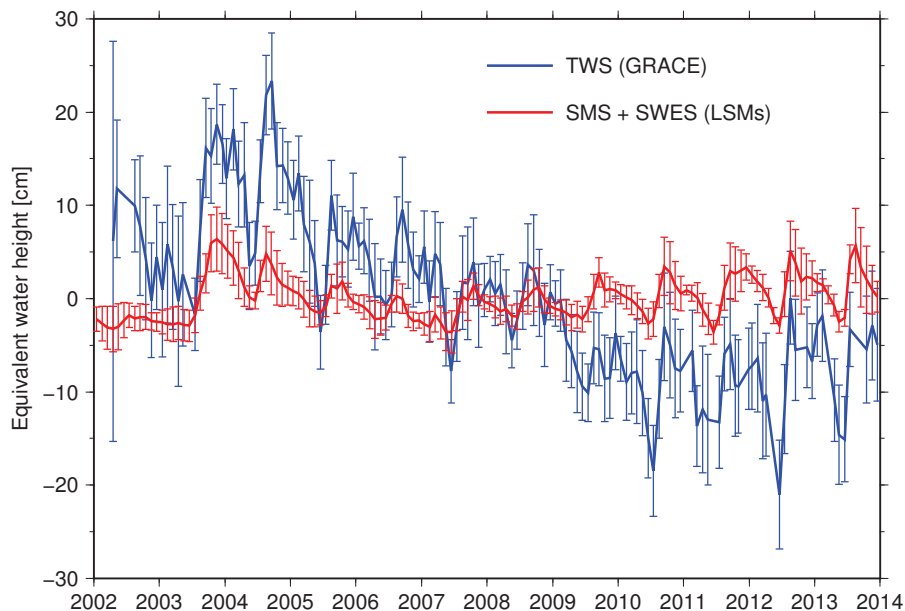


Figure 3.4: TWS variations estimated from GRACE and SMS+SWES variations estimated from seven LSMs (GLDAS_NOAH, GLDAS_VIC, GLDAS_CLM, GLDAS_MOSAIC, CPC, CLM4.5, and WGHM)

3.3.1 Seasonal GWS Variations

Figure 3.5 depicts the GWS changes estimated as the difference between GRACE-derived TWS and simulated SMS+SWES from LSMs, and the mean groundwater level changes observed by monitoring wells. These two independent groundwater change estimates agree with each other rather well both on seasonal and interannual timescales. Figure 3.6 further shows the seasonal monthly variations of groundwater storage, groundwater level, and precipitation in the study region. On seasonal timescales, the trough of GRACE-based GWS and groundwater level variations occurs in June/July. However, the precipitation peaks in July, which is in anti-phase with groundwater variations. GWS decreases rapidly from spring to summer, and is recovered continuously from summer to autumn and stabilized in winter. The recovery of GWS generally begins in July/August, when precipitation reaches maximum, which means a delayed response of groundwater to precipitation.

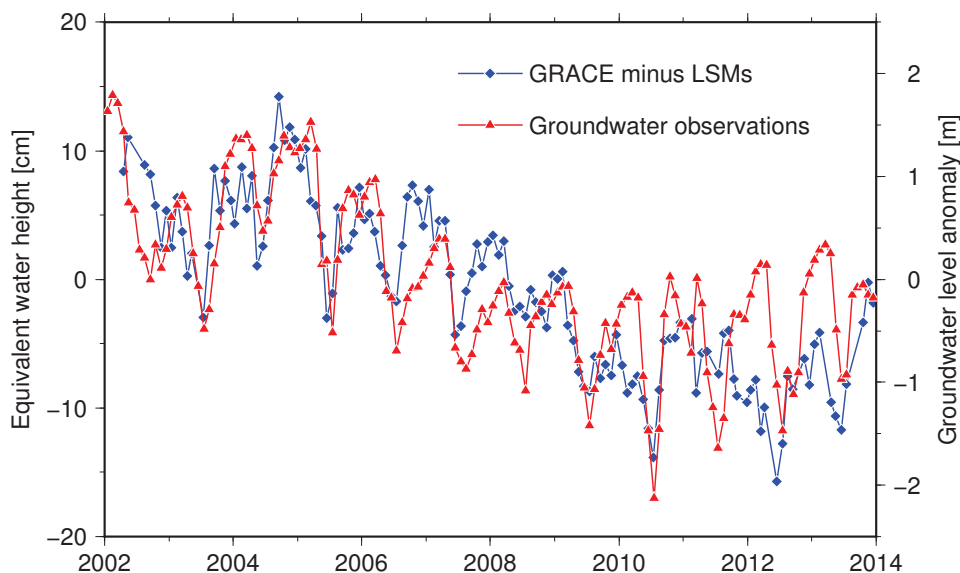


Figure 3.5: Comparison between monthly GWS variations estimated from GRACE minus LSMs and monthly groundwater level changes observed by monitoring wells during 2002-2013.

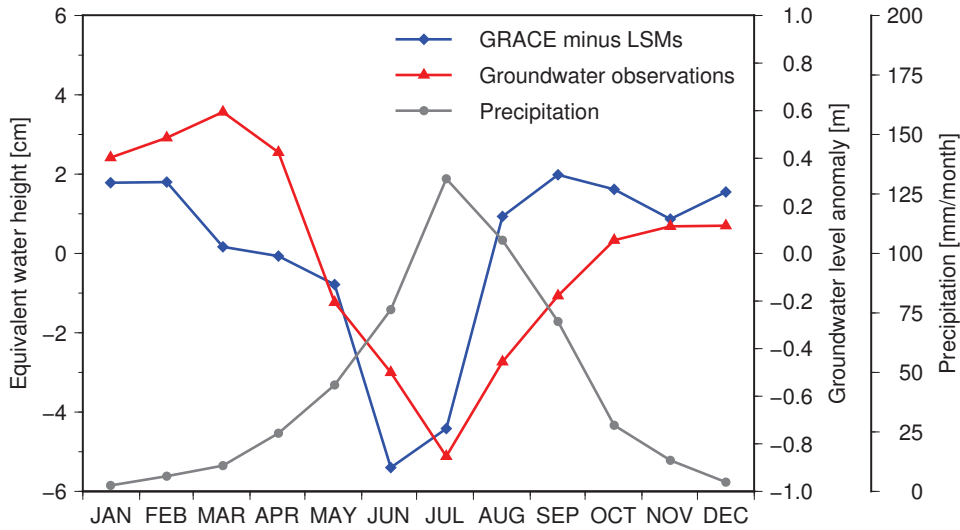


Figure 3.6: Seasonal monthly variations of groundwater storage, groundwater level, and precipitation in the study region during 2002-2013.

3.3.2 Interannual GWS Variations

To better understand the interannual GWS variations in North China, we further removed annual and semiannual cycles and applied a 3-month moving average to time series. As shown in Figure 3.7, GRACE-based GWS variations and groundwater level changes show a rapid groundwater depletion in 2002, which is consistent with the less precipitation in the same year. From 2003 to 2004, GRACE and ground monitoring wells observe a sharp increase of GWS, which agrees rather well with abundant precipitation in these two years. After that, groundwater level shows a persistent decrease from 2005 to 2010, and then increases again after 2010. There is a rather good agreement between interannual variations of GRACE-based GWS and that of groundwater level. From 2012 to 2013, obvious groundwater increase is detected by the two independent observations, which agree with the increase of annual precipitation in the same time period. It is worthwhile to note that, there are two main discrepancies between the two independent observations, i.e., from mid-2006 to mid-2008 and from late 2011 to 2012. They will be discussed in the Discussion of this chapter.

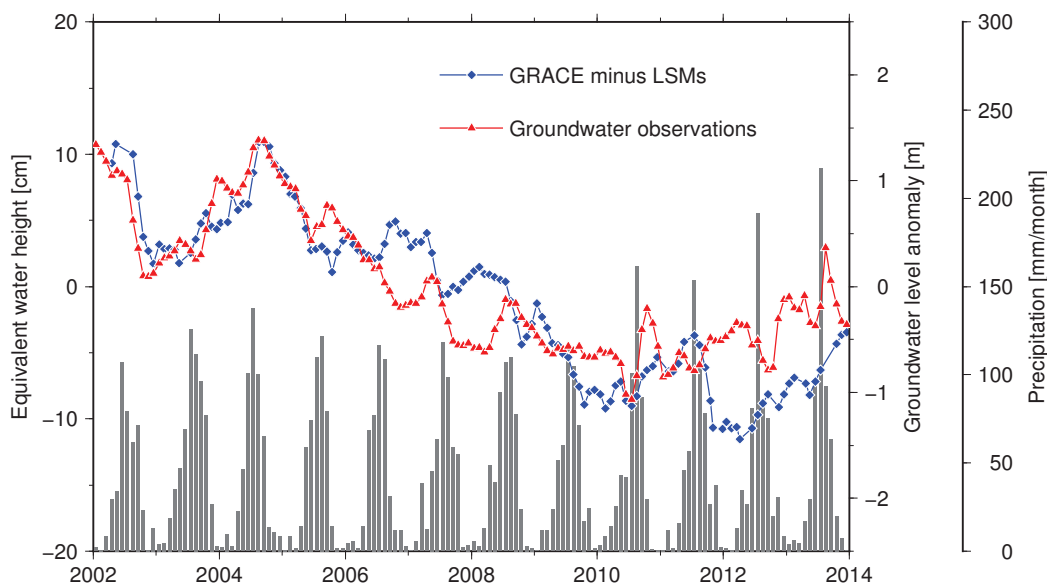


Figure 3.7: Interannual GWS variations derived by GRACE minus LSMs and interannual groundwater level changes observed by groundwater monitoring wells (same as the time series in Figure 3.5, but with annual and semi-annual cycles removed using least-square-fit and a 3-month moving average applied). Monthly precipitation in the study region is also shown.

Figure 3.8a shows the yearly GWS variations in mass estimated from GRACE minus LSMs, groundwater monitoring well observations, groundwater bulletins, and groundwater model. As shown in Figure 3.8a, although the interannual variations of groundwater level observed by monitoring wells is highly consistent with that of GRACE-based GWS (Figure 3.7), the GWS depletion rate in volume during 2002-2013 observed by monitoring wells, when converted to integrated mass, is significantly smaller than the estimate from GRACE minus LSMs. It is also the case for the estimates from groundwater bulletins and groundwater model. Yearly GWS variations in volume from groundwater monitoring well data were computed by converting the groundwater level changes to groundwater storage changes using the mean specific yield of NCP, and then multiplying it with the area of NCP. The original values from groundwater bulletins and groundwater model are given by yearly GWS depletion in volume. The groundwater level decline rate in the NCP observed by groundwater monitoring wells is -14.1 ± 1.1 cm/yr from 2002 to 2013, which is equivalent to -0.8 ± 0.1 cm/yr of GWS depletion rate (-1.2 ± 0.1 km³/yr in volume). As shown in Table 3.1, the GWS depletion rate released by groundwater bulletins from 2002 to 2013 is -2.0 km³/yr, which is still

smaller than the estimate from GRACE, i.e., $-7.1 \pm 1.0 \text{ km}^3/\text{yr}$. The GWS depletion rate over 2002-2008 estimated by the groundwater model is $-4.0 \text{ km}^3/\text{yr}$, which is in the estimation interval of GRACE-based result. However, the estimates from groundwater observations and groundwater bulletins are still significantly smaller than that from GRACE.

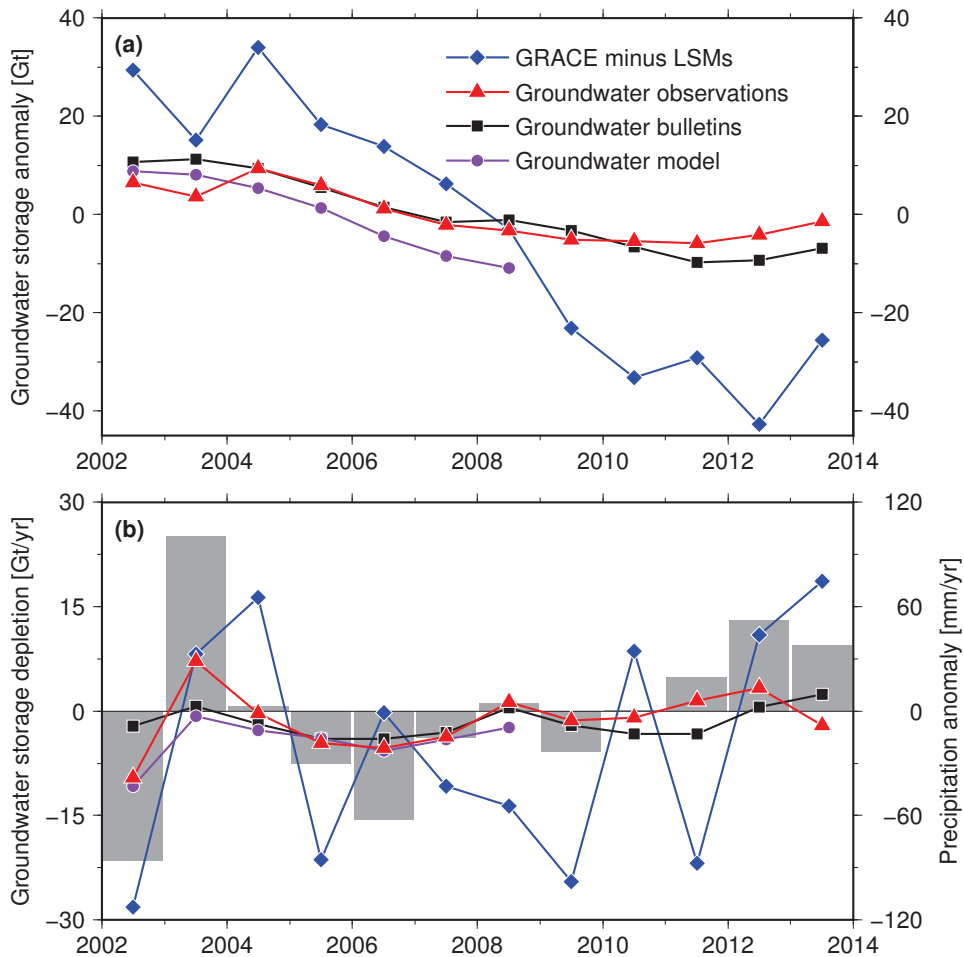


Figure 3.8: (a) Yearly GWS variations (in Gigatonne (Gt), which is equivalent to km^3) derived by GRACE minus LSMs, groundwater monitoring wells, groundwater bulletins, and groundwater model. (b) Yearly precipitation anomalies from CMDSSS and yearly GWS depletion, i.e., the GWS difference between the beginning and end of a given year, from GRACE minus LSMs, groundwater monitoring wells, groundwater bulletins, and groundwater model.

Table 3.1: Groundwater depletion rates (km^3/yr) estimated from GRACE minus LSMs, groundwater monitoring wells, groundwater bulletins, and groundwater model during 2002-2013 and 2002-2008.

	Observations	Bulletins	Model	GRACE
2002-2013	-1.2 ± 0.1	-2.0	–	-7.1 ± 1.0
2002-2008	-1.8 ± 0.2	-2.5	-4.0	-5.0 ± 1.8

Table 3.2: Yearly precipitation anomalies (mm/yr) and yearly groundwater depletion (Gt/yr) from groundwater observations, groundwater bulletins, and GRACE minus LSMs.

	Precipitation	Observations	Bulletins	GRACE-LSMs
2002	-86	-9.586	-2.187	-28.181
2003	101	7.165	0.662	8.206
2004	3	-0.336	-1.865	16.300
2005	-30	-4.563	-3.957	-21.398
2006	-63	-5.267	-3.955	-0.272
2007	-15	-3.695	-3.105	-10.773
2008	4	1.291	0.432	-13.665
2009	-23	-1.301	-2.077	-24.475
2010	0	-0.912	-3.307	8.643
2011	20	1.518	-3.277	-21.893
2012	52	3.31	0.541	10.911
2013	38	-2.097	2.431	18.635

To better evaluate year-over-year GWS variations, we further calculated the yearly GWS change in volume between the beginning and end of a given year. The GWS change at the beginning or end of a given year is the average of GWS variations in December of previous year and that in January of this year. As shown in Figure 3.8b and Table 3.2, in general, when yearly precipitation anomaly is negative, the yearly GWS depletion is also negative; and vice versa. It is especially the case for results from groundwater observations and groundwater

bulletins. Considering the results from groundwater observations and groundwater bulletins only represent the GWS anomalies in shallow aquifers, good agreement between year-over-year precipitation and GWS indicates the response of groundwater in shallow aquifers to the precipitation. The yearly GWS depletion from GRACE minus LSMs is still significantly larger than that from groundwater observations and bulletins. The discrepancy between them may indicate the effect the GWS change in deep aquifers.

As shown in Figure 3.9, the yearly groundwater level variations from groundwater monitoring wells indicates large groundwater decline in the piedmont region of the NCP, especially in Hebei province. Figure 3.10 shows the spatial pattern of specific yields in the NCP. Figure 3.11 demonstrates the spatial patterns of yearly GWS variations from groundwater monitoring wells, which show the similar distribution to those from groundwater level variations. In order to compare with GRACE results, we further filtered the results in Figure 3.11 in the same way as GRACE data processing (i.e., projection of grids to spherical harmonic coefficients, truncation to d/o 60, application of destriping and 200 km Gaussian filtering). As shown in Figure 3.12 and Figure 3.13, spatial patterns of yearly GWS variations from groundwater observations and GRACE minus LSMs agree with each other rather well, although the magnitude of estimates from groundwater observations is generally smaller than that from GRACE minus LSMs. Based on the results from GRACE minus LSMs, GWS change reaches minimum in 2012, and increases after that. Results from groundwater observations also show the GWS increase from 2012 to 2013, which agree with those from GRACE minus LSMs.

As shown in Figure 3.14, the yearly GWS variations from groundwater model also indicates the large GWS loss in the piedmont region of the NCP from 2002 to 2008. However, the magnitude of GWS estimates from groundwater model is larger than that from groundwater observations, which is also confirmed by results in Table 3.2.

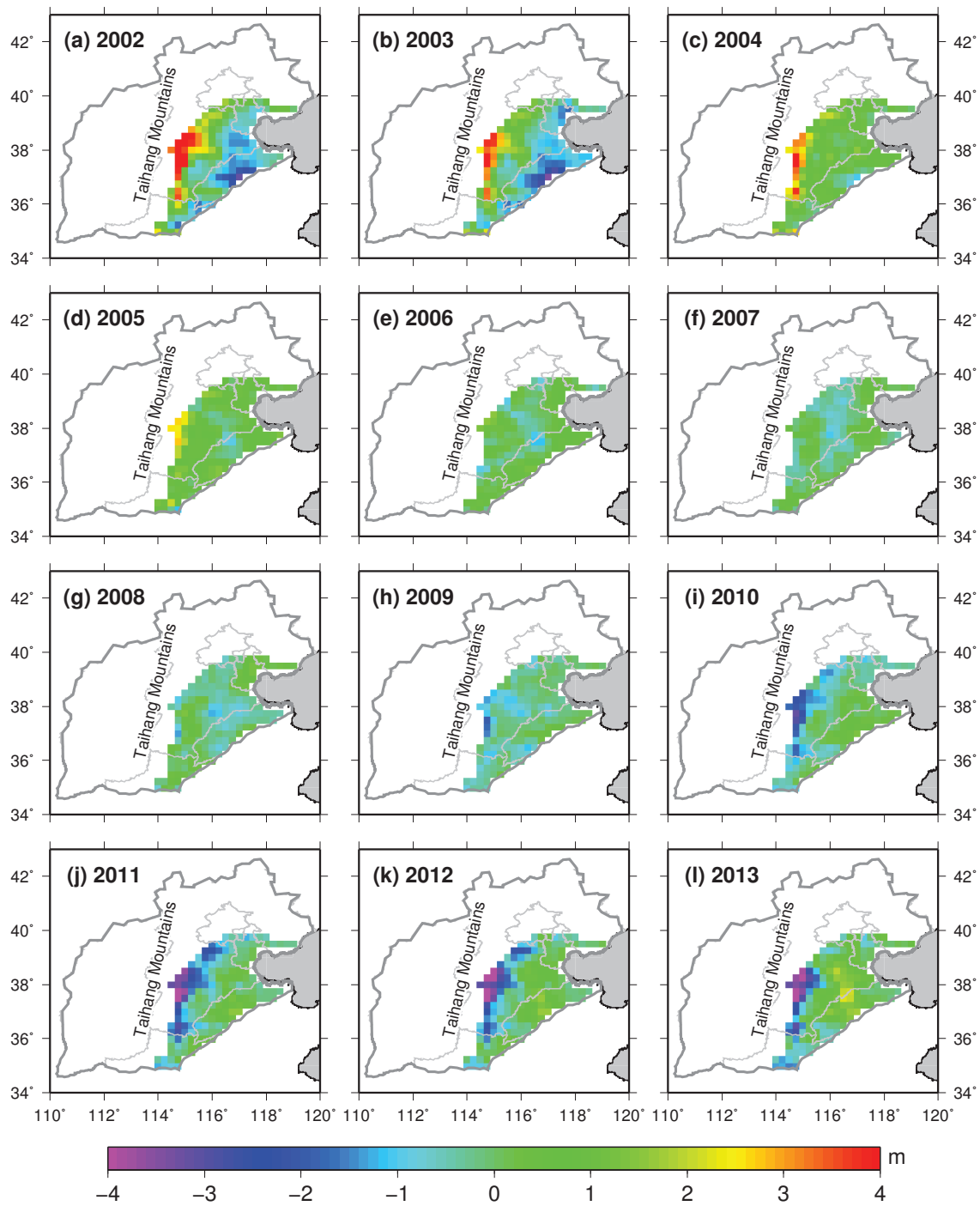


Figure 3.9: Spatial patterns of yearly groundwater level variations from groundwater monitoring wells.

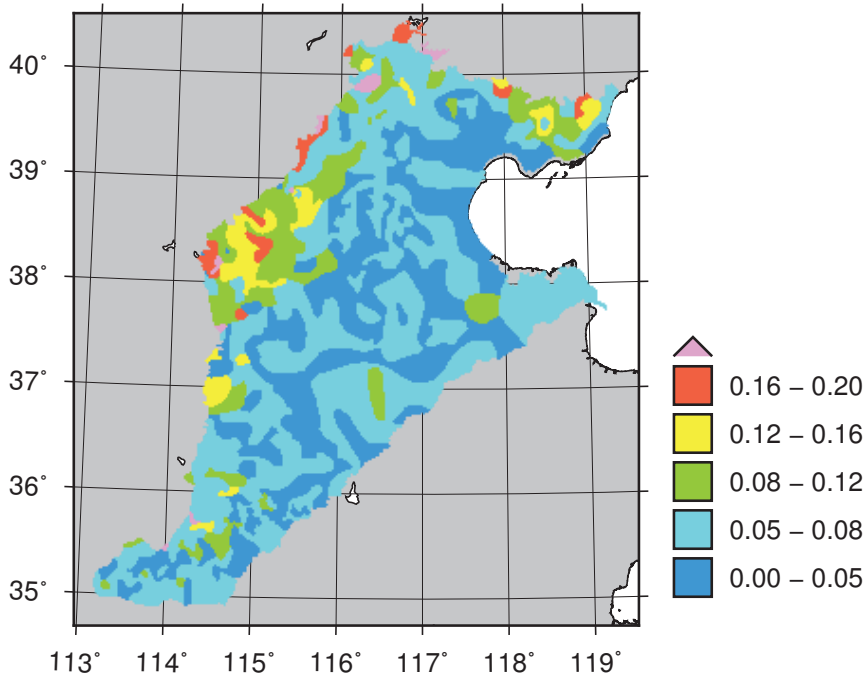


Figure 3.10: Spatial pattern of specific yields in the NCP (modified from Zhang and Fei [2009]).

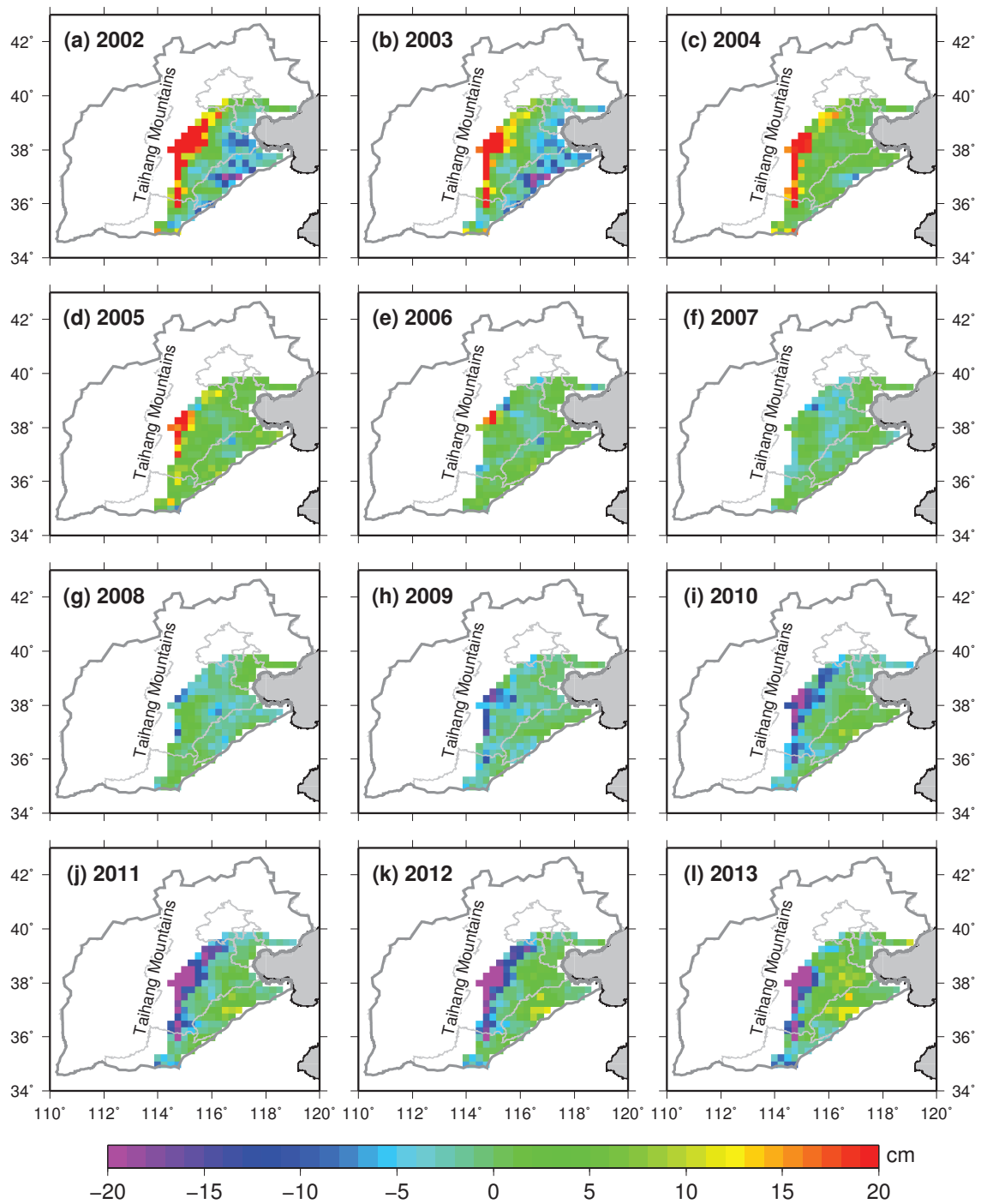


Figure 3.11: Spatial patterns of yearly GWS variations from groundwater monitoring wells.

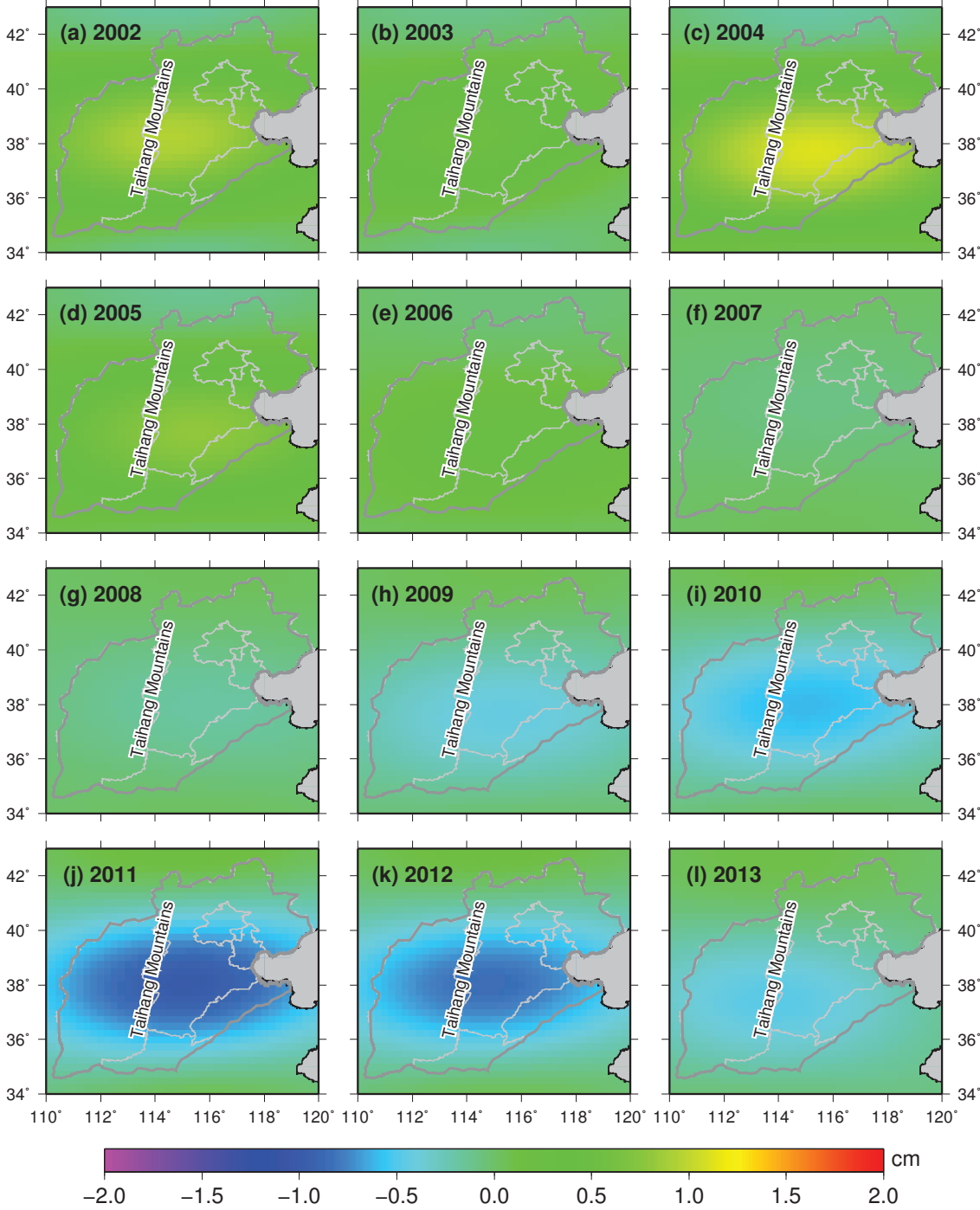


Figure 3.12: Spatial patterns of yearly GWS variations from groundwater monitoring wells at GRACE resolution.

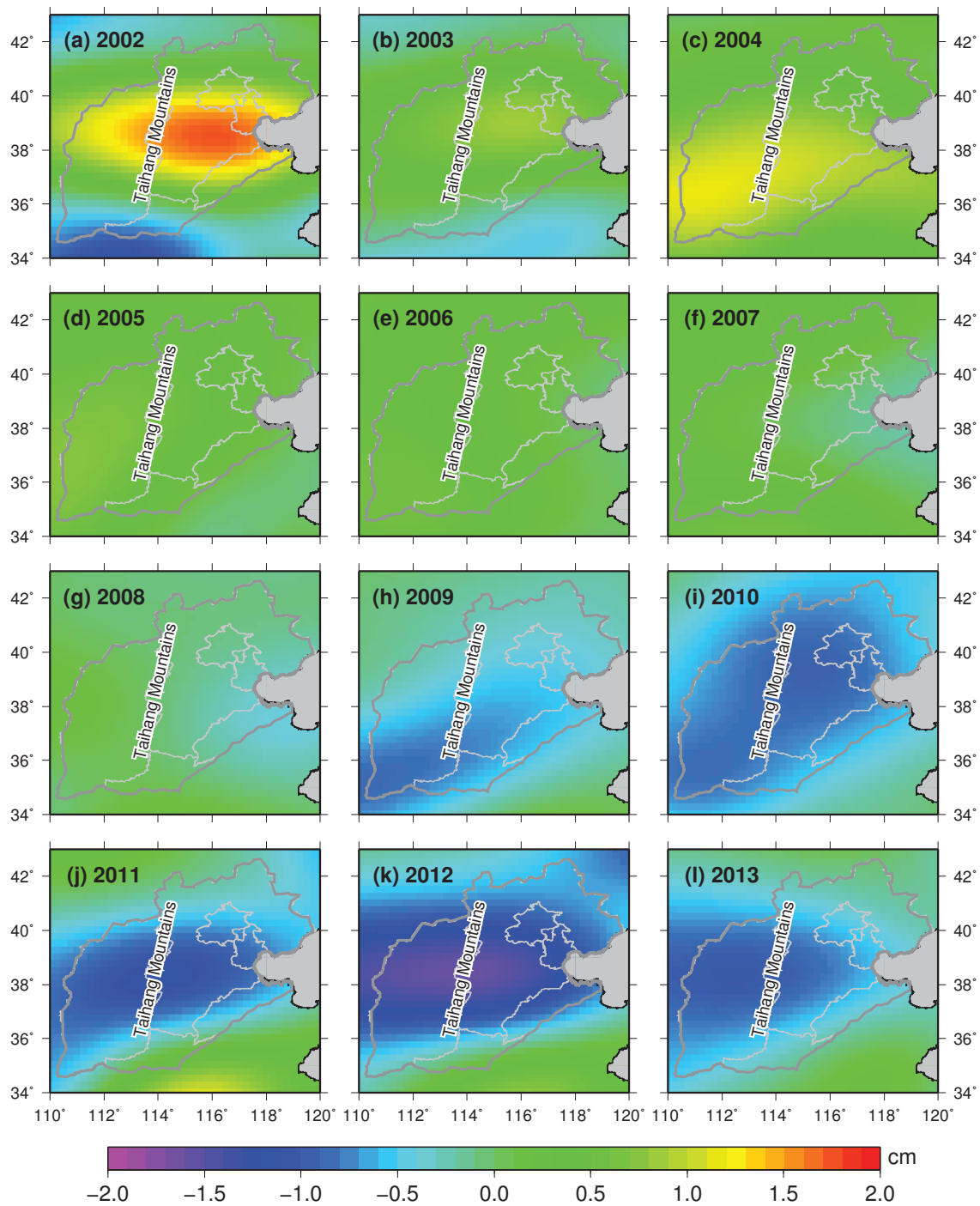


Figure 3.13: Spatial patterns of yearly GWS variations from GRACE minus LSMs.

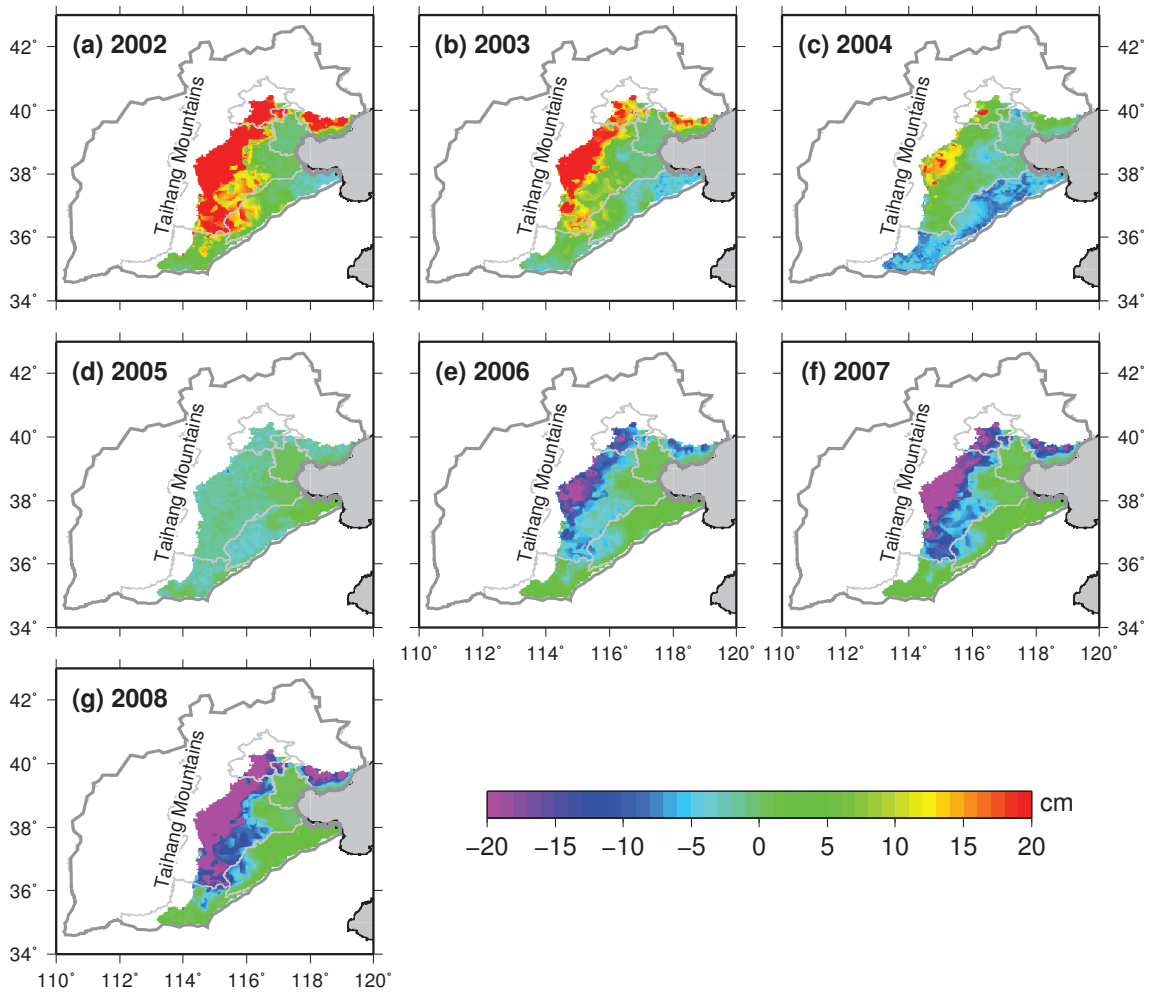


Figure 3.14: Spatial patterns of yearly GWS variations from groundwater model.

3.3.3 Long-term GWS Variations

As shown in Figure 3.15a, the GRACE-based GWS trend showed the largest groundwater depletion in the piedmont region of the Taihang Mountains, where irrigation relies heavily on groundwater [Kendy et al., 2003; Siebert et al., 2010; Yang et al., 2010]. The spatial pattern of the GWS trend estimated from groundwater monitoring wells also demonstrates obvious groundwater depletion in the piedmont region of the Taihang Mountains, especially in Hebei province (Figure 3.15b). However, based on groundwater monitoring well data, GWS increases at a rate of about 1 cm/yr in the eastern part of the study region from 2002 to 2013. To make the GWS trend map estimated from groundwater observations consistent with that

from GRACE minus LSMs, we then transformed the gridded GWS trend map from groundwater observations to the SH domain, truncated to d/o 60, destriped, and smoothed with a 200 km Gaussian filter. As shown in Figure 3.15a and c, the spatial pattern of GWS trend map derived from groundwater observations at GRACE spatial resolution agrees rather well with the GRACE-based results. Note that the magnitude of GWS trend map from groundwater observations is smaller than that from GRACE minus LSMs. The possible GWS changes in deep aquifers are not included in Figure 3.15b. The groundwater depression cones in shallow aquifers are mainly located in the piedmont region of the Taihang Mountains, whereas most of the groundwater depression cones in deep aquifers are located in the central plain region of Hebei province (Figure 3.15c) [Ministry of Land and Resources of China, 2009]. Although the spatial resolution of groundwater depletion from GRACE data is limited to approximately 300 km, there is a good correlation between the location of GRACE-observed groundwater depletion and that of groundwater depression cones, which confirms that GRACE does observe the groundwater depletion occurring in North China.

For the time period of 2002-2008, the spatial patterns of GWS trend from filtered groundwater observations and ground model are also generally consistent with that from GRACE minus LSMs (Figure 3.16).

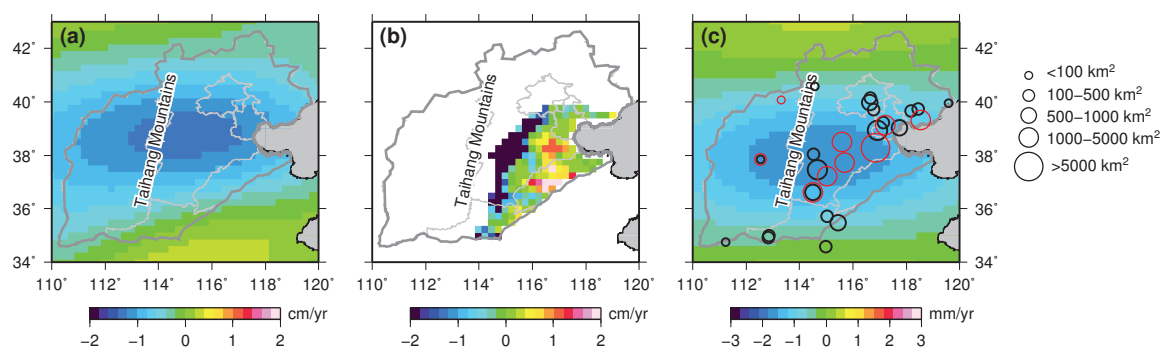


Figure 3.15: Spatial patterns of GWS trends estimated from (a) GRACE minus LSMs, (b) groundwater observations, and (c) filtered groundwater observations from 2002 to 2013. The location and size of groundwater depression cones in shallow aquifers (black circles) and deep aquifers (red circles) are also shown in panel (c).

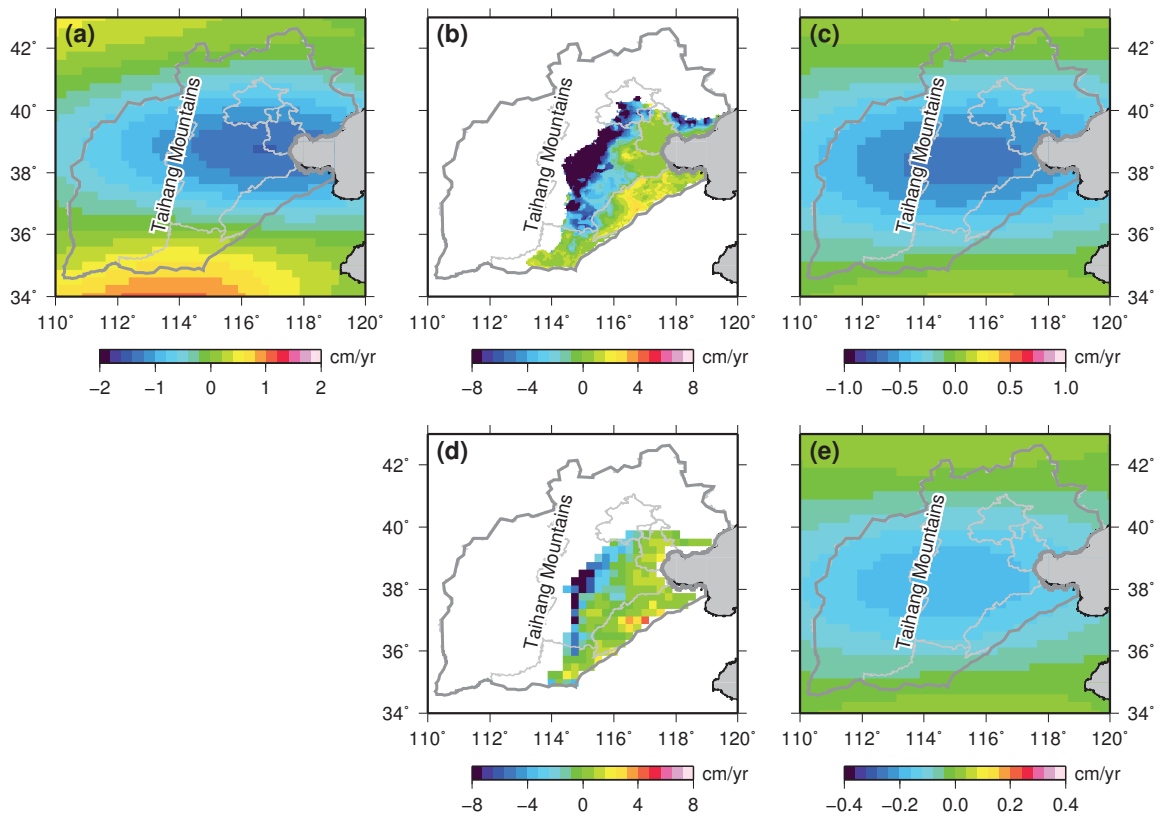


Figure 3.16: Spatial patterns of GWS trends estimated from (a) GRACE minus LSMs, (b) groundwater model, (c) filtered groundwater model, (d) groundwater observations, and (e) filtered groundwater observations from 2002 to 2008.

Figure 3.17 shows locations of cities in the North China Plain. As shown in Figure 3.18a, the rates of groundwater level decline in cities, which are located in the piedmont region of Hebei province, are significantly larger than those in cities located in the central plain and coastal region of the NCP. The largest groundwater level decline is located in Shijiazhuang, at a rate of -1.1 m/yr. As shown in Figure 3.18b, the groundwater levels in cities of Henan province and Shandong province do not show significant decline as those in cities of Hebei province. The time series of groundwater level changes in Liaocheng, Dezhou and Binzhou show a significant jump at the end of 2010, which correspond to the increase of precipitation in the same year rather well. Results in Figure 3.18 are consistent with the spatial pattern of GWS trends estimated from groundwater observations (Figure 3.15b).

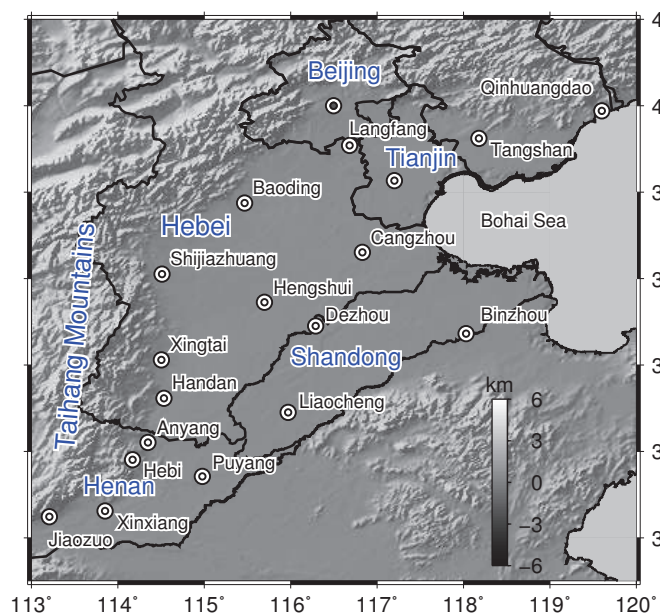


Figure 3.17: Locations of cities in the NCP.

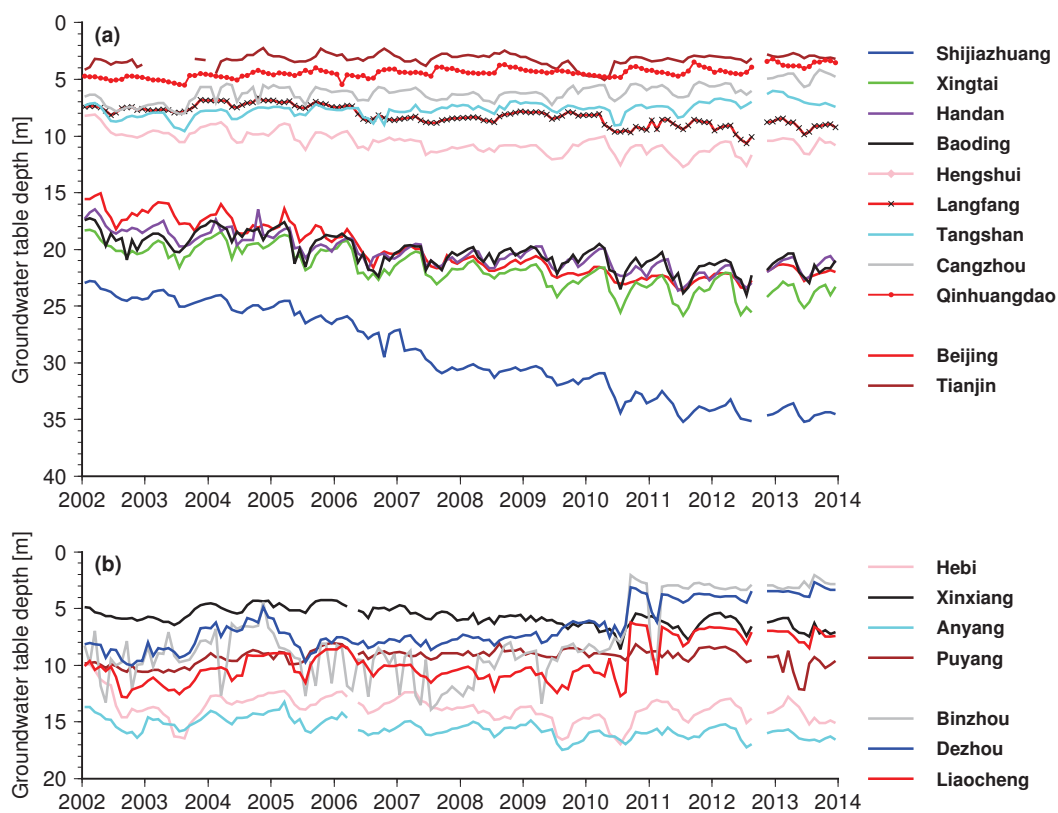


Figure 3.18: Groundwater level changes in cities of the NCP.

3.3.4 Error Estimation of GRACE-based GWS Variations

Although GRACE shows the great potential in monitoring groundwater storage variations in many parts of the world, the uncertainties related to GRACE results are still very high and should be assessed carefully. Firstly, considering the polar orbit design of GRACE satellites and observation errors of GRACE's payload, there are systematic error and random noise in GRACE resolutions. In spatial domain, systematic error is shown as so-called "north-south stripes". In order to reduce these stripes, researchers devised some destriping methods [Chambers, 2006; Chen et al., 2006; Duan et al., 2009; Swenson and Wahr, 2006]. In addition, many filters are devised to reduce the random noise of GRACE results, e.g., classic Gaussian filter [Jekeli, 1981; Wahr et al., 1998], non-isotropic filter [Han et al., 2005], statistical filter [Davis et al., 2008], DDK filter [Kusche, 2007], wavelet filter [Schmidt et al., 2006], wiener filter [Sasgen et al., 2007], fan filter [Zhang et al., 2009], and so on. The error of GRACE observations and the uncertainty of GRACE data processing related to different smoothing methods should be considered. Secondly, in order to estimate GWS variations, other components of TWS should be estimated and removed from GRACE observations, i.e., soil moisture storage, surface water reservoir storage, and snow water equivalent storage. In fact, nearly all of the major rivers in North China are dammed for municipal and industrial use. The surface water reservoir storage change and snow water equivalent storage change are negligible on interannual and long-term timescales [Han et al., 2008]. The snow water equivalent storage change estimated from LSMs is also negligible. The largest uncertainty exists in soil moisture storage. In this section, the uncertainty of soil moisture storage variation in our study region is assessed using the standard deviation of different LSMs' SMS outputs.

We considered the uncertainty of GWS changes derived from GRACE minus LSMs. As summarized by Longuevergne et al. [2010], the errors induced by the GRACE data processing include the scaled GRACE measurement error ($k\Delta\hat{S}_0$), the error due to leakage correction ($k\Delta S_{leakage}$), and the uncertainty of the scaling factor ($\Delta k\hat{S}_0$ and $\Delta kS_{leakage}$). The error from hydrological models, processing error from applying Gaussian smoothing with different radii and different destriping methods, and the error from GIA were also considered here.

To estimate GRACE measurement error, we used the method proposed by Chen et al. [2009b]. The measurement error was determined from root-mean-square variability over the Pacific Ocean at the same latitude as the North China, in which true mass variation should be small, as barotropic ocean mass variations have been removed by the de-aliasing process. A potential limitation of the scaling method is how mass change is distributed inside the basin. We applied the mass distribution within the study area determined from five hydrological models and under uniformity assumption to estimate the uncertainty of the scaling method (Table 3.3). Based on our simulation, we conclude that the uncertainty of the scaling factor estimation (Δk) is less than 5%, which we included in our final error budget. Based on the GWS trends estimated by applying Gaussian smoothing with different radii and applying different destriping methods, we concluded that the uncertainty of GRACE data processing is about 0.12 cm/yr, which is included in our final error budget too (Table 3.4). The GIA effect in our study area is approximately 0.19 cm/yr. We pessimistically assumed that the uncertainty of the GIA correction was $\pm 50\%$ and thus 0.10 cm/yr.

Table 3.6 lists the different error components in the final error budget of monthly GWS estimates and the trend. As shown in Table 3.6, the errors primarily result from the SMS error, GRACE measurement error, processing error, and leakage error. The LSMs used in this study only simulate SMS above 2 m. There might be significant variations in unsaturated water storage below 2 m, which would not be included in the hydrological models. This is especially true for the western part of the Hebei province, where the mean water table depth is usually tens of meters [Foster et al., 2004]. Therefore, the unmodeled SMS could lead to errors in our final groundwater estimate. The error from leakage corrections estimated from hydrological models might be underestimated as well. The final error estimate of the GWS trend based on GRACE and LSMs was 0.24 cm/yr, based on the assumption that no correlations exist between the individual trend errors.

Figure 3.19 shows the time series of GWS variations in our study region estimated from different GRACE products released by CSR, GFZ, JPL, and GRGS. Groundwater depletion rates in North China estimated from CSR, GFZ, and JPL are 1.57 ± 0.24 , 1.60 ± 0.24 , and 1.58 ± 0.24 cm/yr, respectively, for 2002-2013. Estimate from GRGS is 1.36 ± 0.30 cm/yr

for 2003-2012, for which a scaling factor of 0.84 is applied. The spatial patterns of GWS trends for 2002-2013 obtained from CSR, GFZ, and JPL GRACE data agree well with each other (Figure 3.20).

Figure 3.21a is the duplicate of Figure 3.19a, but for the period of 2003-2012. Destriping and 200 km Gaussian smoothing is applied to CSR RL05 GRACE data in Figure 3.21a. In Figure 3.21b, only 200 km Gaussian smoothing is applied. The difference between Figure 3.21a and b indicates the effect of destriping on spatial pattern of GWS trends. Figure 3.21c demonstrates the spatial pattern of GWS trends from GRGS RL03 GRACE data from 2003-2012. The difference between CSR and GRGS results indicates that uncertainty still remains within GRACE products derived using different gravity field inversion strategies.

Table 3.3: Scaling factors for rescaling TWS time series estimated from uniformity assumption, four GLDAS models (NOAH, VIC, CLM, and MOSAIC) and the CPC model over 2002-2013. SH expansion, destriping, kernel function and Gaussian smoothing with different radii are applied to simulate GRACE data processing. The mean values with different radii are shown in the last column. Obviously, the remaining signal in the basin will be attenuated significantly when we apply a large Gaussian smoothing radius. Therefore, the biggest scaling factor is retrieved when the largest Gaussian smoothing radius is applied. With the same Gaussian smoothing radius, the estimates from different models are consistent with each other. Based on the simulation, we conclude that the uncertainty of scaling factor estimation (Δk) is smaller than 5%, which we include in our final error budget.

	Uniformity assumption	NOAH	VIC	CLM	MOSAIC	CPC	Mean
300 km	3.12	3.20	3.23	3.16	3.27	3.15	3.19
250 km	2.78	2.84	2.87	2.80	2.91	2.80	2.83
200 km	2.51	2.55	2.58	2.51	2.62	2.52	2.55
150 km	2.29	2.32	2.35	2.28	2.39	2.29	2.32
100 km	2.14	2.16	2.19	2.12	2.23	2.14	2.16
50 km	2.04	2.07	2.09	2.02	2.13	2.04	2.07
0 km	2.01	2.03	2.06	1.99	2.10	2.01	2.03

Table 3.4: GRACE data processing error of applying Gaussian smoothing with different radii and applying different destriping methods on the trend estimation. Trend estimates of groundwater depletion corresponding to different Gaussian smoothing radii and different destriping methods in GRACE data processing are computed (unit: mm/yr). We compared three destriping methods, proposed by Swenson and Wahr [2006], Duan et al. [2009], and Chen et al. [2006]. The uncertainty of these estimates is 1.2 mm/yr, which we included in our final error budget as the uncertainty of GRACE data processing error. Scaling factors adopted for rescaling GWS time series are shown in Table 3.5.

	Swenson	Duan	Chen
300 km	-16.3	-16.8	-15.8
250 km	-16.4	-16.2	-14.9
200 km	-16.3	-15.7	-13.9
150 km	-16.2	-15.2	-13.0
100 km	-16.0	-14.8	-12.4
50 km	-15.9	-14.5	-11.9
0 km	-15.8	-14.4	-11.8

Table 3.5: Scaling factors for rescaling GWS time series with different destriping methods and different radii of Gaussian smoothing. We adopted gridded groundwater observations released by MWR to estimate these scaling factors. SH expansion, destriping, kernel function and Gaussian smoothing with different radii are applied to simulate GRACE data processing. We adopt the Swenson’s destriping method in this study, since it’s widely used to estimate terrestrial water storage changes and groundwater storage changes.

	Swenson	Duan	Chen
300 km	2.59	2.16	2.12
250 km	2.26	1.88	1.79
200 km	1.99	1.64	1.53
150 km	1.78	1.46	1.33
100 km	1.63	1.34	1.20
50 km	1.55	1.27	1.12
0 km	1.52	1.24	1.09

Table 3.6: Different error components in the final error budget of monthly GWS estimates and the trend. Processing error represents the uncertainty of applying Gaussian smoothing with different radii and applying different destriping methods. Uncertainties in the trends were estimated by applying a least squares fit through the error propagation from the monthly data using a covariance matrix. The final error estimate of the GWS trend based on CSR RL05 GRACE data and LSMs was 0.24 cm/yr, under the assumption that no correlations exist between the individual trend errors.

		Monthly (cm)	Trend (cm/yr)
TWS (GRACE)	Measurement error ($k\Delta\hat{S}_0$)	3.84	0.11
	Leakage ($k\Delta S_{leakage}$)	2.64	0.07
	$\Delta k\hat{S}_0$	<1.39	0.04
	$\Delta kS_{leakage}$	<0.33	0.01
	Processing error	–	0.12
	GIA	–	0.1
	Total	4.87	0.21
SMS+SWES	Land surface models	4.26	0.12
GWS	GRACE-LSMs	6.47	0.24

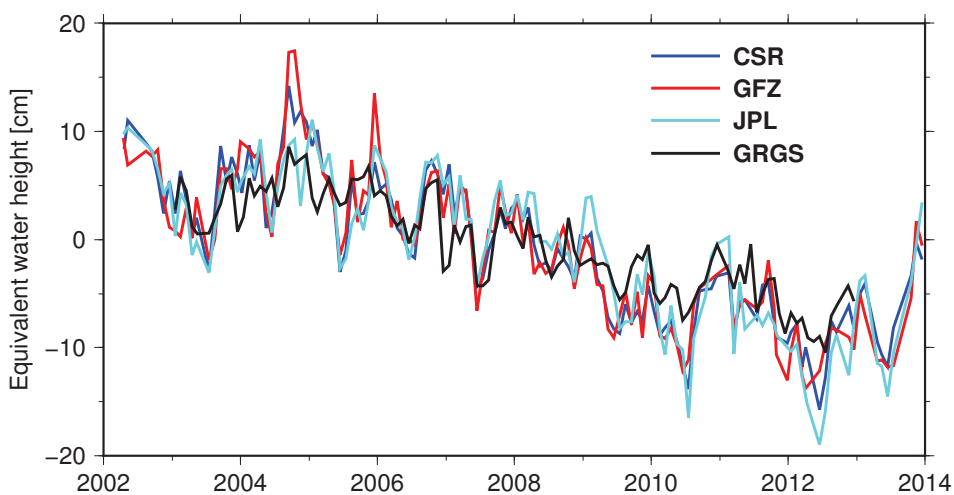


Figure 3.19: Interannual GWS variations based on CSR, GFZ, JPL, and GRGS GRACE products and LSMs.

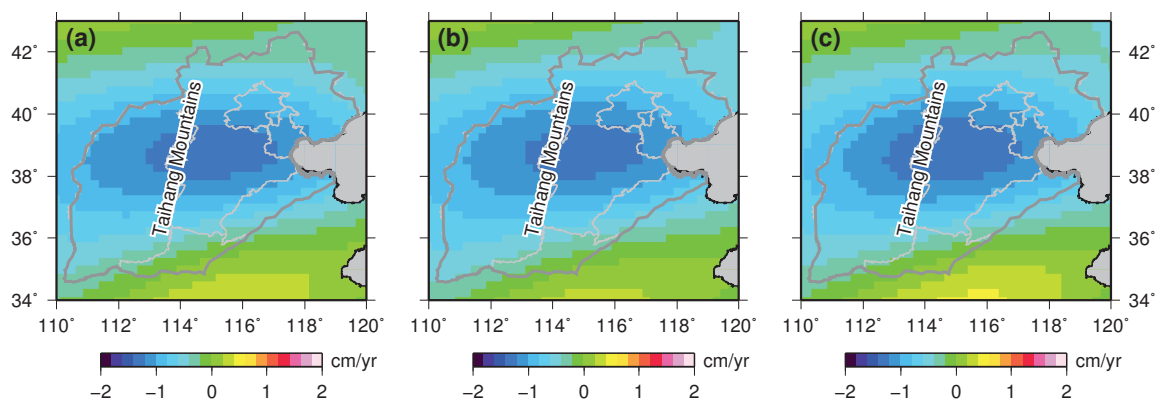


Figure 3.20: Spatial patterns of GWS trends estimated from (a) CSR, (b) GFZ, and (c) JPL GRACE products from 2002 to 2013.

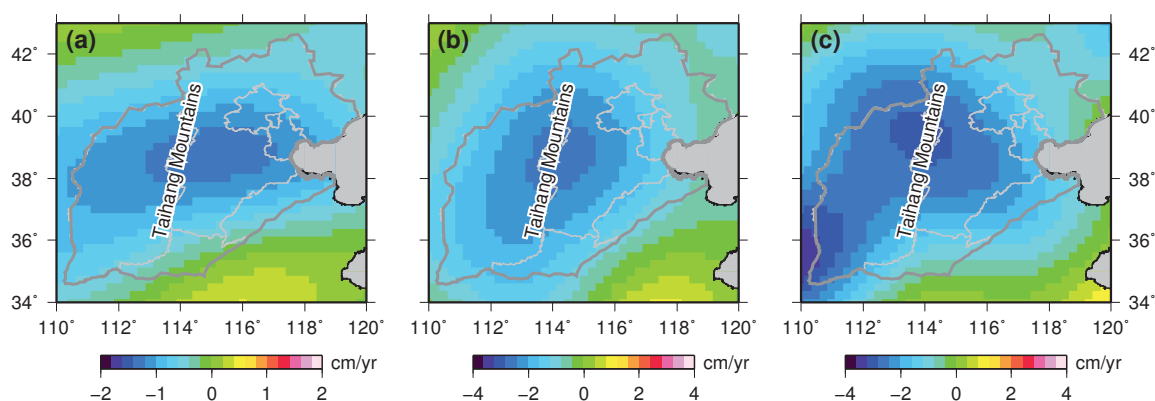


Figure 3.21: Spatial patterns of GWS trends estimated from (a) CSR GRACE data with destriping and 200 km Gaussian smoothing applied, (b) CSR GRACE data with only 200 km Gaussian smoothing applied, and (c) GRGS GRACE products without destriping and Gaussian smoothing from 2003 to 2012.

3.3.5 Discussion

North China Plain is one of largest agricultural production zone in China. Winter wheat and summer maize are the two staple crops in the NCP. Winter wheat is generally sown in October and harvested in June, while maize occupies the field from the middle of June to the end of September. Generally, the seedling stage of winter wheat is completed in November. From November to February, water requirement by winter wheat is very low owing to the low winter temperature [Yang et al., 2006]. In March, wheat begins to turn green. After that, wheat experiences the stage of jointing, booting, flowering, and grain filling from April to June, i.e.,

the growing season of wheat. More than 70% of irrigation water is consumed during the wheat growing season, which mainly stems from groundwater pumping. As shown in Figure 3.6, GRACE-based GWS and groundwater level variations show the rapid groundwater decline from spring to early summer, due to the extensive wheat irrigation with groundwater pumping. Although the seasonal monthly precipitation climbs from nearly zero to about 130 mm during January to July, the groundwater continues to decrease for the same period because of crop irrigation. So, we conclude that anthropogenic effect, i.e. irrigation, is the main factor of groundwater decline in the NCP from spring to summer. After the harvest of winter wheat in June, drought-tolerant maize is cultivated. The demand of groundwater-based irrigation begins to decrease after June/July so that groundwater aquifers are recharged during the rainy summer and groundwater storage increases continuously until stabilized in winter and spring of next year (shown in Figure 3.6). Note that the response of groundwater to precipitation has a delay because of the infiltration effect of precipitation to groundwater aquifers. Based on the above discussion, we conclude that both anthropogenic irrigation and natural precipitation contribute to climatological groundwater storage change in North China. From spring to summer, the groundwater decline is mainly caused by the extensive irrigation for wheat. From summer to winter, the groundwater aquifers are recharged gradually due to natural precipitation.

On interannual timescales, time series of GRACE-based GWS variations and groundwater level change agree with each other rather well (Figure 3.7). Interannual groundwater variations estimated from two independently groundwater observations agree well with year-over-year precipitation anomalies. The discrepancy on interannual timescales between these two independent estimates occurs in two periods, i.e., from mid-2006 to mid-2008 and from late 2011 to 2012. Note that groundwater observations only represent the groundwater level changes in shallow aquifers of NCP. However, GWS variations from GRACE minus LSMs represent the whole groundwater change information which also includes the change of groundwater storage in deep aquifers of NCP. This may explain the differences of groundwater changes in these two periods. For example, GRACE observes a sharp GWS decline from 2011 to 2012 in North China, which may mainly represent the groundwater depletion in deep aquifers. However, the groundwater level changes from observations of shallow aquifers shows a persistent

increase after 2010, when the annual precipitation begins to increase. Obviously, the recharge from precipitation for deep aquifers lags than that for shallow aquifers. It can explain the decline of GRACE-based GWS from late 2011 to 2012 well. In addition, these discrepancies may reflect uncertainties in GRACE, LSMs and groundwater monitoring well data. Except these two short-period discrepancies, GRACE and ground observations agree with each other very well. From 2012 to 2013, both GRACE and ground observations detect a GWS increase, which agree with the continued increase of precipitation.

Our final estimate of the groundwater depletion rate in North China based on GRACE data and land surface models was 1.57 ± 0.24 cm/yr for 2002-2013, which is equivalent to a volume rate of 7.1 ± 1.0 km³/yr. For the same time period, the estimated groundwater depletion rate in shallow aquifers according to the groundwater bulletins was approximately 2.0 km³/yr, which is less than one-third of our estimate. The estimate from groundwater monitoring well data was even smaller, i.e., -1.2 ± 0.1 km³/yr. One of the main reasons for these differences is that the ground-based estimate includes only groundwater information in shallow aquifers of China northern plains, whereas the GRACE observes all GWS changes from all aquifers. Some studies have shown that the deep groundwater table is also decreased greatly in the piedmont region of the Taihang Mountains and the central plain region of Hebei province [World Bank, 2001; Foster et al., 2004; Tamanyu et al., 2009]. The high groundwater depletion rate estimated using GRACE data indicates the important contribution of groundwater depletion in deep aquifers of North China. In addition, the contribution of possible groundwater depletion in the mountain areas of North China is not included in the GBCNP. The mountain areas of Shanxi province are among the largest coal-producing regions in China. Large-scale coal mining processes could destroy the aquifers and result in the observed groundwater depletion. However, determining the effect of coal mining processes on groundwater depletion is beyond the scope of the current study. Recently, Konikow [2011] estimated the contribution of global groundwater depletion since 1900 to sea level rise. Based on groundwater level measurements and groundwater flow models, cumulative net groundwater depletion in the NCP was found to be 130.3 km³ and 170.3 km³ for the 1900-2000 and 1900-2008 periods, respectively, which indicates that the groundwater depletion rate was 5 km³/yr from 2001-2008. Our estimate

based on GRACE data was $5.0 \pm 1.8 \text{ km}^3/\text{yr}$ for 2002-2008. Although the two time periods are not the same, our GRACE-based estimate is consistent with that reported by Konikow [2011]. Note that GRACE-based GWS increased after 2012, which leads to the difference in GRACE-based groundwater depletion rates between 2002-2008 and 2002-2013. Based on the above analysis, we conclude that the current depletion of groundwater resources in North China is more serious than previously reported in official groundwater bulletins.

The spatial pattern of groundwater depletion based on GRACE data shows significant groundwater loss in the piedmont and central plain regions of North China. In these regions, numerous studies have reported the consequences of groundwater depletion, such as groundwater depression, land subsidence, soil salinization, groundwater pollution, and seawater intrusion [Foster and Chilton, 2003; Foster et al., 2004; Liu et al., 2002; Shah et al., 2000; Wang et al., 2007], and demonstrated that extensive groundwater-based irrigation is the main cause of groundwater depletion in North China [Foster et al., 2004; Kendy et al., 2004].

3.3.6 Summary

GRACE satellite gravimetry offers an important approach to estimate GWS changes in North China. In this study, regional groundwater depletion in North China was estimated from GRACE-derived TWS and simulated SMS+SWES data during 2002-2013. The estimate was compared with in situ water table observations, groundwater bulletins and groundwater model. On seasonal timescales, groundwater variations respond to the combined effect of anthropogenic irrigation (discharge of groundwater aquifers from spring to summer) and natural precipitation (recharge of groundwater aquifers from summer to winter). On interannual timescales, groundwater variations are consistent with precipitation variations. Based on the GRACE-derived TWS and simulated SMS+SWES estimates, the groundwater depletion rate in North China was $7.1 \pm 1.0 \text{ km}^3/\text{yr}$ from 2002-2013, which is more than three times higher than the official estimate of the groundwater depletion rate in shallow plain aquifers from the GBCNP for the same period ($2.0 \text{ km}^3/\text{yr}$). The difference between our estimate and the GBCNP result indicates the potential deep groundwater depletion in the plain and piedmont regions of North China. Even if we apply the low bound of our estimate conservatively, the

study region lost approximately 70 km³ of groundwater from 2002 to 2013, which is greater than the capacity of China's Three Gorges Reservoir, the largest power station in the world.

Given the continuous groundwater depletion observed by GRACE in North China, more effective measures should be taken to curb groundwater loss, such as artificial recharge of water into aquifers [Han, 2003], crop structure adjustment [Yang and Zehnder, 2001], and reintroducing fallow periods [Kendy et al., 2004]. China's South-North Water Transfer Project, which takes water from the Yangtze River and the Han River in the south to the arid region of North China, could partially ease the water shortage in North China and also reduce the dependence on groundwater.

REGIONAL SEA LEVEL VARIATIONS FROM GRACE

4.1 Introduction

Since its launch in 2002, GRACE satellite provides direct observations of global temporal gravity variations, which includes the mass redistribution information on land and in the ocean [Chambers et al., 2004; Tapley et al., 2004; Wahr et al., 1998]. Although the annual amplitude of global mean ocean mass change observed by GRACE is only about 7 mm [Chambers and Schroter, 2011; Chambers et al., 2004; Leuliette and Willis, 2011], the spatial pattern of annual global ocean mass change from GRACE is also inhomogeneous. As shown in Figure 4.1, the annual ocean mass variation signal in the Gulf of Thailand and the Gulf of Carpentaria is significantly larger than the global mean value. Tregoning et al. [2008] found an annual periodic amplitude in sea surface height of 40 cm in the Gulf of Carpentaria using GRACE and steric-corrected altimetry. Later, Wouters and Chambers [2010] studied annual mass variations in the Gulf of Thailand, which reaches about 20 cm. In Figure 4.1, annual seawater mass change in the China seas and in the Red Sea is also significantly larger than the global mean value of 7 mm, which motivates us to further analyze the mass-induced sea level variations in these two regions. In this chapter, we discuss the sea level variations in the China seas and in the Red sea on seasonal and interannual timescales using altimetry, GRACE and oceanographic observations. In this study, the China seas includes the South China Sea (SCS), the East China Sea (ECS) and the Yellow Sea (YS). As for the Red Sea, it is an interesting study area because

of its semi-enclosed nature and arid continental surroundings.

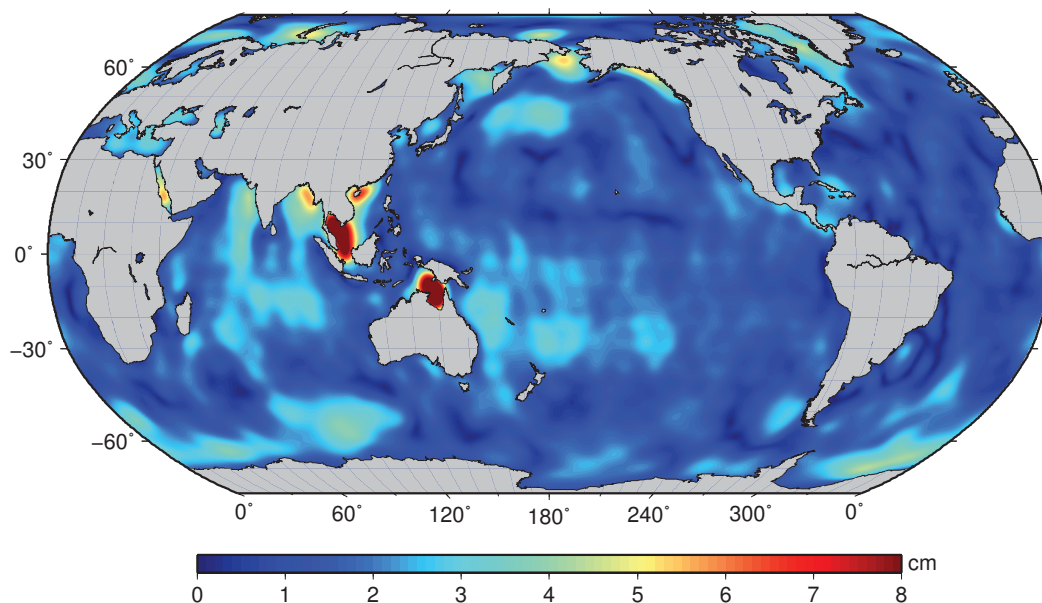


Figure 4.1: Spatial pattern of annual global ocean mass change observed by GRACE from 2003 to 2012.

4.2 Sea Level Variations in China Seas

4.2.1 Data

Satellite Altimetry

We use the merged Maps of Sea Level Anomalies (MSLA) derived from TOPEX/Poseidon, Jason-1/2, ERS-1/2 and Envisat, which are provided by the Archiving, Validation and Interpretation of Satellite Oceanographic (AVISO) data (for details, see the AVISO User Handbook available at <http://www.aviso.oceanobs.com/>). Here we use the $0.25^\circ \times 0.25^\circ$ gridded products with a daily temporal resolution. Monthly-averaged maps are calculated for comparing with other oceanographic observations. All standard geophysical and environmental corrections have been applied, including the ionospheric correction, dry and wet tropospheric corrections, solid Earth and ocean tides, ocean tide loading, pole tide, electromagnetic bias, inverted barometer corrections and instrumental corrections [Ducet et al., 2000; Minster et al., 1999]

Ishii Oceanographic Dataset

The Ishii oceanographic dataset is a historical objective analysis of oceanic temperature and salinity database, which is carried out on a monthly basis from 1945 to 2012. The Ishii analysis oceanographic dataset is based on the World Ocean Database (WOD) from National Oceanographic Data Center of the National Ocean and Atmosphere Administrations in US (NODC/NOAA), GTSP (Global Temperature Salinity Profile Program), and Argo floats data from Global Data Assembly Center (GDAC). The horizontal resolution of the Ishii dataset is $1^\circ \times 1^\circ$, ranging from 0.5°E - 359.5°E in longitude and from 89.5°S - 89.5°N in latitude. The dataset contains 24 layers from 0-1500 m. The depths of first 12 layers are 0, 10, 20, 30, 50, 75, 100, 125, 150, 200, 250, and 300 m respectively. From 300 to 1500 m, the depth interval is 100 m. In this study, we used the latest v6.13 version of Ishii dataset (<https://amaterasu.ees.hokudai.ac.jp/~ism/pub/ProjD/>).

NODC Oceanographic Dataset

NODC/NOAA provides temperature and salinity products for depths 0-700 m with pentadal, yearly, and 3-monthly temporal resolution. For years 2005 to present, yearly and 3-monthly temperature and salinity products are available for depths 0-2000 m. In this study, we adopt temperature and salinity fields for depths 0-2000 m from NODC/NOAA with 3-monthly resolution. The horizontal resolution of NODC dataset is $1^\circ \times 1^\circ$. Steric sea level variations calculated from NODC 3-monthly dataset is compared with that from Ishii dataset. More details can be available at <http://www.nodc.noaa.gov/OC5/indprod.html>.

ECCO Ocean Model

The ECCO model (Estimation of the Circulation and Climate of the Ocean) is a state-of-the-art ocean general circulation, which is based on the Massachusetts Institute of Technology general circulation model (<http://ecco.jpl.nasa.gov/>). The model is configured in a near-global domain (0.5°E - 359.5°E , 72.5°S - 72.5°N) with a uniform zonal grid spacing of 1° longitude. The meridional grid spacing is 0.3° latitude within 10° of the Equator and increases to 1° in the

extratropics. The model contains 46 levels in the vertical with 10 m spacing from the surface to 150 m, and gradually increasing to 400 m spacing at depth. The outputs of the ECCO model includes Sea Surface Height (SSH), Ocean Bottom Pressure (OBP), temperature and salinity, and so on. In this study, we use temperature and salinity data from the kf080 version ECCO model to compute the steric sea level variations over the SCS. In this version ECCO model, sea level variations from altimetry are assimilated into the model using a Kalman filter [Fukumori, 2002].

GRACE Data

We use monthly Release-05 GRACE products from the Center for Space Research (CSR) at the University of Texas at Austin [Bettadpur, 2007], which are expressed in the form of spherical harmonic (SH) geopotential coefficients up to degree and order (d/o) 60. We adopt the destriping filter proposed by Chambers and Bonin [2012] and a 300 km Gaussian smoothing to reduce the stripes in CSR solutions. In spatial domain, the leakage from mass variations on the land is removed based on the method proposed by Wahr et al. [1998]. The GRACE data are further corrected for glacial isostatic adjustment (GIA) based on the model of Paulson et al. [2007], which was updated by A et al. [2013]. To estimate the seawater mass changes in the China seas, the atmospheric and ocean de-aliasing model, which have been modeled and removed, are added back to GRACE solutions. In order to make GRACE-derived ocean mass changes comparable with inverse-barometer corrected altimetry data, we further remove the time-variable mass of the atmosphere averaged over the global ocean [Leuliette and Miller, 2009; Willis et al., 2008].

Sea Level Report of China

We adopt yearly sea level variations in the SCS, ECS and YS from the annual Sea Level Report of China released by the State Oceanic Administration of China (available at <http://www.coi.gov.cn/gongbao/haipingmian/>). These data are based on the tide gauge measurements in the coast of China.

4.2.2 Study Region

In our study, if not mentioned specifically, time series of SLV in the SCS represents the sea level change in the region of SCS deeper than 200 m (shown in Figure 4.2 as red boundary). In addition, we define two regions of SCS, i.e., eastern part of SCS (ESCS, 115°E - 120°E , 15°N - 20°N) in the west of Luzon Island and northern part of SCS (NSCS, 105°E - 115°E , 15°N - 22°N) near the coast. NSCS includes the shallow water region of northern SCS. Selected study regions in the Yellow Sea and the East China Sea are defined as the following regions, 119°E - 126°E 33°N - 37°N and 120°E - 127°E 26°N - 33°N .

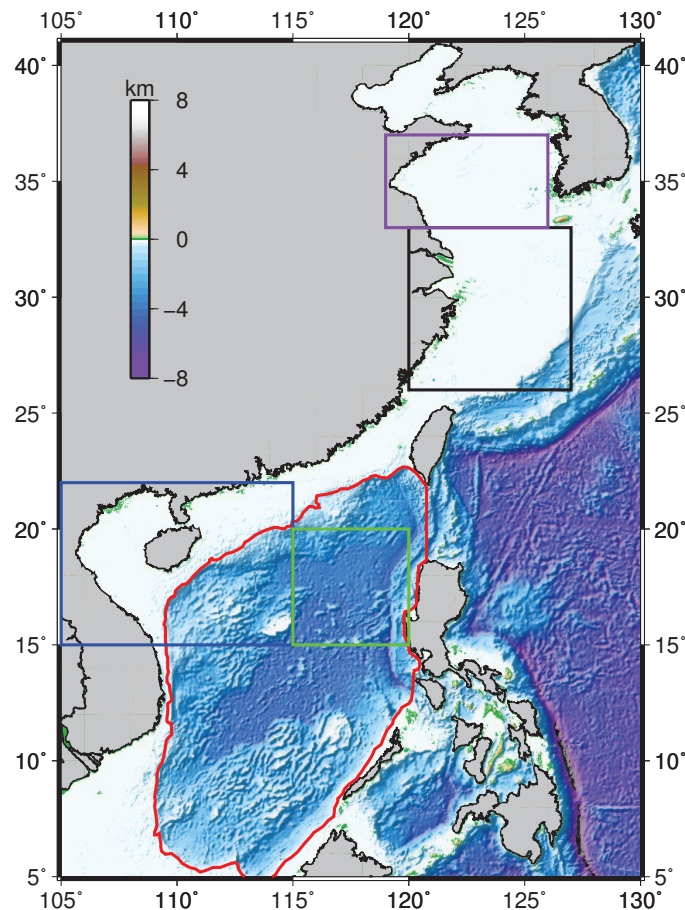


Figure 4.2: Selected study regions for the South China Sea (red boundary), eastern part of SCS (green rectangle), northern part of SCS (blue rectangle), Yellow Sea (purple rectangle) and East China Sea (black rectangle).

4.2.3 Spatial Patterns of Seasonal Sea Level Variations in China Seas

In order to make the altimetry results, steric SLV results and GRACE results comparable in spatial domain, we convert altimetry and steric SLV grids to spherical harmonic coefficients and truncate them to d/o 60. A 300 km Gaussian filter is also applied to the SH coefficients of observed SLV from altimetry and steric SLV from Ishii. As shown in Figure 4.3a, altimetry observes strong annual SLV in the Yellow Sea (YS) and the East China Sea (ECS), which peak maximum in September. In addition, significant annual variations of sea level are detected by altimetry in the eastern part and northern part of South China Sea. In Figure 4.3b, the steric SLV based on temperature and salinity data from the Ishii dataset also show the similar annual variations in the YS, ECS, and eastern part of South China Sea (ESCS). The annual phase of steric SLV from Ishii also agrees well with that from altimetry in the same region. As shown in Figure 4.3 c-d, steric-corrected altimetry results indicate that significant seasonal ocean mass change exists in the northern part of South China Sea (NSCS), which is further confirmed by GRACE. The annual amplitude of largest mass-induced SLV observed by steric-corrected altimetry and GRACE is about 6 mm in the northern coastal part of South China Sea.

We further calculated the spatial patterns of correlation coefficients between total altimetric SLV vs. steric SLV from Ishii, total altimetric SLV vs. mass-induced SLV from GRACE, and total altimetric SLV vs. SLV from Ishii+GRACE. As shown in Figure 4.4, results from altimetry agree with Ishii-based steric SLV better in the YS, ECS, and ESCS. Mass-induced SLV from GRACE show high correlations with that from altimetry in the coastal region of the South China Sea and the YS, where high annual ocean mass change is detected by GRACE and steric-corrected altimetry. The correlation coefficients between altimetry and “Ishii+GRACE” show high values in most parts of China seas, except in the western of SCS with latitudes from 10°N - 15°N . The possible reason of this low-value region will be discussed in the Discussion and Summary section.

Then, we computed the seasonal maps of SLV from altimetry, Ishii, GRACE, and “Ishii+GRACE”. As shown in Figure 4.5a, SLV in the YS, ECS, and ESCS observed by altimetry reach minimum in winter, and maximum in summer. These features are confirmed by the steric SLV from

Ishii. In addition, the Ishii-based steric SLV also show a significant dipole mode in the open ocean region of Western Pacific Ocean. GRACE observes large ocean mass loss in spring and ocean mass gain in autumn in the NSCS, which is confirmed by altimetry results. The seasonal spatial patterns of SLV from “Ishii+GRACE” agree well with those from altimetry.

Based on the above results, we conclude that seasonal SLV in the YS and ECS observed by altimetry are mainly induced by the steric SLV, i.e., density change due to the expansion/contraction of seawater. In the ESCS, seasonal SLV are also caused by the steric effect. However, in the NSCS, ocean mass change dominates the total SLV observed by altimetry.

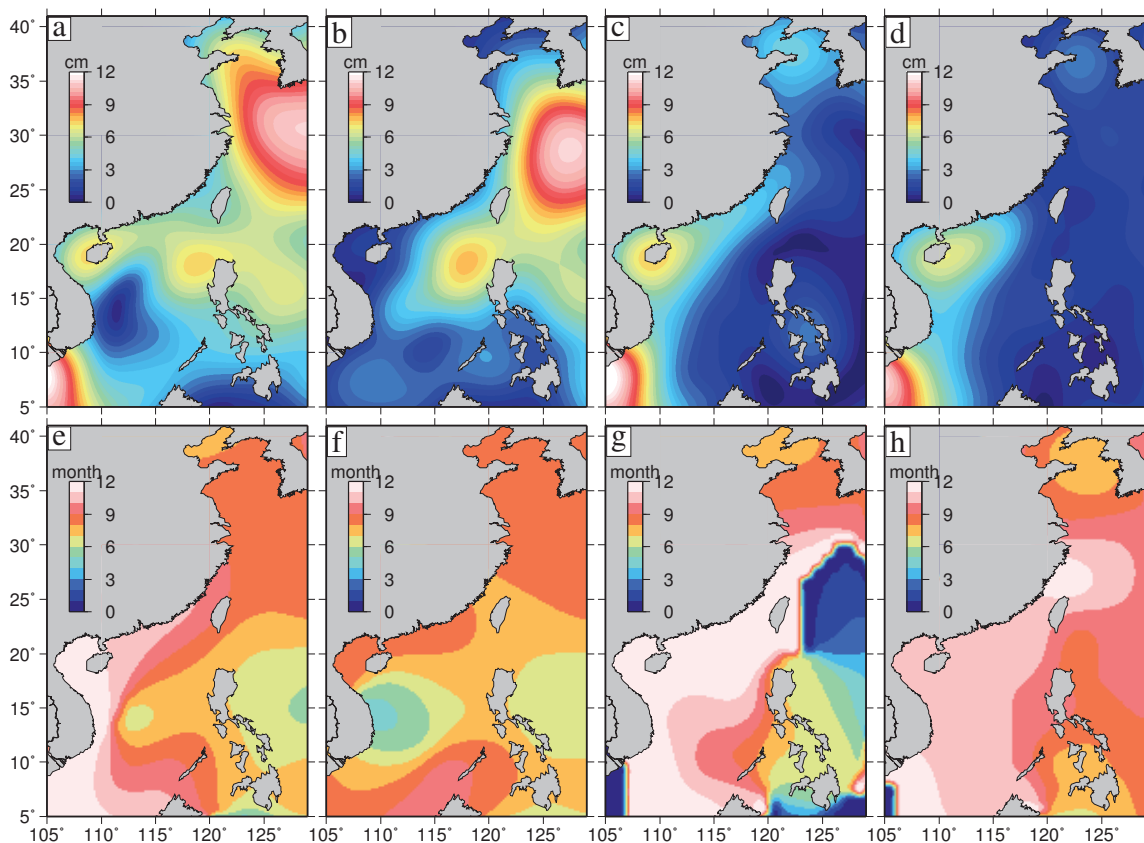


Figure 4.3: Annual amplitude of (a) total SLV from altimetry, (b) steric SLV from Ishii, (c) mass-induced SLV from steric-corrected altimetry, and (d) mass-induced SLV from GRACE in the China seas during 2003-2012. (e-h): Same as (a-d), but for annual phase.

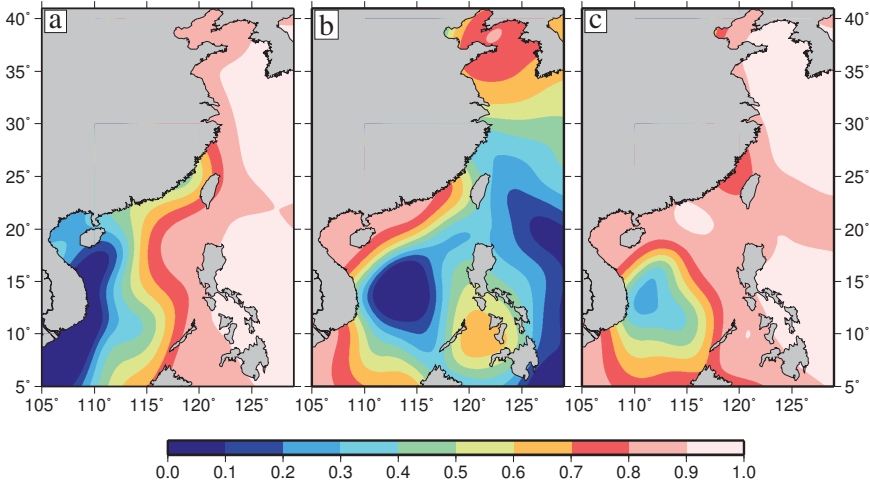


Figure 4.4: Spatial patterns of correlation coefficients between (a) total SLV from altimetry vs. steric SLV from Ishii, (b) total SLV from altimetry vs. mass-induced SLV from GRACE, and (c) total SLV from altimetry vs. SLV from “Ishii+GRACE” during 2003-2012.

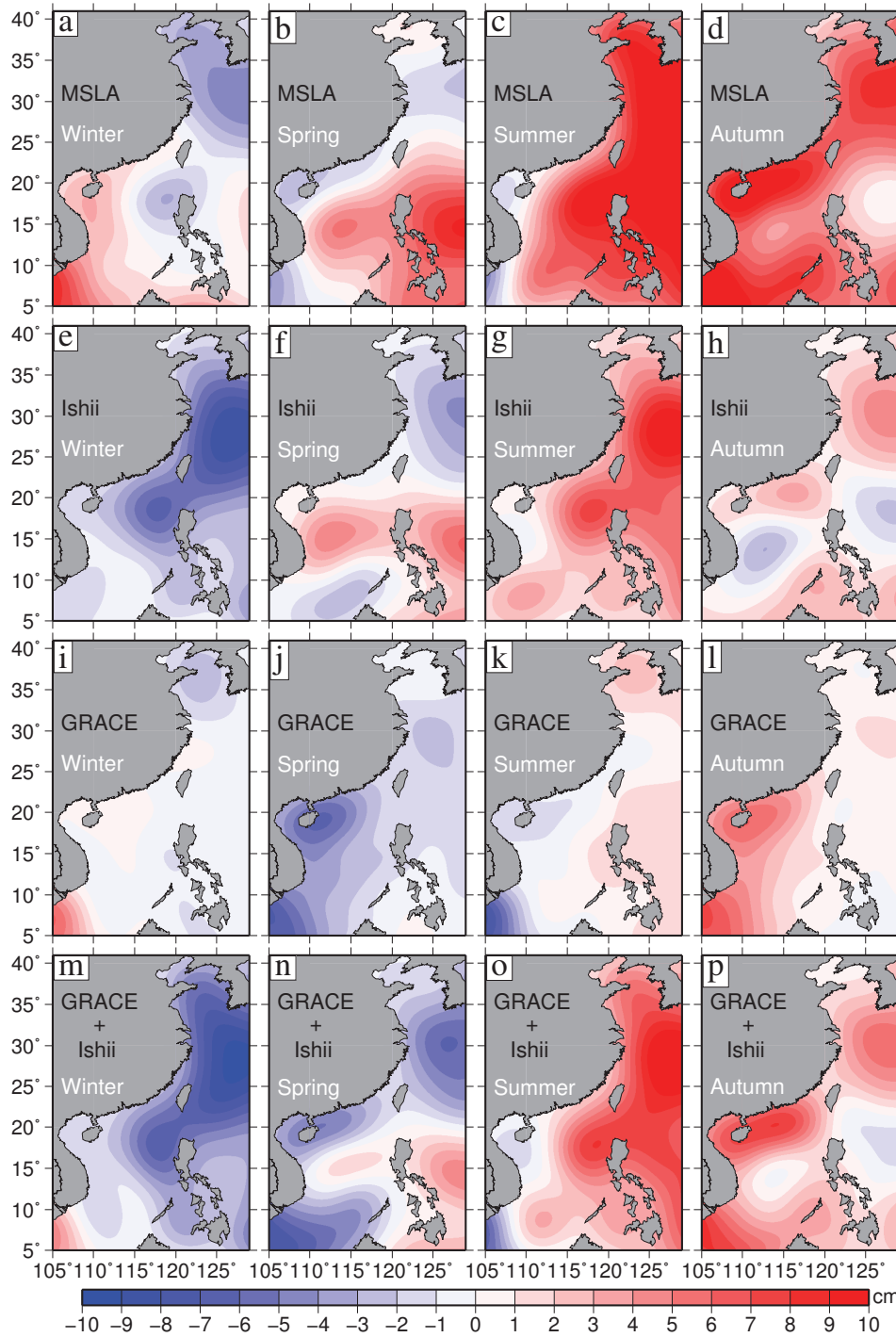


Figure 4.5: Spatial patterns of seasonal maps of SLV in China seas in winter (January-March), spring (April-June), summer (July-September), and autumn (October-December) from altimetry, Ishii, GRACE, and “Ishii+GRACE” during 2003-2012.

4.2.4 Sea Level Variations in the South China Sea

Seasonal SLV in the SCS

As shown in Figure 4.6, total SLV from altimetry, steric SLV from Ishii, and mass-induced SLV from GRACE show strong seasonal variations in the SCS. As shown in Table 4.1, the annual amplitude of total SLV in the SCS is 3.3 ± 0.4 cm, which peaks in mid-September. The steric SLV in the SCS has a similar amplitude as total SLV, but peaks about one month earlier. Altimetric SLV and steric SLV in the SCS also show the similar interannual fluctuations in Figure 4.6a. Figure 4.6b illustrates the time series of steric SLV, thermosteric SLV, and halosteric SLV from Ishii in the SCS. As shown in the figure, thermosteric SLV dominates the total steric SLV in the SCS. The annual amplitude of mass-induced SLV in the SCS observed by GRACE is 2.8 ± 0.3 cm, which agrees with the estimate from steric-corrected altimetry.

As shown in Figure 4.7b, the magnitude of seasonal steric SLV in the NSCS is significantly smaller than that in the SCS. However, the annual amplitude of mass-induced SLV in the NSCS from GRACE reaches 5.0 ± 0.4 cm, which is more than twice higher than that of the Ishii-based steric SLV (Table 4.2). In addition, the annual phase of mass-induced SLV in the NSCS agrees well with that of total SLV from altimetry, which reach maximum in November. As shown in Figure 4.7c, there is a rather good agreement between GRACE and steric-corrected altimetry on seasonal timescales in the NSCS. Different from that in the NSCS, the seasonal variability of ocean mass change in the ESCS is small (Figure 4.8c). In contrast, annual amplitude of steric SLV in the ESCS is three times higher than that of mass-induced SLV. The seasonal variability of steric SLV in the ESCS is also larger than that in the NSCS and that over the whole SCS. Based on the above results, we find that, the mass-induced SLV is dominant in northern coastal regions of SCS, whereas the steric SLV has more contribution to the total SLV in the deep basin of SCS. Over the whole SCS, both steric SLV and mass-induced SLV contribute to the total SLV on seasonal timescales. Based on these three independent observations, i.e., altimetry, oceanographic measurements, and GRACE, we successfully isolated seasonal steric and eustatic components of observed SLV in the SCS.

Apart from the seasonal variability, one of the most striking features in Figure 4.6c is the

difference in trend between the mass-induced SLV from GRACE and steric-corrected altimetry over 2003-2012 which, according to Figure 4.7c and 4.8c, comes mostly from the ESCS. This point will be addressed in detail in the next section.

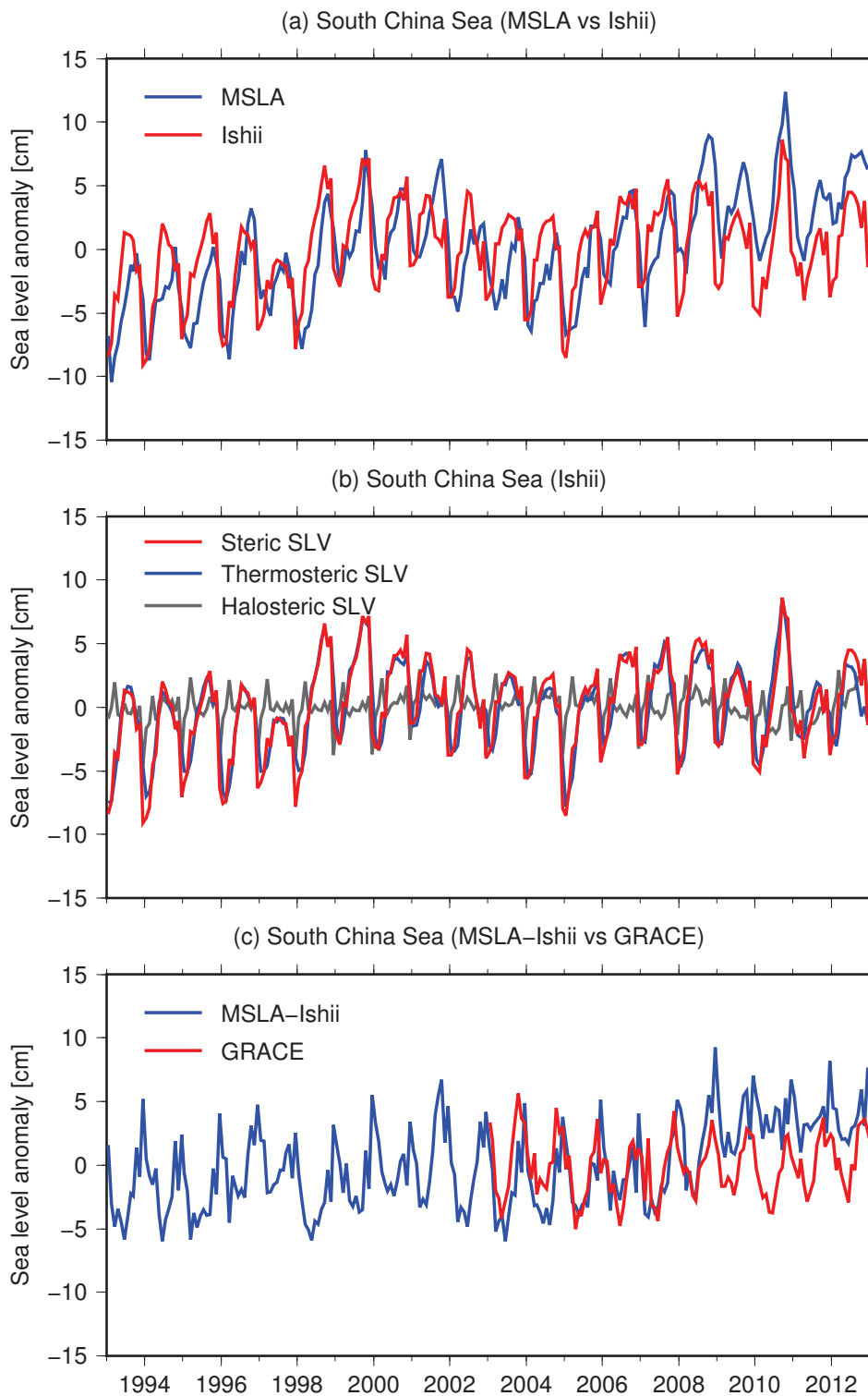


Figure 4.6: Time series of (a) total SLV from altimetry and steric SLV from Ishii, (b) steric, thermosteric, and halosteric SLV from Ishii, (c) mass-induced SLV from GRACE and steric-corrected altimetry in the SCS during 1993-2012.

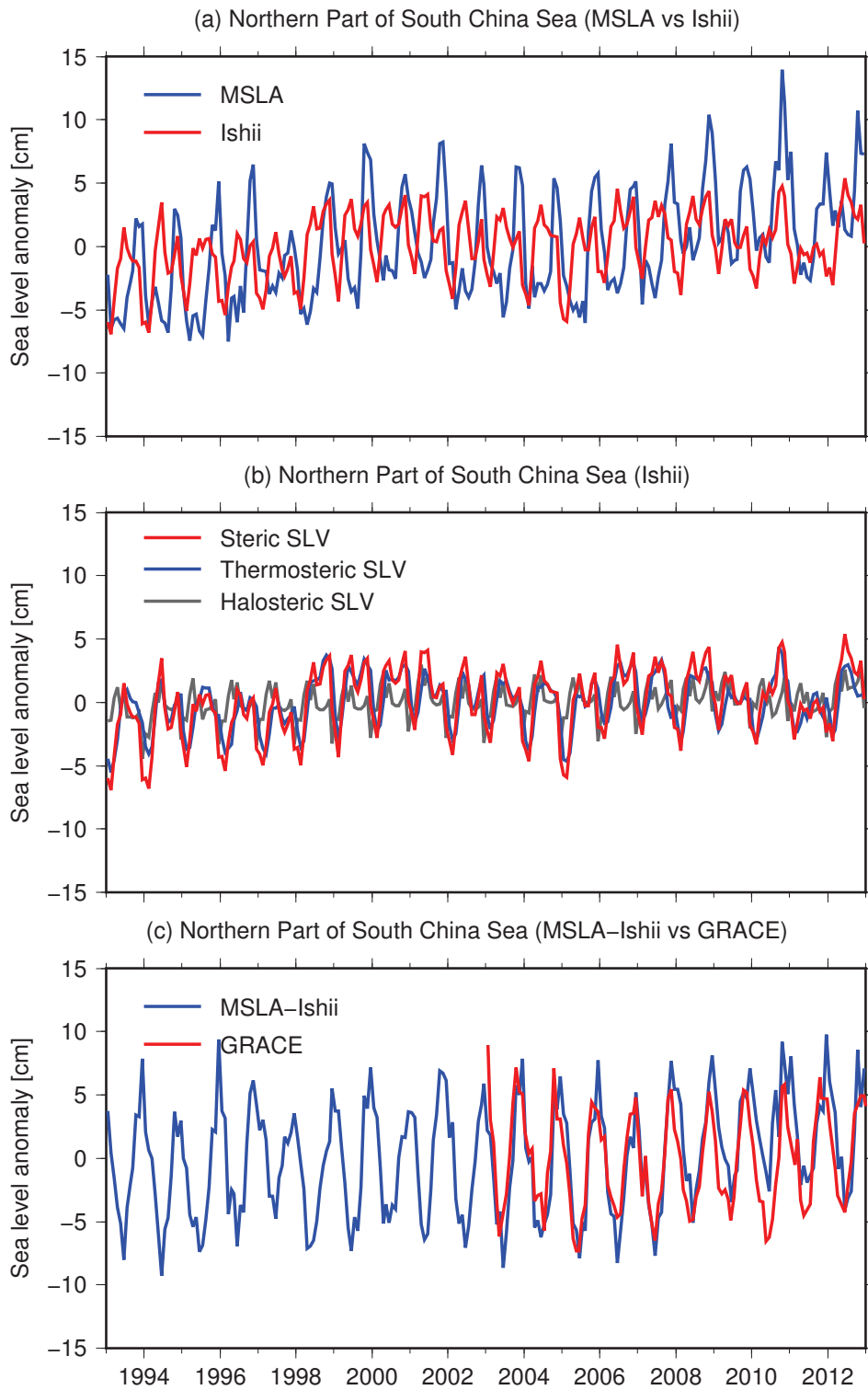


Figure 4.7: Same as Figure 4.6, but for the NSCS.

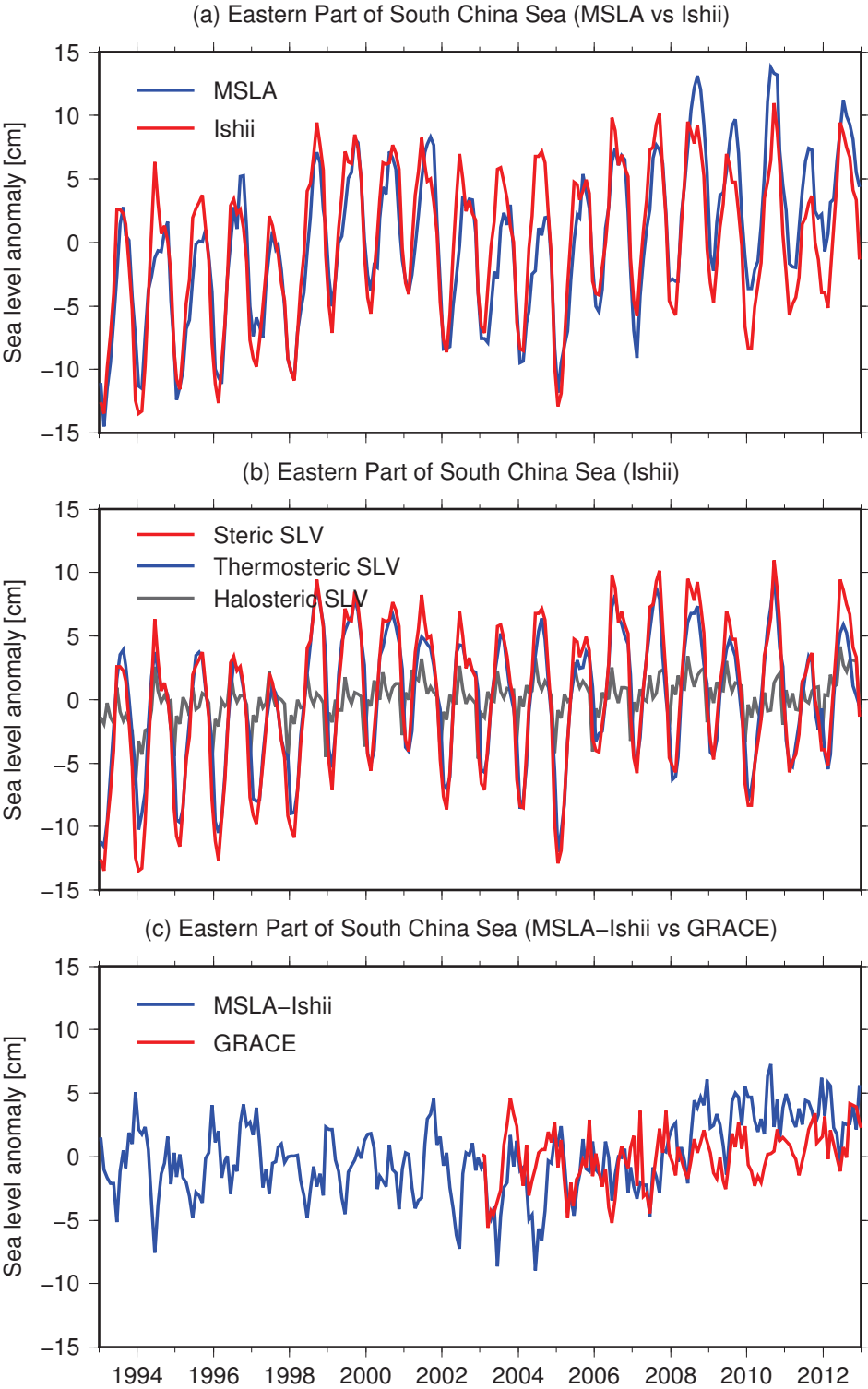


Figure 4.8: Same as Figure 4.6, but for the ESCS.

Table 4.1: Annual amplitudes (cm) and phases ($^{\circ}$) of total SLV from altimetry, steric SLV, thermosteric SLV, and halosteric SLV from Ishii in the SCS, NSCS, and ESCS during 1993-2012.

	SCS	NSCS	ESCS
	Amplitude (Phase)	Amplitude (Phase)	Amplitude (Phase)
MSLA (altimetry)	3.3 ± 0.4 (258 ± 7)	4.1 ± 0.4 (315 ± 1)	6.1 ± 0.5 (232 ± 5)
Steric SLV (Ishii)	3.5 ± 0.4 (214 ± 7)	2.2 ± 0.3 (204 ± 7)	6.8 ± 0.5 (217 ± 4)
Thermosteric SLV (Ishii)	3.3 ± 0.3 (221 ± 5)	1.8 ± 0.2 (230 ± 8)	5.7 ± 0.4 (222 ± 3)
Halosteric SLV (Ishii)	0.4 ± 0.2 (148 ± 29)	1.0 ± 0.2 (149 ± 10)	1.2 ± 0.2 (190 ± 11)

Table 4.2: Annual amplitudes (cm) and phases ($^{\circ}$) of total SLV from altimetry, steric SLV from Ishii, mass-induced SLV from steric-corrected altimetry (“MSLA-Ishii”), and mass-induced SLV from GRACE in the SCS, NSCS, and ESCS during 2003-2012.

	SCS	NSCS	ESCS
	Amplitude (Phase)	Amplitude (Phase)	Amplitude (Phase)
MSLA (altimetry)	3.2 ± 0.5 (259 ± 9)	4.1 ± 0.5 (317 ± 3)	6.0 ± 0.6 (230 ± 7)
Steric SLV (Ishii)	3.3 ± 0.6 (216 ± 9)	2.1 ± 0.4 (208 ± 10)	6.7 ± 0.7 (217 ± 6)
MSLA-Ishii	2.4 ± 0.5 (332 ± 11)	5.2 ± 0.5 (339 ± 5)	1.6 ± 0.5 (339 ± 18)
GRACE	2.8 ± 0.3 (315 ± 1)	5.0 ± 0.4 (322 ± 5)	2.0 ± 0.4 (308 ± 12)

Interannual SLV in the SCS

As one of the largest marginal sea in the tropics, South China Sea connects the East China Sea, the Pacific Ocean and the Indian Ocean through Taiwan Strait, Luzon Strait and Malacca Strait. To investigate the main driving climate factor of interannual SLV in the SCS, we analyzed the correlation between total SLV/steric SLV and NINO4 index. NINO4 index is defined as the mean sea surface temperature over the central tropic Pacific Ocean (i.e., 160°E - 150°W , 5°N - 5°S), which is used to monitor the occurrence of the El Niño-Southern Oscillation (ENSO) events. We downloaded the NINO4 index data from http://www.esrl.noaa.gov/psd/gcos_wgsp/

Timeseries/Nino4/index.html. Figure 4.9a shows the low-pass filtered NINO4 and detrended interannual variations of altimetric sea level and steric sea level in the SCS. As shown in Figure 4.9a, altimetric SLV and steric SLV show similar interannual fluctuations in the SCS, and match the interannual variations of inverse NINO4 index well. For the inverse NINO4 index, negative anomaly represents El Niño event, while positive anomaly means La Niña event. As indicated by the NINO4 index, the El Niño event occurs in 1997/98 and 2009/2010, while the La Niña event happens in 1998/2000, 2007/08, and 2010/11. As indicated in Figure 4.9a, during the El Niño event, observed sea level and steric sea level in the SCS drop dramatically; and vice versa, when the La Niña event happens. For example, during the period of the 1997/98 El Niño and the following 1998/2000 La Niña, the sharp V-shaped sea level change is observed in the SCS. It is obvious that interannual sea level change in the SCS is modulated by ENSO. In addition, the steric SLV is the dominant component of SLV in the SCS on interannual timescales. It is worthwhile to note that, in 2011, there is a large sea level drop in the SCS. The peak-to-trough fluctuation is more than 5 cm. In fact, global mean sea level (GMSL) also dropped 5 mm between the beginning of 2010 and mid 2011, when a strong La Niña event occurred. Considering the global averaging effect, this 5 mm drop is a rather big value for GMSL. This drop in GMSL is primarily driven by an ENSO-related transfer of water mass between the oceans and the continents [Boening et al., 2012; Fasullo et al., 2013]. As shown in 4.9a, the sea level drop during the 2010/11 La Niña is amplified in the SCS.

Furthermore, we calculated the correlations between total SLV/steric SLV and NINO4 index corresponding to different lag times. Positive lag time represents the lead of NINO4 over total SLV/steric SLV. As shown in Figure 4.9, the maximum correlation coefficient between total SLV and NINO4 is 0.64, when NINO4 leading the total SLV 2 months. The correlation coefficient between steric SLV and NINO4 reaches maximum, i.e., 0.55, when there is no lag between them. Good agreement between altimetric SLV/steric SLV and NINO4 indicates that the interannual variations of sea level in the SCS is closely related to ENSO.

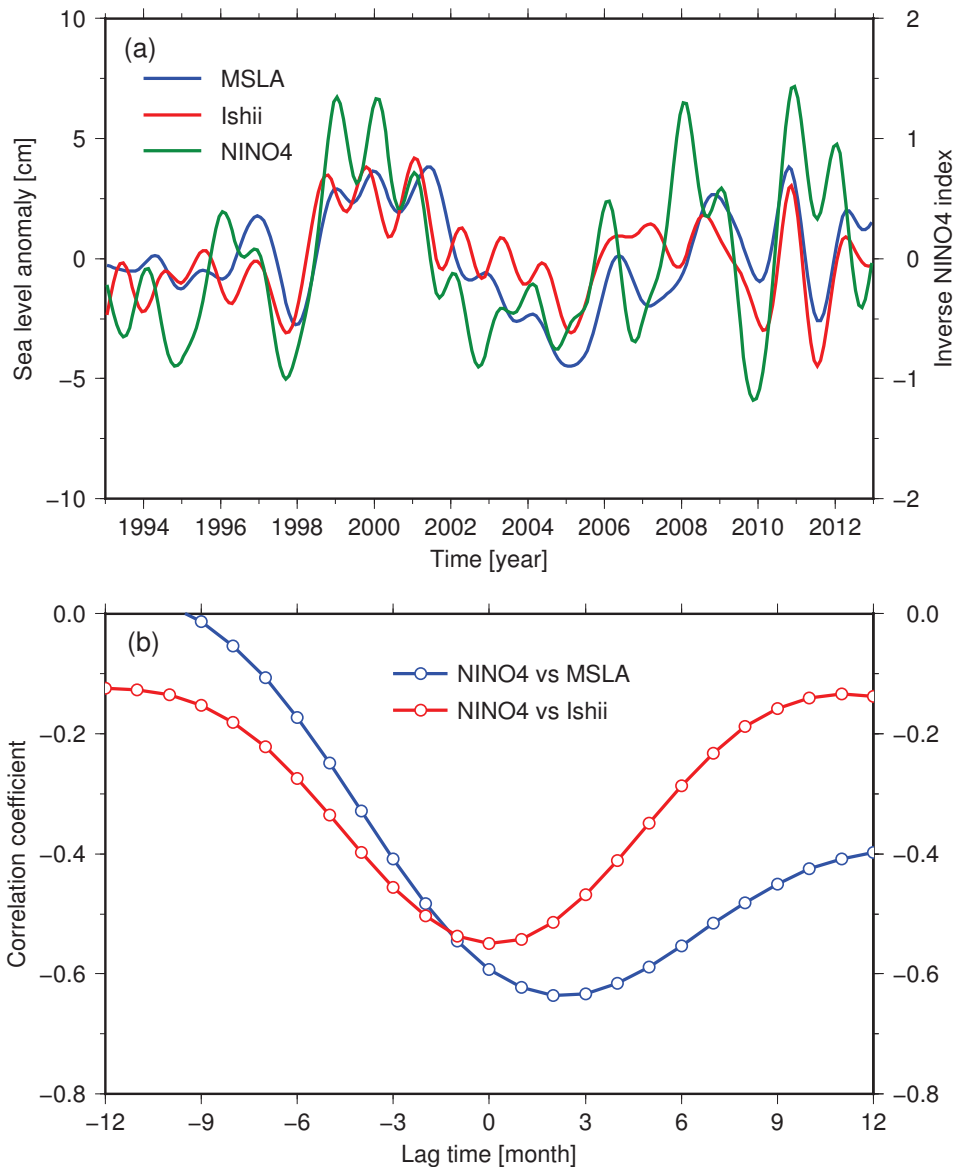


Figure 4.9: (a) Interannual time series of total SLV from altimetry and steric SLV from Ishii in the SCS during 1993-2012. Seasonal cycles and the trend are removed using least-square-fit and a one-year low-pass filter is applied. Time series of inverse NINO4 index is also superimposed. The mean value of inverse NINO4 index is removed and a one-year low-pass filter is applied. (b) Correlation coefficients corresponding to different lag times between total SLV/steric SLV and NINO4 index.

We further calculated the nonseasonal variations of sea level in the SCS, NSCS, and ESCS, i.e., only removing seasonal cycles of SLV. As shown in Figure 4.10a, the total SLV from altimetry over the whole SCS is dominant by interannual fluctuations, with strong increases over

1993-1999 and 2005-2012 and a significant decrease over 2000-2004. The rate of altimetry-observed SLV in the SCS is 8.7 ± 1.8 and -12.3 ± 1.8 mm/yr, respectively, during 1993-1999 and 2000-2004, which is fairly consistent with the estimates from Li et al. [2002] and Cheng and Qi [2007]. The mean sea level rise rate in the SCS is 4.3 ± 0.5 mm/yr over the period 1993-2012. Additionally, yearly sea level variations from the annual Sea Level Report of China also show similar large interannual oscillations as altimetry-observed SLV (Figure 4.10a). The mean sea level rise rate in the SCS based on the government report is 3.6 mm/yr from 1993-2012. Keep in mind that the yearly values reported by the State Oceanic Administration of China only represent the mean sea level variations near the coast of China, since they are based on tide gauge observations.

In Figure 4.10a, steric SLV estimated from the Ishii dataset shows similar interannual fluctuations as that from altimetry before 2008. It indicates that the steric SLV is the dominant component of total SLV in the SCS on interannual timescales. However, since 2008, the steric SLV decreases significantly, which is quite different from the altimetric SLV. This discrepancy will be discussed later.

As shown in the panel (b) and (c) of Figure 4.10, the magnitude of interannual fluctuations is dampened in the NSCS, but amplified in the ESCS. It is fairly reasonable since the steric component of interannual SLV is dominant in the SCS and the magnitude of seasonal steric SLV is large in the ESCS, but small in the NSCS. More importantly, since 2008, the discrepancy between altimetric SLV and steric SLV is also manifested in the ESCS and NSCS.

We calculated the trend maps of sea level change in the SCS over three time periods: 1993-1999, 2000-2004, and 2007-2012. As shown in Figure 4.11, both the Ishii-based steric SLV and altimetric SLV show the significant sea level rise in the central ocean basin of SCS over 1993-1999. Then, the total sea level observed by altimetry drops rapidly in the central ocean basin of SCS during 2000-2004. The Ishii-based steric SLV also captures the similar features, but with smaller magnitude, for the same time period. The large discrepancy between altimetry and Ishii appears over the period 2007-2012. Altimetry detects rapid sea level rise in the surrounding boundary regions of SCS, i.e., the shallow water region, over 2007-2012. There are two separate domes of weak sea level decrease in the central deep ocean basin of

SCS, detected by altimetry. The steric SLV from Ishii also demonstrate a small sea level drop in the central SCS over 2007-2012 (Figure 4.11f). However, more importantly, the sea level rise rate from steric SLV in the shallow water region of SCS is significantly smaller than that from altimetry. This apparent discrepancy in the shallow water region of SCS is exactly the reason for the difference between interannual time series of altimetric SLV and that of steric SLV since 2008, which are indicated in Figure 4.10.

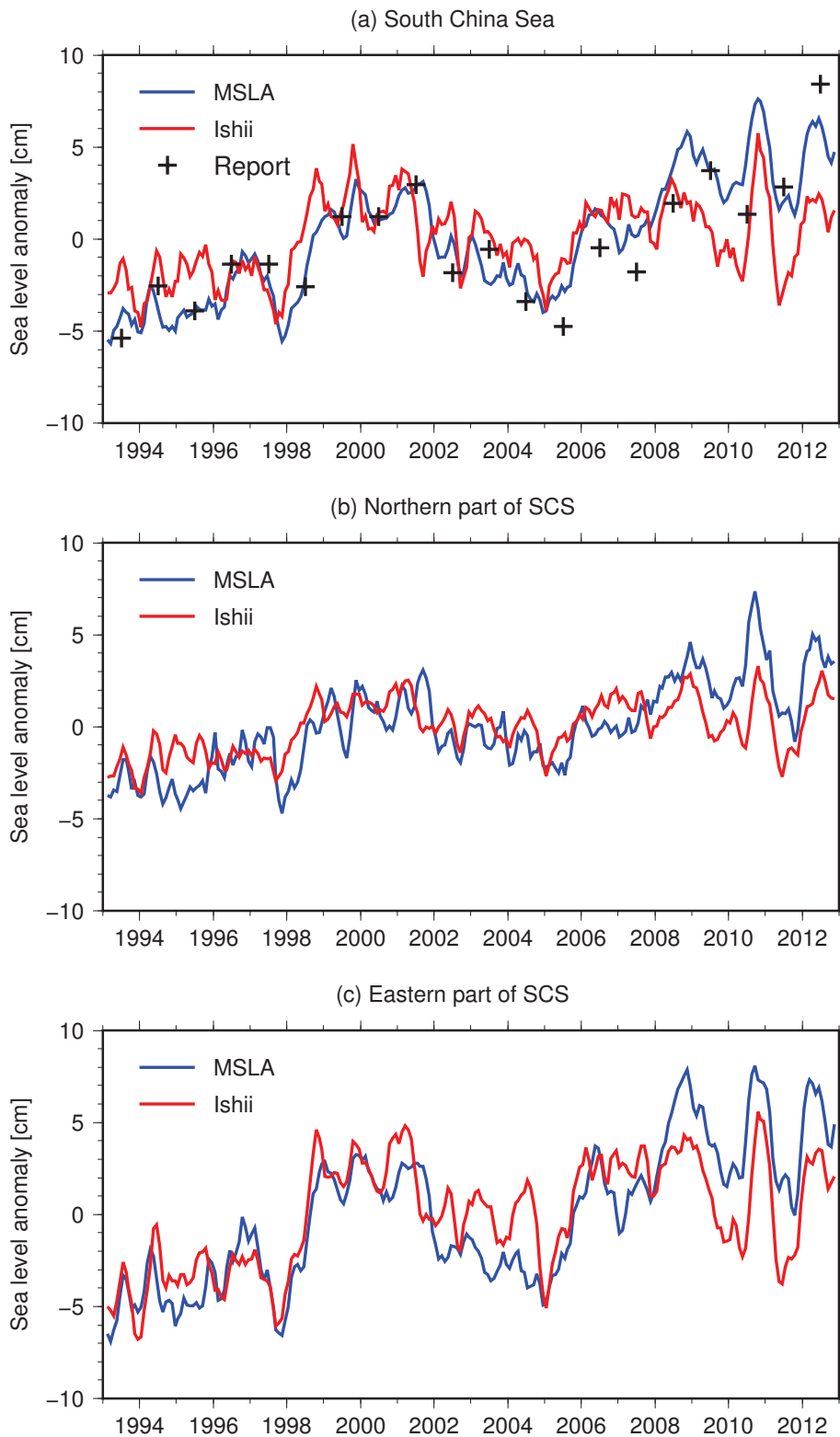


Figure 4.10: Interannual time series of total SLV from altimetry and steric SLV from Ishii in the SCS, NSCS, and ESCS during 1993-2012. Seasonal cycles are removed using least-square-fit and a 3-month moving average is applied. Yearly sea level variations in the SCS from the annual Sea Level Report of China are superimposed in panel (a).

Table 4.3: Trends of total SLV from altimetry and steric SLV from Ishii in the SCS in different time periods (mm/yr).

	1993-1999	2000-2004	2005-2007	2008-2012	1993-2012
MSLA (altimetry)	8.7 ± 1.8	-12.3 ± 2.3	13.6 ± 6.0	2.2 ± 3.4	4.3 ± 0.5
Steric SLV (Ishii)	7.4 ± 2.2	-5.9 ± 3.1	12.8 ± 7.1	-1.8 ± 4.3	1.6 ± 0.5

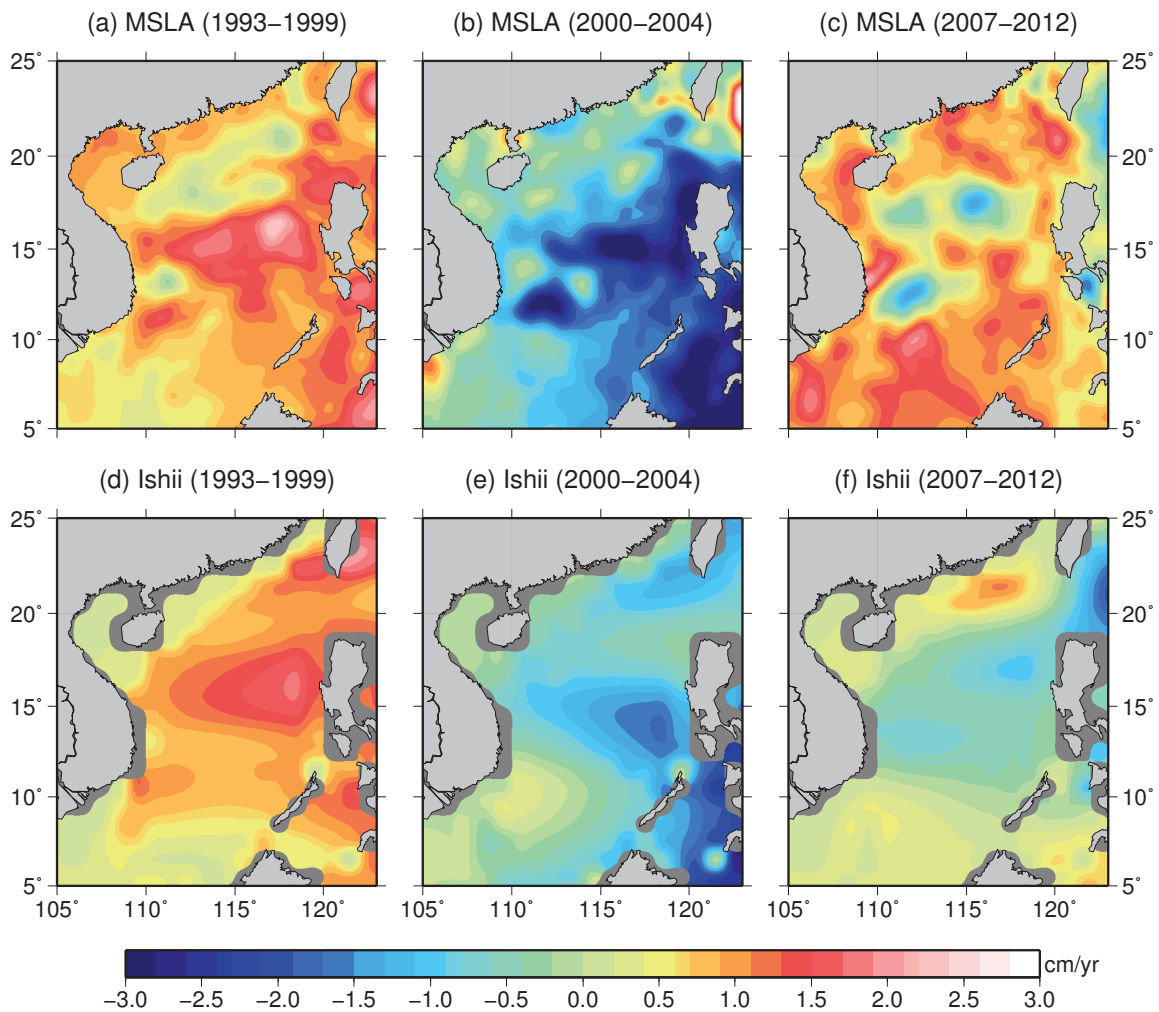


Figure 4.11: Trend maps of total SLV from altimetry and steric SLV from Ishii in the SCS over three time periods: 1993-1999, 2000-2004, and 2007-2012.

To validate our findings, we further calculated the steric SLV in the SCS, NSCS, and ESCS using the temperature and salinity observation dataset from NODC and simulation datasets from the ECCO ocean model. As shown in Figure 4.12 (a-c), the steric SLV based on NODC

oceanographic observation dataset is also obviously different from altimetric SLV since late 2007, which agrees rather well with results from Ishii. However, the steric SLV from ECCO shows fairly good agreement with altimetric SLV, although there is a slight discrepancy in last two or three years. Keep in mind that, for the ECCO model, sea level anomalies are assimilated into the model using a Kalman filter [Fukumori, 2002], which might explain the good agreement between the ECCO steric SLV and altimetric SLV. However, when another simulation version of ECCO is used with no data assimilated (kf079), the steric SLV based on this version of ECCO also agrees with altimetric SLV better than that from oceanographic observations from Ishii and NODC (shown in Figure 4.12a). For the NODC and Ishii datasets, the similar in-situ temperature and salinity observation database is adopted, but using different interpolation methods (i.e., mapping strategies). In addition, the NODC provides the temperature and salinity dataset from 0 to 2000 m every three months, while the Ishii provides the temperature and salinity dataset from 0 to 1500 m every month. However, we find that, the difference of steric SLV caused by different integrated depth is negligible (not shown).

We computed the interannual mass-induced SLV in the SCS, NSCS, and ESCS from GRACE, “MSLA-Ishii”, and “MSLA-ECCO” over the period 2003-2012. Considering the large discrepancy between altimetric SLV and Ishii steric SLV, there exists a high rate of mass-induced sea level rise estimate from “MSLA-Ishii”, i.e., 7.7 ± 1.1 mm/yr in the SCS over 2003-2012 (Figure 4.12d and Table 4.4). However, the trend of mass-induced SLV from GRACE is not significantly different from zero, i.e., 0.2 ± 0.8 mm/yr in the SCS over 2003-2012. The corresponding estimate from “MSLA-ECCO” is 1.4 ± 0.7 mm/yr, which agrees with the GRACE estimate better than that from “MSLA-Ishii”. The similar conclusions can be drawn in the NSCS and ESCS.

In spatial domain, trend map of steric SLV from ECCO matches well with that from altimetry over 2003-2012, shown in Figure 4.13. However, the Ishii-based steric SLV fails to capture the sea level increase in the whole basin of SCS. The secular seawater mass increase rate inferred from “MSLA-Ishii” is as high as 1 cm/yr in the central SCS, which is unrealistic, since both GRACE and “MSLA-ECCO” do not observe so large trend signal in the same region.

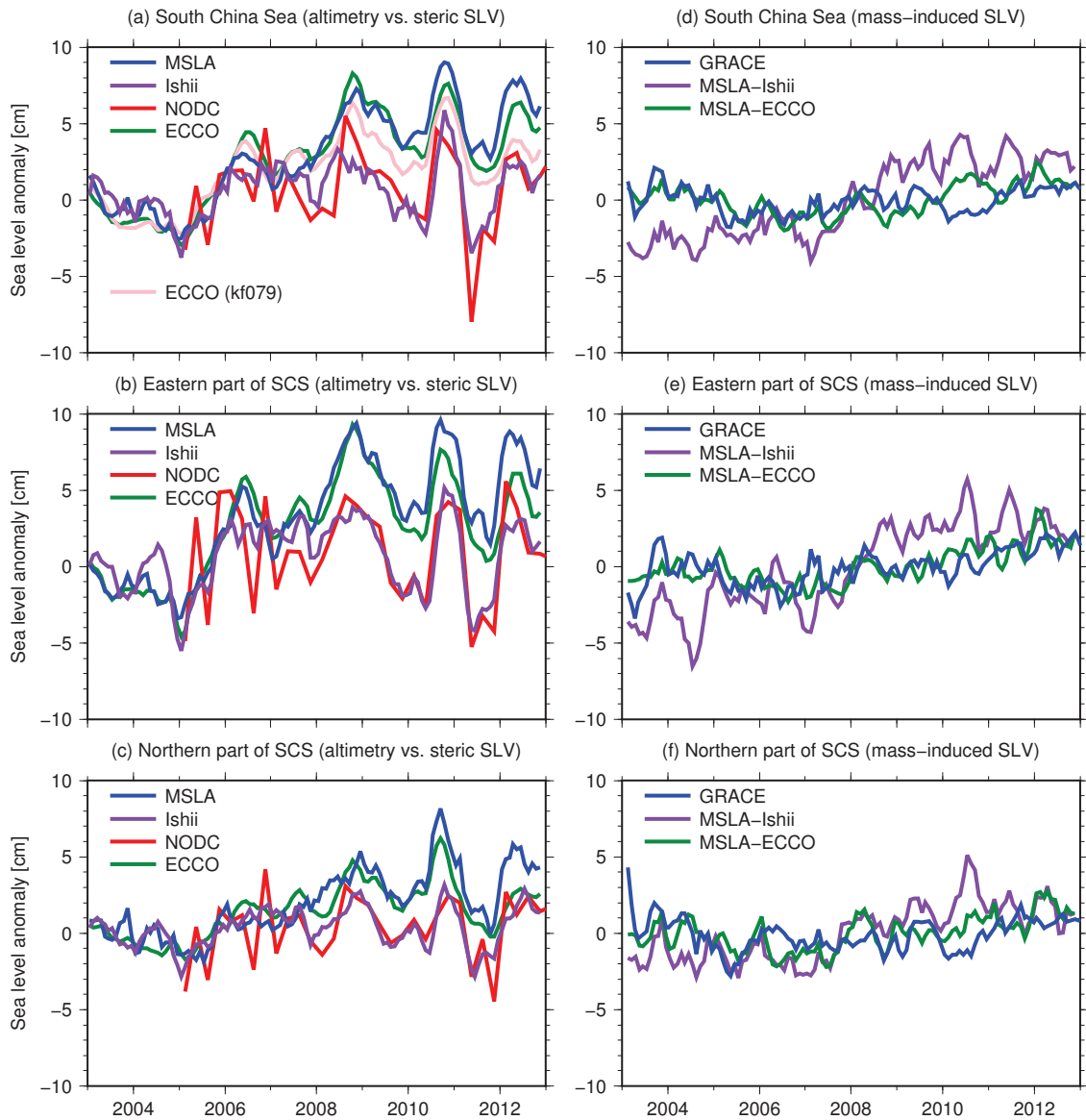


Figure 4.12: (a) Interannual time series of total SLV from altimetry and steric SLV from Ishii, NODC, and ECCO in the SCS during 2003-2012. Results from another version of ECCO model (kf079) are also shown. To be comparable, the mean value of every time series during 2003-2006 is removed. The mean value of NODC time series during 2005-2012 is set to be the same as that of Ishii time series for the same period. (b-c) Same as (a), but for the NSCS and ESCS. (d) Interannual time series of mass-induced SLV from GRACE, “MSLA-Ishii”, and “MSLA-ECCO” in the SCS during 2003-2012. (e-f) Same as (d), but for the NSCS and ESCS. Seasonal cycles are removed using least-square-fit and a 3-month moving average is applied.

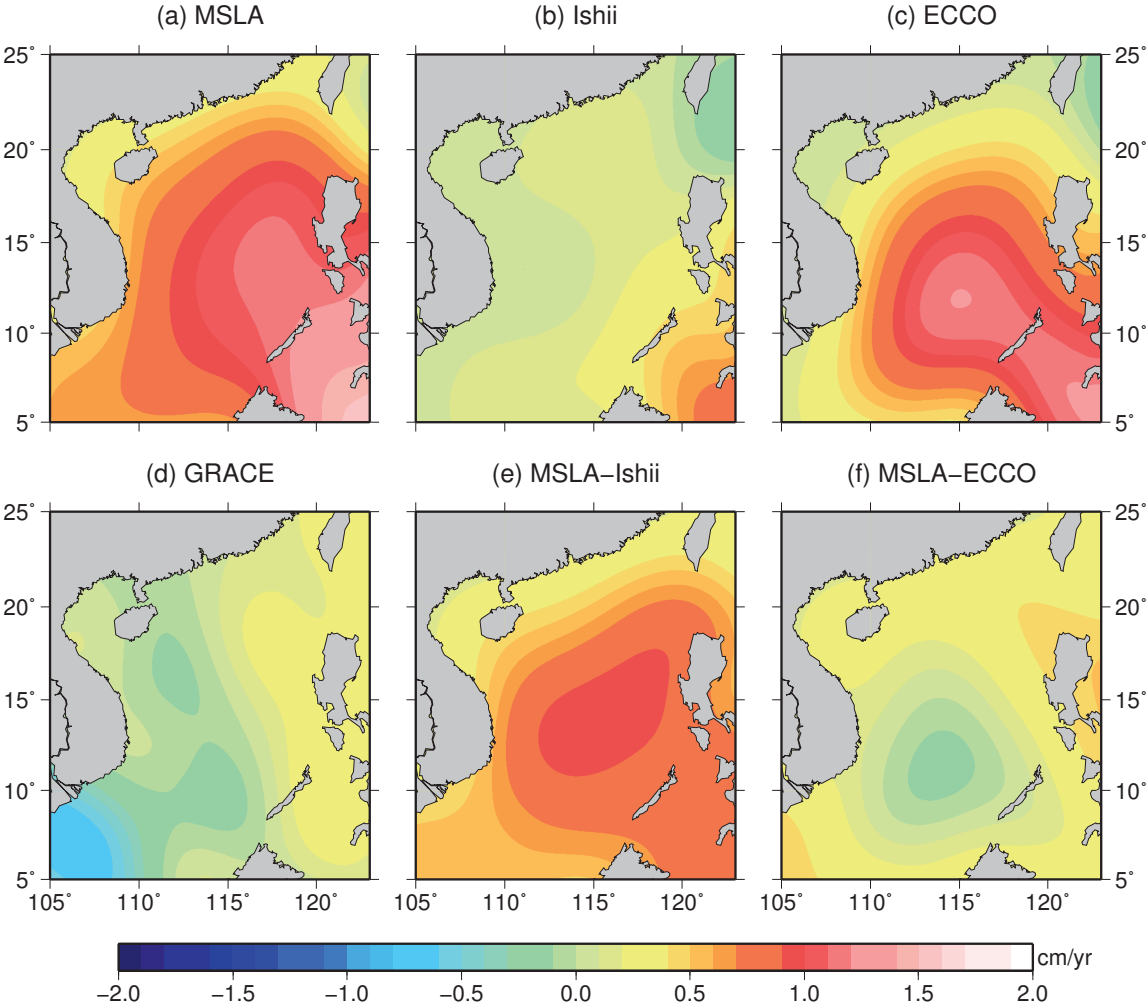


Figure 4.13: Trend maps of total SLV from altimetry, steric SLV from Ishii and ECCO, mass-induced SLV from GRACE, “MSLA-Ishii”, and “MSLA-ECCO” in the SCS during 2003-2012.

Table 4.4: Trends of total SLV from altimetry, steric SLV from Ishii and ECCO, mass-induced SLV from steric-corrected altimetry and from GRACE in the SCS, NSCS, and ESCS during 2003-2012 (mm/yr).

	SCS	NSCS	ESCS
MSLA (altimetry)	9.1±1.2	5.7±1.2	9.9±1.6
Steric SLV (Ishii)	1.4±1.4	0.9±0.9	1.4±1.6
Steric SLV (ECCO)	7.7±1.3	3.8±0.9	7.0±1.7
Mass-induced SLV (MSLA-Ishii)	7.7±1.1	4.8±1.2	8.4±1.2
Mass-induced SLV (MSLA-ECCO)	1.4±0.7	1.9±0.9	2.9±0.8
Mass-induced SLV (GRACE)	0.2±0.8	-0.2±1.0	2.1±1.0

4.2.5 Sea Level Variations in the East China Sea and Yellow Sea

As shown in Figure 4.14a and Figure 4.15a, SLV in the ECS and YS from altimetry demonstrate a similar large seasonal variability, with an annual amplitude of about 8 cm and peaking in September. The annual amplitude of steric SLV in the ECS is 7.5 ± 0.2 cm, which is consistent with that of total SLV from altimetry. However, the annual amplitude of steric SLV in the YS is only 4.6 ± 0.1 cm. Nevertheless, the thermosteric SLV is the dominant component of steric SLV in the YS, which is also the case of ECS (Figure 4.14b and Figure 4.15b).

In Figure 4.14c, mass-induced sea level estimated from steric-corrected altimetry (“MSLA-Ishii”) mainly show high-frequency variations in the ECS. GRACE-observed seawater mass change in the ECS also demonstrates similar high-frequency variations. The standard deviation of mass-induced SLV in the ECS estimated from “MSLA-Ishii” is 2.4 cm, the same as that from GRACE. The root-mean-square (RMS) of differences between mass-induced SLV from “MSLA-Ishii” and GRACE is 2.2 cm, which does not decrease significantly. However, there is a high correlation coefficient between them in the ECS (i.e., 0.62). As shown in Figure 4.15c, mass-induced SLV from “MSLA-Ishii” shows a good agreement with that from GRACE in the YS. The correlation coefficient between them reaches as high as 0.78. The standard deviation of mass-induced SLV in the YS estimated from “MSLA-Ishii” and from

GRACE is 3.4 cm and 2.9 cm, respectively. The RMS of differences between mass-induced SLV from “MSLA-Ishii” and GRACE in the YS decreases to 2.2 cm.

As shown in Figure 4.16, on interannual timescales, SLV in the ECS and YS estimated from altimetry show similar features. Sea level anomaly reaches minimum in 1995, which is 5 cm lower than the mean sea level. From 1995 to 1998, a rapid sea level rise is detected in the ECS and YS. The sea level rise rate in the ECS and YS is 12.8 ± 4.9 mm/yr and 12.8 ± 6.8 mm/yr respectively over the period 1995-1998. Since 1999, the mean sea level in the ECS and YS is rather stable, except a significant increase during 2011-2012. On interannual timescales, the change of steric SLV in the YS is negligible, while steric SLV in the ECS shows some fluctuations. However, no significant rate of steric SLV exists in the ECS and YS. The mean sea level rise rate in the ECS and YS observed by altimetry is 2.2 ± 0.5 mm/yr and 1.8 ± 0.6 mm/yr, respectively, during 1993-2012, which is lower than the global mean sea level rise rate for the same time period (i.e., 3.2 mm/yr) [Boening et al., 2012; Meyssignac and Cazenave, 2012].

In Figure 4.16, yearly sea level variations released by the annual Sea Level Report of China from State Oceanic Administration (SOA) of China also show the sea level drop in 1995 and a rapid sea level increase from 1995 to 1998, which confirm our findings from altimetry. Sea level from the government report also shows a large positive anomaly in 2012, which agrees well with our altimetric SLV. Keep in mind that sea level variations from the government report are based on the coastal tide gauge measurements, while our altimetric SLV represent the mean sea level change averaged in a specific ocean region. The mean sea level rise rate in the ECS and YS based on the government report is 2.6 and 3.4 mm/yr respectively from 1993-2012.

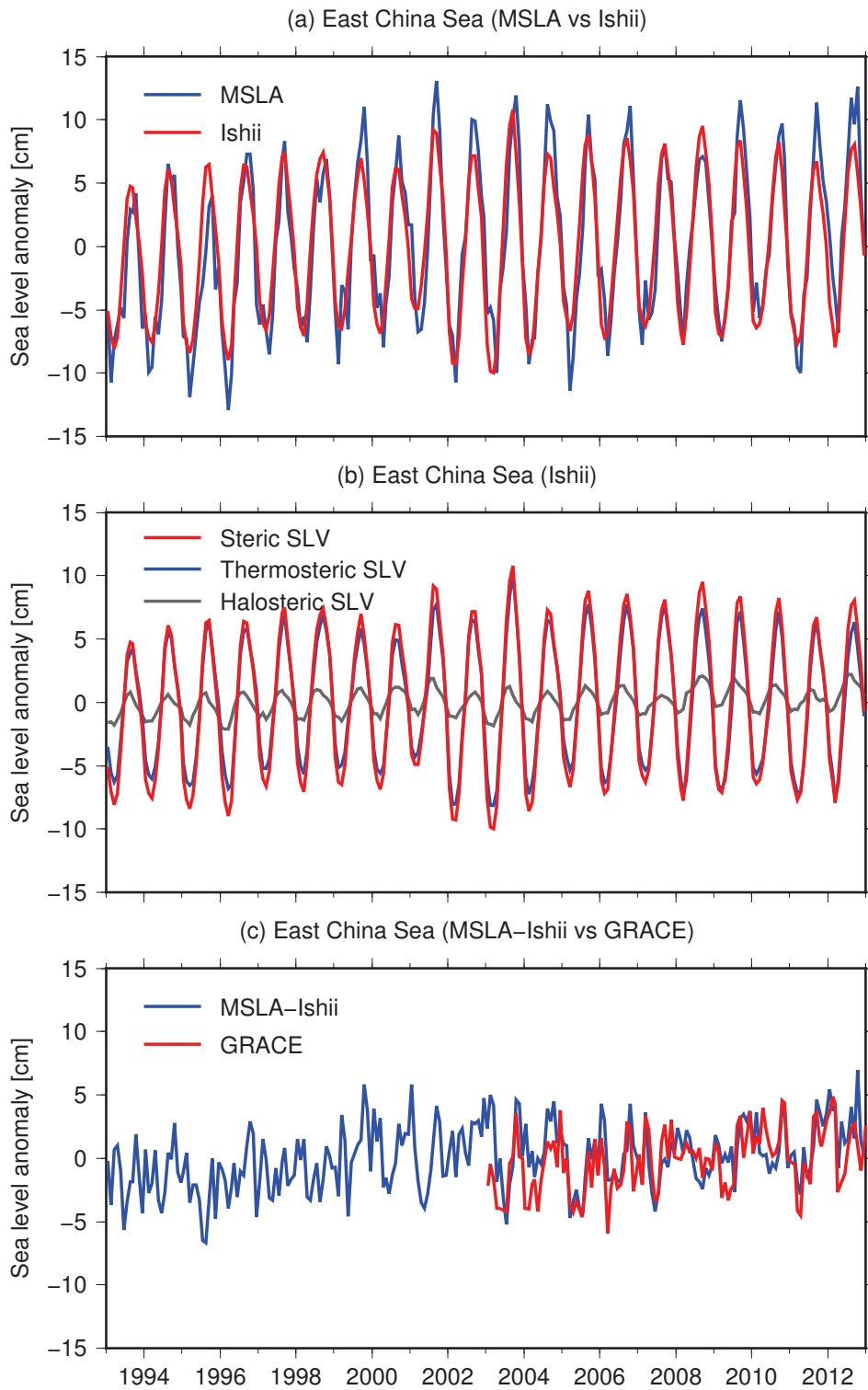


Figure 4.14: Same as Figure 4.6, but for the ECS.

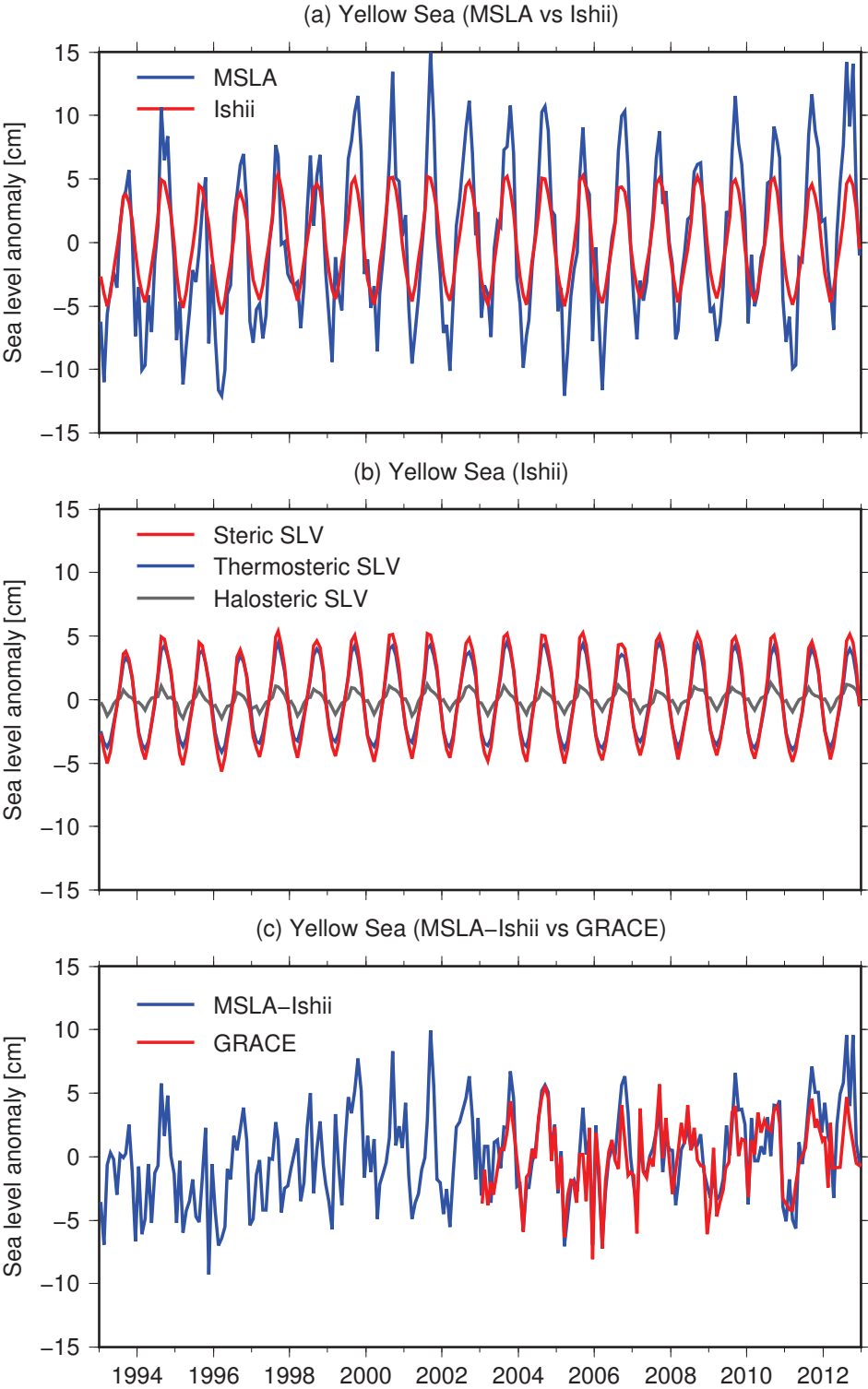


Figure 4.15: Same as Figure 4.6, but for the YS.

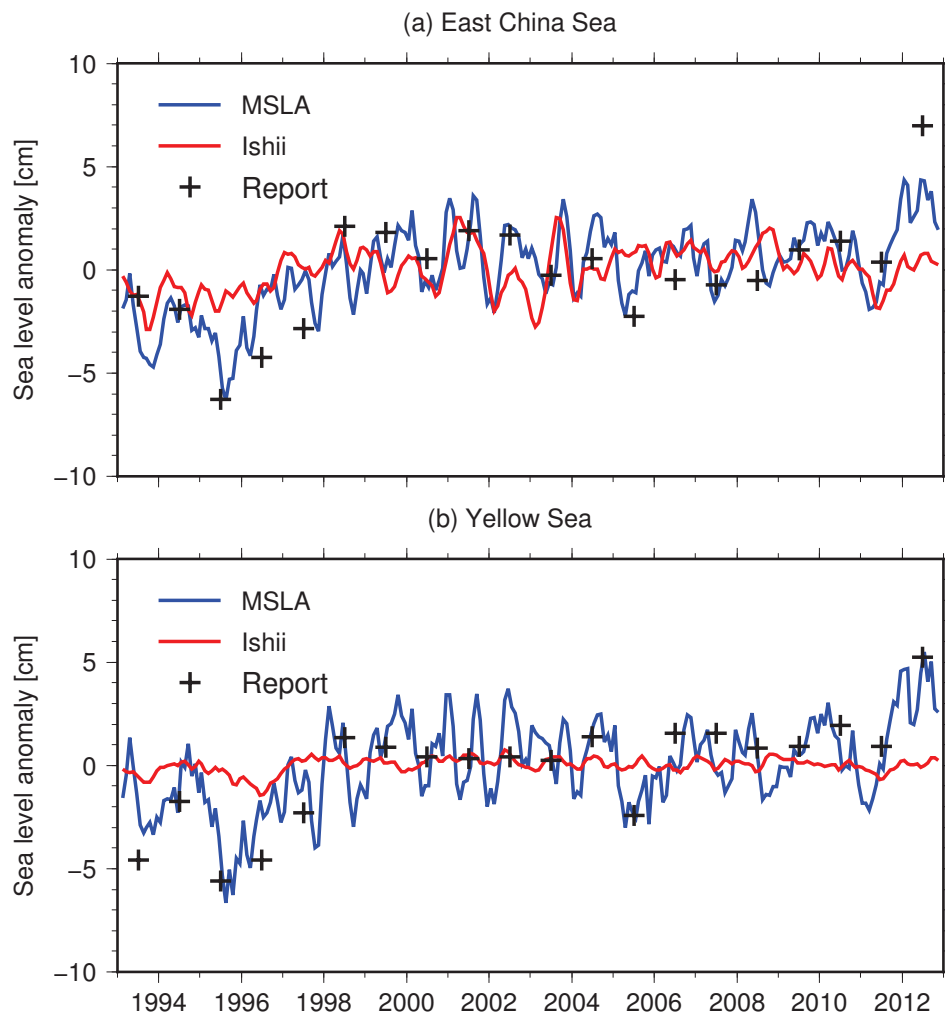


Figure 4.16: Interannual time series of total SLV from altimetry and steric SLV from Ishii in the ECS and YS during 1993-2012. Seasonal cycles are removed using least-square-fit and a 3-month moving average is applied. Yearly sea level variations released by the annual Sea Level Report of China from State Oceanic Administration of China are superimposed.

Table 4.5: Annual amplitudes (cm) and phases ($^{\circ}$) of total SLV from altimetry, steric SLV, thermosteric SLV, and halosteric SLV from Ishii in the ECS and YS during 1993-2012.

	East China Sea	Yellow Sea
	Amplitude (Phase)	Amplitude (Phase)
MSLA (altimetry)	7.8 ± 0.4 (257 ± 3)	7.6 ± 0.5 (251 ± 4)
Steric SLV (Ishii)	7.5 ± 0.2 (246 ± 2)	4.6 ± 0.1 (253 ± 1)
Thermosteric SLV (Ishii)	6.5 ± 0.2 (248 ± 2)	3.9 ± 0.1 (254 ± 1)
Halosteric SLV (Ishii)	1.1 ± 0.1 (227 ± 5)	0.8 ± 0.1 (250 ± 3)

4.2.6 Discussion and Summary

Among China seas, the East China Sea exhibits the largest seasonal variations of observed sea level from altimetry, which is generally high in September and low in March. Annual amplitude of steric SLV in this sea is also as high as 7.5 ± 0.2 cm, which is comparable with that from altimetry (7.8 ± 0.4 cm). Since the halosteric effect is rather small, the expansion and contraction of seawater due to temperature changes dominates the sea surface height changes in the ECS. It is well known that the Kuroshio Current is the main driving factor of this seasonal steric SLV in the ECS [Ichikawa and Beardsley, 2002; Jayne et al., 2009]. Nevertheless, intra-seasonal fluctuations of mass-induced SLV in the ESC is also obvious, both from steric-corrected altimetry and GRACE. In the Yellow Sea, the seasonal and intra-seasonal fluctuations of mass-induced SLV from steric-corrected altimetry and GRACE is more evident. Wakata [2009] established a simple ocean model to investigate the seasonal SLV along the East China Sea due to annual southward monsoons. Because of the sloping sea floor and seasonal strong monsoon winds, seawater mass and volume transport is considered to be the main reason of the continental boundary current and sea level seasonal variation in the East China Sea. In winter, strong monsoon blow from the northeast to the southwest; and vice versa in summer. Thus, the seasonal and intra-seasonal fluctuations of seawater mass change in the coastal region of the ECS and YS observed by steric-corrected altimetry and GRACE are most probably caused by the monsoon.

In the northern shallow water region of South China Sea, GRACE detects obvious seasonal variations of seawater mass with an annual amplitude of 5.0 ± 0.4 cm, which agrees with steric-corrected altimetry. For the SCS, Zhuang et al. [2010] established a regional ocean model forced by surface wind stress from QuickScat measurements. They focused on intra-seasonal variability in sea surface height over the SCS, and found striking variations on the northern of SCS shelf, which is strongest in autumn and weakest in spring. In response to the seasonal SCS monsoon, sea surface height rises and falls via Ekman transport and coastal waves [Zhuang et al., 2010]. The strong variations they found in the NSCS agrees well with our GRACE-observed seawater mass change in the same region. Thus, we conclude that, as in the ECS and YS, seawater mass variability on the shallow continental shelf of NSCS is also dominated by the response of sea level to seasonal wind stress forcing. As we discovered, the high-frequency variations of sea level modeled by Zhuang et al. [2010] in the shallow water of NSCS is also the case of ECS and YS (Figure 4.14c and Figure 4.15c).

In the deep ocean basin of South China Sea, the seasonal variability of SLV observed by altimetry is dominated by the thermosteric effect, i.e., the contribution of density changes due to expansion and contraction of seawater. The largest seasonal SLV is located in west of Luzon Island, which is consistent with an anticyclonic circulation in summer with maximum sea surface height in west of Luzon Island [Ho et al., 2000; Qu et al., 2000]. The annual amplitude of steric SLV in the ESCS reaches 6.7 ± 0.7 cm.

Over the whole SCS (depth > 200 m), both steric SLV from Ishii and mass-induced SLV from GRACE exhibit the evident seasonal variability. The annual amplitude of observed SLV from altimetry over the SCS is 3.2 ± 0.5 cm, peaking in mid-September. The annual steric SLV in the SCS leads the annual observed SLV ~ 44 days, while the annual mass-induced SLV lags the annual observed SLV ~ 57 days. It indicates that the ocean heat content in the SCS reaches maximum in early-August, while the ocean mass reaches maximum in mid-November. In Figure 4.4c, the observed SLV from altimetry show high correlations with “Ishii+GRACE” over most parts of SCS, except in the western part of central SCS, which is a dynamically active region. In summer, the southwesterly winds are blocked by Annam Cordillera (a north-south running mountain range on the east coast of Vietnam) and form a strong wind jet at its

southern tips. The accompanying wind stress curls result in the ocean upwelling off the coast [Qu et al., 2000; Xie et al., 2003]. We suspect that this eastward offshore flow and upwelling off Vietnam might cause the low correlation between altimetry and “Ishii+GRACE”.

On the interannual timescales, the mean SLV in the SCS from altimetry show large fluctuations, which are mainly caused by the steric effect. High correlation between interannual mean SLV in the SCS and NINO4 index indicates that sea level change in the SCS is driven by ENSO events on the interannual timescales. However, since 2008, the Ishii-based steric SLV in the SCS shows a long-term drift, which is significantly lower than the observed SLV. Considering the good agreement between interannual variability of steric SLV and observed SLV during 1993-2007, the reality of this drift is skeptical. However, good agreement between two temperature and salinity datasets (Ishii vs NODC) using different data processing strategies suggests that this drift is not caused by the difference in data processing procedure. So, what is suspicious is the uncertainty of oceanographic observations themselves. We further checked the steric SLV in the SCS using temperature and salinity outputs from the ECCO model. Different from steric SLV from Ishii and NODC, ECCO-based steric SLV in the SCS shows similar interannual fluctuations as the observed SLV from altimetry, and there is no obvious drift between them (Figure 4.12).

As another independent measurement, GRACE is used to validate the problem in Ishii and NODC datasets. Over the period 2003-2012, no significant long-term trend of mass-induced SLV is detected by GRACE, which agrees with ECCO-based steric-corrected altimetry. So, the rapid ocean mass increase estimated from Ishii-based steric-corrected altimetry is unreal. In other words, there exist systematic errors in oceanographic datasets.

It is worthwhile to mention that the existence of systematic errors in the oceanographic dataset has been proved before. Lombard et al. [2007] found that the Ishii-based steric SLV shows a dramatic negative trend since 2003, which is in complete disagreement with the estimate from altimetry minus GRACE. A net loss of $3.2 (\pm 1.1) \times 10^{22}$ J of heat from the upper ocean between 2003 and 2005 is claimed to be found from in situ ocean measurements too [Lyman et al., 2006]. Later, this cooling signal is proved to be an artifact that is mainly caused by systematic errors in eXpendable BathyThermograph (XBT) data [Ishii and Kimoto, 2009;

Willis et al., 2007]. When these biases are corrected, the ocean cooling signal becomes insignificant [Ishii and Kimoto, 2009; Willis et al., 2007]. With the improvement of quality and spatial distribution of in situ oceanographic observations, the systematic errors in the global mean steric SLV seems to be reduced significantly. However, our findings show that the systematic errors in oceanographic observations could be significant in some regional oceans and seas, e.g., the South China Sea. As shown in Figure 4.11, oceanographic observations successfully capture the observed sea level increase and decrease in the deep ocean basin of SCS over the period 1993-1999 and 2000-2004 respectively. However, the trend signal of SLV in the SCS from altimetry has migrated from deep ocean basin to surrounding shallow shelf over the period 2007-2012. Since the trend signal of SLV on shallow shelf from GRACE is insignificant, we conclude that there should be significant steric sea level rise on shallow shelf of SCS during 2007-2012. Unfortunately, oceanographic observations fail to capture this trend signal. We suspect that the steric sea level variations from in situ oceanographic observations in shallow water of SCS is totally underestimated. Considering the transfer of trend signal from deep ocean basin to shallow water, this problem emerges after 2008. So, the uncertainty on trend estimates of regional steric SLV from oceanographic observation is still large. More investigation should be carried out in the future.

4.3 Sea Level Variations in the Red Sea

4.3.1 Introduction

The Red Sea is a semi-enclosed basin and exchanges water with the Gulf of Aden through the strait of Bab-el-Mandeb at the southern end of the sea. The seasonally reversing Indian Monsoon (prevailing southerly and southeasterly winds in winter and northerly and northwesterly winds in summer) dominates the circulation in the southern Red Sea, while the northerly and northwesterly winds prevail in the northern Red Sea all the year round [Patzert, 1974]. There exist two distinct seasonal modes of water exchange between the Red Sea and the Gulf of Aden (Figure 4.17). In winter, the wind-driven fresh Gulf of Aden Surface Water (GASW) enters the Red Sea through the Bab-el-Mandeb above the Red Sea Outflow Water (RSOW). In summer,

a three-layer flow structure prevails in the strait of Bab-el-Mandeb. The northerly and north-westerly monsoon winds drive surface currents and RSOW outflow, while an upwelling of Gulf of Aden Intermediate Water (GAIW) penetrates into the south of the Red Sea [Cromwell and Smeed, 1998; Murray and Johns, 1997; Smeed, 1997]. A lot of previous studies have reported the seasonal variations of the flow between the Red Sea and the Gulf of Aden, validated from flux observations [Murray and Johns, 1997], XBT data [Smeed, 1997] and ocean models [Siddall et al., 2002; Sofianos and Johns, 2002]. Besides these hydrographic observations and models, the development of satellite altimetry provides more information on ocean dynamics [Fu and Cazenave, 2001]. Sofianos and Johns [2001] found a good agreement between TOPEX/Poseidon altimetry data and the predictions from a simple model that balances the sea surface elevation against the wind stress. They concluded that the basic mechanism responsible for the sea level variations (SLV) in the Red Sea on seasonal timescales is the wind pattern. In fact, wind stress can also cause the ocean mass change and ocean bottom pressure change, which can be detected by satellite gravimetry. Many studies have shown that GRACE has been successfully used to estimate the mass-induced SLV in global oceans and regional seas on seasonal and interannual timescales. The annual amplitude of global mean ocean mass variations detected by GRACE is about 7 mm [Chambers et al., 2004; Leuliette and Willis, 2011]. However, seawater mass variation signal can be tens of times higher than the global mean value in some regional shallow seas. For example, GRACE observes an amplitude of ~ 20 cm ocean mass variations in the Gulf of Thailand and ~ 40 cm in the Gulf of Carpentaria [Tregoning et al., 2008; Wouters and Chambers, 2010]. Besides these two gulfs, Fenoglio-Marc et al. [2006] and García et al. [2006] studied the seasonal SLV in the Mediterranean Sea using altimetry, ocean models and GRACE. Furthermore, Calafat et al. [2010] found a seawater mass increase in the Mediterranean Sea from GRACE over the period 2002-2006, which is consistent with the result from the steric-corrected altimetry. Swenson and Wahr [2007] found a good agreement between the GRACE-derived SLV and the steric-corrected altimetry observations in the Caspian Sea on seasonal and interannual timescales.

The subject of this study is to analyze the mass-induced SLV in the Red Sea using GRACE, and compare the results with those from steric-corrected altimetry, in-situ bottom pressure

records, and hydrographic observations. The Red Sea is an ideal study target for GRACE since it is nearly enclosed and surrounded by dry areas. Thus, the leakage from hydrological signals outside the Red Sea is relatively small for GRACE-derived mass variations in the region. In addition, the area of the Red Sea is large enough (438,000 km²) for GRACE to detect the mass-induced SLV. All these conditions provide the possibility to estimate seawater mass variations in the Red Sea using GRACE. This study has led to the publication of a paper [Feng et al., 2014], which was the first one published on this topic. Later, Wahr et al. [2014] also reported the similar results in the Red Sea.

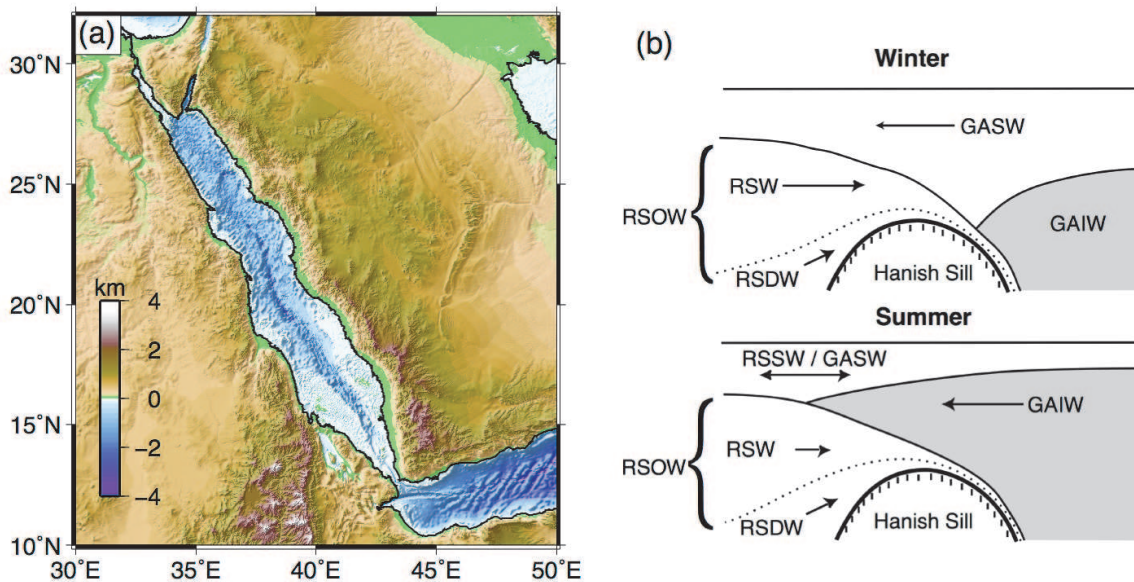


Figure 4.17: (a) Map of Red Sea bathymetry and surrounding topography. (b) The seasonal exchange regime in the Red Sea. GAIW is Gulf of Aden Intermediate Water, GASW is Gulf of Aden Surface Water, RSOW is Red Sea Overflow Water, RWS is Red Sea Water, RSDW is Red Sea Deep Water, RSSW is Red Sea Surface Water. Panel b is from Siddall et al. [2002].

4.3.2 Data and Processing

4.3.3 GRACE Data

To estimate the mass-induced SLV in the Red Sea, we use two sets of GRACE products, i.e., ten-day Release-02 products from the Groupe de Recherche de Géodésie Spatiale (GRGS) [Bruinsma et al., 2010; Lemoine et al., 2007] and monthly Release-05 products from the

Center for Space Research (CSR) at the University of Texas at Austin [Bettadpur, 2007]. It must be noted that these two sets are based on different releases of the GRACE Level-1B measurements: GRGS-RL02 is based on version 1 of the Level-1B measurements, whereas CSR-RL05 is based on the more recent version 2 of the same data which was reprocessed and released in 2012 by JPL. These two GRACE products are expressed in the form of spherical harmonic (SH) geopotential coefficients up to degree and order (d/o) 50 for GRGS and d/o 60 for CSR. These solutions are derived using different gravity inversion strategies. The GRGS GRACE products are stabilized towards the EIGEN-GRGS.RL02.MEAN-FIELD mean gravity field at each given epoch, with a constraint law that depends on the degree and on the order of each coefficient (<http://grgs.obs-mip.fr/grace>). Thus there is no need to de-stripe and smooth the GRGS solutions. The CSR solutions are unconstrained solutions and usually need de-stripping and Gaussian smoothing to reduce the correlated north-south-oriented stripes and short-wavelength random noises [Swenson and Wahr, 2006; Wahr et al., 1998]. We adopt the de-stripping filter proposed by Chambers [2006] to reduce the stripes in CSR solutions. Comparison of these two GRACE solutions derived from different processing strategies allows us to estimate the confidence of GRACE-derived mass variations in the Red Sea.

For both GRACE solutions, atmospheric pressure and ocean mass variations have been modeled and removed. To be consistent with steric-corrected altimetry for oceanographic analyses, these removed models have to be added back [Willis et al., 2008]. For CSR, ECMWF operational atmospheric model and the baroclinic OMCT ocean model are added back using CSR RL05 GAD products to recover the ocean bottom pressure (OBP) [Bettadpur, 2007]. For GRGS, ECMWF atmospheric model and the barotropic MOG2D ocean model [Carrère and Lyard, 2003] are restored using GRGS RL02 GAA and GAB products. In order to make GRACE-derived ocean mass changes comparable with inverse-barometer corrected altimetry data, we further remove the time-variable mass of the atmosphere averaged over the global ocean [Leuliette and Miller, 2009; Willis et al., 2008]. The GRACE data are further corrected for glacial isostatic adjustment (GIA) based on the model of Paulson et al. [2007].

Since the SH coefficients of GRACE data are truncated to some d/o (50 for GRGS and 60 for CSR) and filtered (in the case of CSR), the mass signal in the Red Sea may be contaminated

by the leakage from continental hydrology and ocean mass change outside. To estimate the mass-induced SLV time series using GRACE, we first have to remove the above mentioned leakage time series. Thus, we construct a synthetic mass change model based on soil moisture data from the Noah land surface model produced by NASA's Global Land Data Assimilation System [Ek et al., 2003; Rodell et al., 2004] and ocean bottom pressure data from a JPL version of the Estimating Circulation and Climate of the Ocean general model [Lee et al., 2002]. We add a uniform layer to the global ocean to conserve the total land and ocean mass at every time step [Velicogna and Wahr, 2006b]. The synthetic gridded data (zeros in the Red Sea) are converted to the SH coefficients, truncated to some d/o (50 for GRGS and 60 for CSR), filtered (in the case of CSR) and spatially averaged to get the leakage time series.

In addition, the truncation and filtering of SH coefficients would make the amplitude of GRACE-based estimate in the area of interest damped. To restore the “real” mass variation signal in the Red Sea, we multiply the leakage-removed time series with a scaling factor [Swenson and Wahr, 2007; Velicogna and Wahr, 2006b]. For GRGS, we construct a mask grid (1 inside the Red Sea, 0 outside) and convert it to SH coefficients truncated to d/o 50, which reduces the amplitude by a factor 0.55. Thus the GRACE-derived mass-induced SLV series from GRGS are multiplied by $1/0.55$ (i.e., 1.81) to recover the “real” mass variation signal in the Red Sea. In the case of CSR, we compare the restored mass change time series using different scaling factors corresponding to the Gaussian smoothing with the half-width varying from 0 km to 500 km. We find that the Gaussian smoothing with different half-width produces insignificant differences in the Red Sea. The variance of the difference between restored time series using 0 km Gaussian smoothing and reference series from steric-corrected altimetry is smaller than other restored time series. Consequently we only do the de-striping to CSR solutions, but no Gaussian smoothing is applied. The scaling factor corresponding to 0 km Gaussian smoothing is 1.59 for CSR. Briefly, we firstly remove the leakage time series from the original GRACE-observed mass-induced SLV time series, and then multiply the scaling factors to the leakage-removed time series to recover the unbiased mass-induced SLV time series from GRACE. The uncertainty of GRACE-derived mass-induced SLV time series is estimated using the method proposed by Wahr et al. [2006], which are 3.4 cm for the

monthly CSR values and 4.2 cm for ten-day GRGS values. To be consistent with monthly CSR values and steric-corrected altimetry results, monthly-average GRGS values are estimated, the uncertainty of which is 2.4 cm.

4.3.4 Steric-corrected Altimetry Data

We use the merged Maps of Sea Level Anomalies (MSLA) derived from TOPEX/Poseidon, Jason-1/2, ERS-1/2 and Envisat, which are provided by the Archiving, Validation and Interpretation of Satellite Oceanographic (AVISO) data (for details, see the AVISO User Handbook available at <http://www.aviso.oceanobs.com/>). Here we use the $0.25^\circ \times 0.25^\circ$ gridded data at monthly interval for the period of January 2003 to December 2011. All standard geophysical and environmental corrections have been applied, including the ionospheric correction, dry and wet tropospheric corrections, solid Earth and ocean tides, ocean tide loading, pole tide, electromagnetic bias, inverted barometer corrections and instrumental corrections. The uncertainty of altimetry-derived monthly SLV in the Red Sea is about 2.3 cm, based on the error files provided by AVISO.

Owing to the elastic loading effect, mass change in the water column produces a deformation in the sea bottom, which may not be negligible in the altimetry data [Kuo et al., 2008]. We estimate the loading effect from GRACE data and remove it from altimetry. The peak-to-peak amplitude of loading deformation in the Red Sea is about 10 mm, accounting for about 3% of steric-corrected altimetry observations. The GIA effect on the long-term sea bottom deformation is also removed from altimetry, which is negligible in the Red Sea [Paulson et al., 2007]. To estimate the steric SLV in the Red Sea, we use the latest oceanographic temperature and salinity dataset provided by Ishii et al. [2006] for the period of January 2003 to December 2011 ($1^\circ \times 1^\circ$ global grids at monthly interval). The steric SLV calculated from Ishii dataset are further interpolated to match the spatial resolution of altimetry observations, and then be removed from altimetry to get the steric-corrected SLV. However, the coverage of original year-to-year hydrographic data in the Red Sea is poor and mapping approach is used to fill the gaps [Ishii et al., 2006]. The uncertainty in the Ishii-based steric SLV in the Red Sea could be significant, so we further verify the validity of the Ishii-based steric SLV using the NOAA's

World Ocean Atlas (WOA09) climatological hydrographic data [Levitus et al., 2009]. Both data show similar spatial patterns and magnitudes. The uncertainty of the Ishii-based steric SLV is assessed using the RMS difference between the Ishii-based steric SLV and the WOA-based steric SLV in the Red Sea (i.e., 1.5 cm). The uncertainty of the steric-corrected SLV is estimated to be 2.7 cm assuming that errors in the altimetry data and the Ishii data are uncorrelated.

4.3.5 Bottom Pressure Records

We use ocean bottom pressure (OBP) time series from three bottom pressure records (BPRs) at Jeddah, Thuwal and Rabigh along the Saudi Arabian coast, which are deployed by King Abdullah University of Science and Technology (KAUST) and Woods Hole Oceanographic Institution (WHOI) (Figure 4.18b). The period of BPRs covers April 2008 to May 2011 with a temporal resolution of 5 minutes (available at <http://www.whoi.edu/science/PO/coastal/RedSeaPressure/index.html>). Monthly means of BPRs observations are derived to be consistent with GRACE results. OBP time series from three BPRs agree well with each other (correlations > 0.99). The RMSs among them are smaller than 2 cm. So three BPRs series are averaged to compare with GRACE results.

4.3.6 Results and Discussion

Seawater Mass Variations from Steric-corrected Altimetry and GRACE

In order to make the steric-corrected altimetry and GRACE comparable in spatial domain, we convert steric-corrected altimetry grids to SH coefficients and truncate them to d/o 50 (corresponding to ~ 400 km resolution). SH coefficients of CSR solutions are also truncated to d/o 50 to be consistent with GRGS solutions. As stated before, we only do the de-stripping to CSR solutions and no Gaussian smoothing is applied. Figure 4.18a shows the annual amplitude of steric-corrected altimetry in the Red Sea from 2003 to 2011, which reaches a maximum of ~ 13 cm in the central part of the Red Sea. The spatial patterns of mass-induced annual SLV's amplitude from GRGS and CSR also show high amplitude in the same region of the Red Sea

(Figure 4.18b-4.18c), which agree well with that of the steric-corrected altimetry. To investigate the reason of dome-shaped annual mass variations, we compute the annual amplitude of the original steric-corrected altimetry grids, which shows the homogeneous annual mass variations in the Red Sea (not shown). It indicates that the spherical harmonic truncation of the narrow and elongated Red Sea induces the signal attenuation in the two ends of the sea and causes the latitudinal mass variations from truncated steric-corrected altimetry. For the same reason, the limitation of GRACE's resolution causes the same spatial patterns shown in Figure 4.18b and 4.18c. The annual phase of mass variations from steric-corrected altimetry is fairly homogeneous in the Red Sea and is in good agreement with GRACE results (Figure 4.18d-4.18f). In the Red Sea, seawater mass variations generally reach maximum in late January/early February.

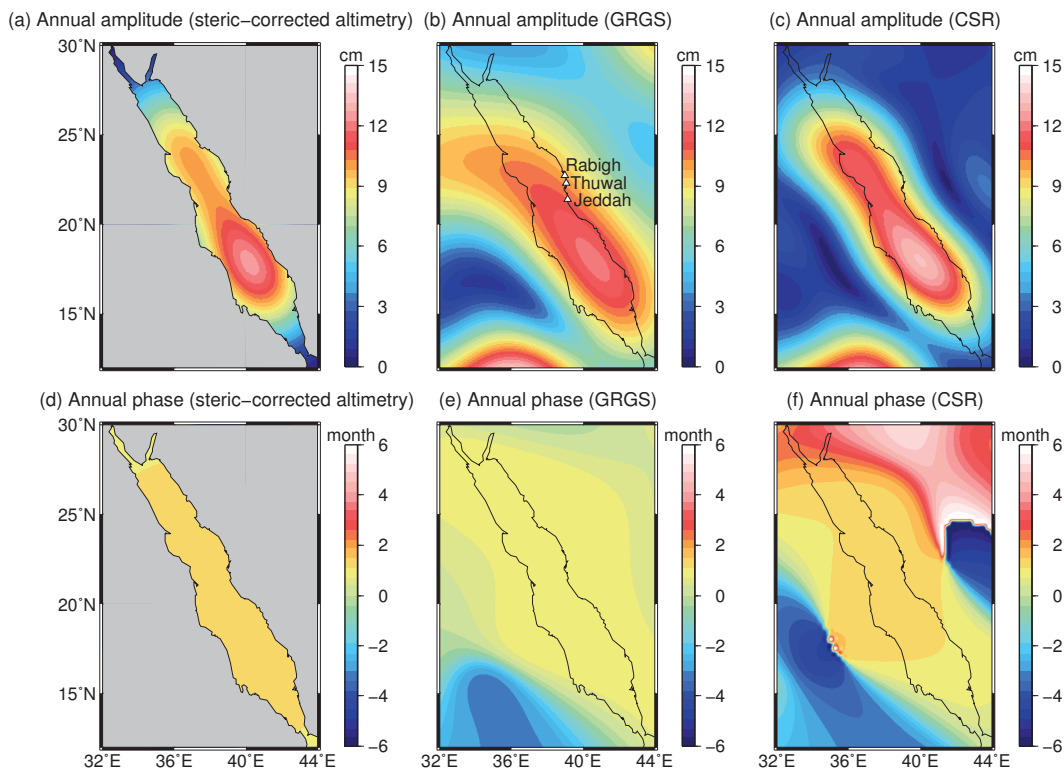


Figure 4.18: Annual amplitude of mass-induced SLV in the Red Sea from (a) steric-corrected altimetry, (b) GRGS, and (c) CSR. (d-f): Same as (a-c), but for annual phase. Harmonic analysis is used to obtain the annual amplitude and phase. Locations of three BPRs (Jeddah, Thuwal, and Rabigh) are shown in panel (b).

In addition to the good agreement in spatial patterns of annual cycle, the mean mass vari-

ation time series in the Red Sea from steric-corrected altimetry and GRACE also agree well with each other (Figure 4.19a). The correlation coefficient between steric-corrected altimetry and GRGS/CSR is 0.93/0.95 (95% confidence intervals, 0.90-0.95/0.93-0.97). We further calculate the magnitude squared coherences between every two series with Matlab's `mscohere` function using Welch's averaged modified periodogram method [Welch, 1967], and the confidence level estimated using the method proposed by Carter [1987]. As shown in Figure 4.20, the maximum and second maximum peaks of the coherence curve between steric-corrected altimetry and GRACE occur in the annual and semi-annual cycle. Coherences between CSR and GRGS also show the similar characteristics. At frequencies lower than 1.3 cycle/yr, CSR results agree with steric-corrected altimetry better than GRGS, which is confirmed from the interannual time series in Figure 4.19b too. However, at frequencies from 1.4 cycle/yr to 2.5 cycle/yr, GRGS series give higher coherences with steric-corrected altimetry. At higher frequencies (>2.5 cycle/yr), CSR-altimetry coherences become higher again than GRGS-altimetry coherences, which indicate CSR series perform better than GRGS series. Significant coherence occurs between 0.3 and 2.8 cycle/yr for GRGS-altimetry and GRGS-CSR. However, coherences between CSR and steric-corrected altimetry are significant in most frequency bands. The origin of the different performance between CSR and GRGS results probably lies in the way the two series are processed in order to avoid the striping inherent to unconstrained solutions. In the GRGS products, a small constraint is applied in the inversion process towards an a priori mean field, which contains annual and semi-annual terms. Thus the 1 cycle/yr to 2 cycle/yr signal is well preserved while the signals at other frequencies tends to be attenuated. In the case of the CSR products, the removal of the striping is obtained through a post-processing (de-striping and Gaussian smoothing), thus producing a small attenuation of the signal at all frequencies, but with a uniform treatment over all the frequencies.

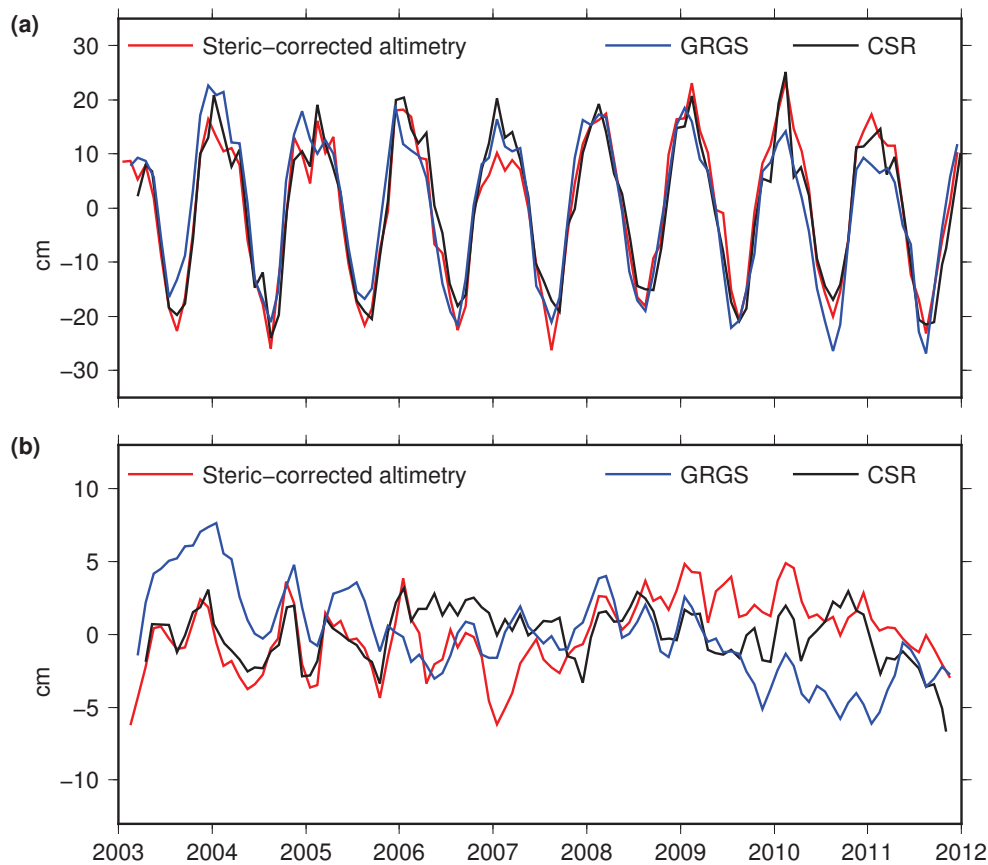


Figure 4.19: (a) Time series of seawater mass variations in the Red Sea estimated from steric-corrected altimetry (red), GRGS (blue), and CSR (black). A scaling factor of 1.81/1.59 is applied to GRGS/CSR time series to restore the “real” mass variation signal in the Red Sea. (b) Same as panel (a), but with seasonal cycles removed. A 3-month boxcar smoothing is applied in panel (b).

As listed in Table 4.6, the annual amplitude of mass-induced SLV from GRGS/CSR is 17.5/17.7 cm and peaks in late January/early February. The steric-corrected SLV from altimetry have an annual amplitude of 17.8 cm peaking early in February, which agree well with GRACE (GRGS/CSR) results. The annual amplitude of the steric SLV here is 2.6 cm, which is significantly smaller than that of the mass-induced SLV. Small steric SLV indicate that the mean SLV in the Red Sea are dominated by seawater mass variations on the annual timescale. The out-of-phase relationship between the steric SLV and the mass-induced SLV indicates that when the Red Sea gains the mass from inflow water in winter, the steric SLV fall, and vice versa in summer.

On the interannual timescales, the mass-induced SLV from CSR are in good agreement with the steric-corrected SLV from altimetry before 2006 (Figure 4.19b). However, GRGS series show a negative trend from 2003 to 2006, which is significantly different from CSR and altimetry results. Nevertheless, the peaks of three series from 2003 to 2006 match well. Since then, steric-corrected SLV from altimetry rise from 2007 to 2008 and decrease since 2010. However, the interannual mass-induced SLV from GRACE after 2007 do not agree with altimetry so well as that happens for the period 2003-2006. It indicates there is still relatively large uncertainty in the estimation of interannual water mass changes in the Red Sea from GRACE and steric-corrected altimetry. The discrepancy between two independent satellite results might result from the uncertainty in GRACE and that in steric SLV.

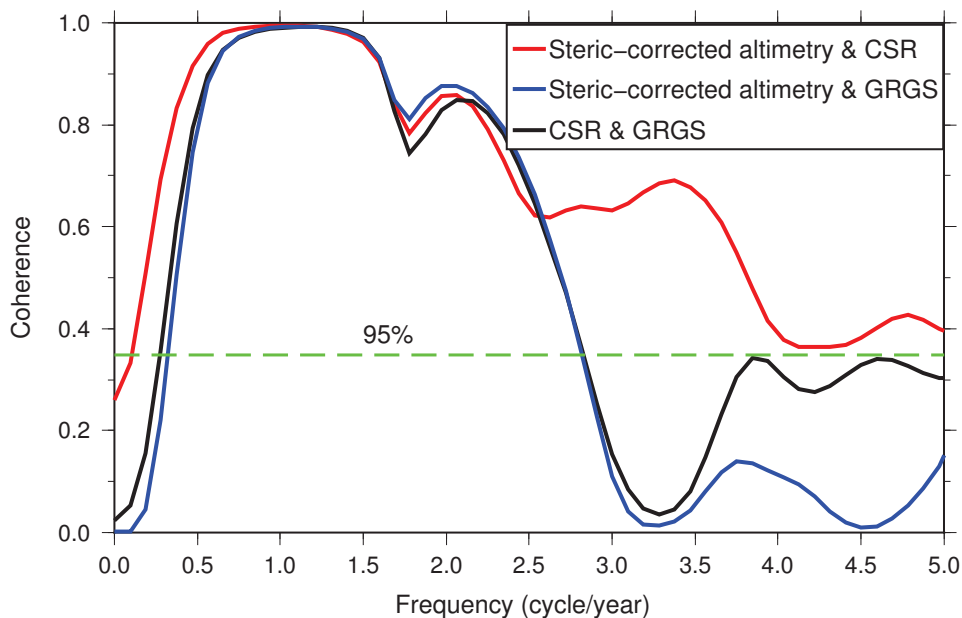


Figure 4.20: Coherences between steric-corrected altimetry and GRGS, steric-corrected altimetry and CSR, and GRGS and CSR at different frequencies. The dashed horizontal green line indicates significance at the 95% confidence level.

Table 4.6: Annual amplitudes and phases of different SLV components in the Red Sea from 2003 to 2011. Uncertainties in amplitudes and phases have been estimated as two standard deviations after propagation of monthly value errors in the least squares fit procedure, which represent the 95% confidence interval.

	Annual amplitude (cm)	Annual phase ($^{\circ}$)
Altimetry	15.7 ± 0.6	32 ± 2
Steric SLC (Ishii)	2.6 ± 0.4	239 ± 9
Altimetry-Steric SLV	17.8 ± 0.7	37 ± 2
Mass-induced SLV (GRGS)	17.5 ± 0.7	29 ± 2
Mass-induced SLV (CSR)	17.7 ± 1.0	38 ± 2

Comparison Between BPRs and GRACE

Besides the comparison between GRACE and steric-corrected altimetry, we further validate GRACE-derived mass variations in the Red Sea with some in-situ BPRs. As shown in Figure 4.21a, OBP time series from BPRs, GRGS and CSR show strong annual cycles and have generally good agreement with each other. The correlation between OBP series from BPRs and GRGS/CSR is 0.96/0.88 (95% confidence intervals, 0.92-0.98/0.78-0.94). The annual amplitude and phase of OBP time series from BPRs are 20.1 ± 1.7 cm and $28^{\circ} \pm 5^{\circ}$, which agree with GRGS results (18.1 ± 1.1 cm, $33^{\circ} \pm 3^{\circ}$) better than CSR results (12.8 ± 2.0 cm, $46^{\circ} \pm 15^{\circ}$). The root-mean-square (RMS) of OBP difference between GRGS and BPRs is 4.5 cm, which is smaller than that between CSR and BPRs (7.9 cm). In addition, the annual signal observed by BPRs along the Saudi Arabian coast is also consistent with mean water mass variations in the Red Sea from steric-corrected altimetry (Table 4.6). We further remove seasonal cycles and trends from time series to get the residuals of OBP time series (Figure 4.21b). The correlation of residual time series between CSR and BPRs is 0.69 (95% confidence interval, 0.43-0.84), which is significantly higher than the correlation between GRGS and BPRs (i.e., 0.28).

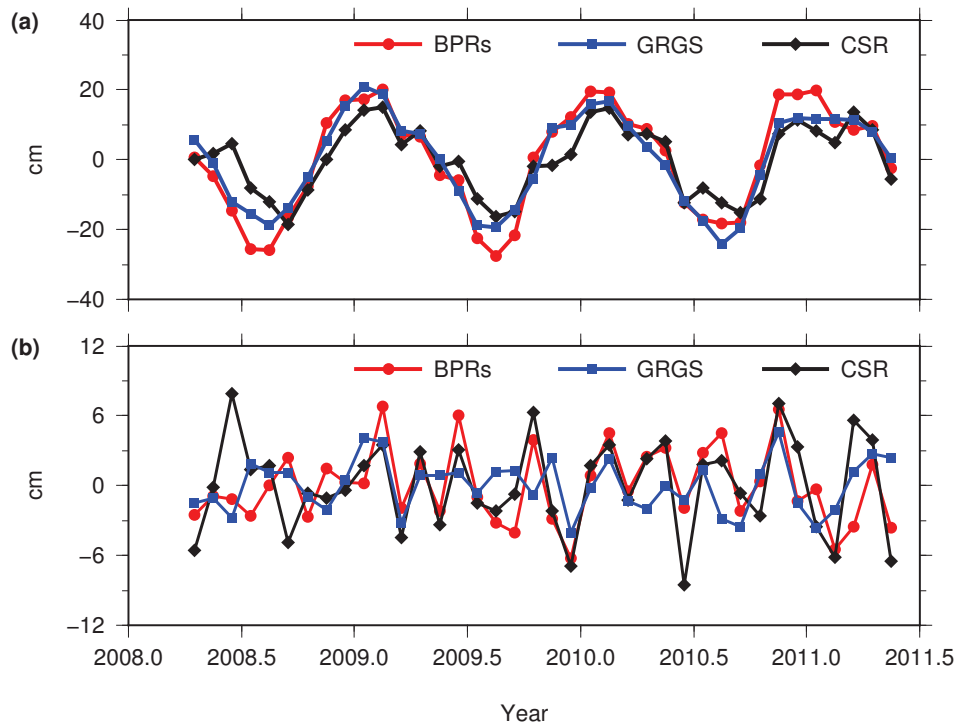


Figure 4.21: (a) Time series of OBP along the Saudi Arabian coast of Red Sea measured by BPRs and GRACE (GRGS/CSR). (b) Same as panel (a), but with seasonal cycles and trends removed.

Horizontal Water Mass Flux

The water mass fluxes of the Red Sea are the sum of horizontal mass flux (i.e., runoff from rivers, water exchange through Bab-el-Mandeb) and vertical mass flux (i.e., evaporation and precipitation), which can be measured by GRACE and steric-corrected altimetry. To isolate the horizontal mass flux of the Red Sea, the vertical mass flux has to be removed from GRACE and steric-corrected altimetry. The land adjacent to the Red Sea is very arid and the precipitation is small. The evaporation rate here is one of the highest in the world ocean with a mean net rate of 2.06 ± 0.22 m/yr [Sofianos et al., 2002]. Here we adopt the climatological monthly precipitation minus evaporation (P-E) data from Sofianos and Johns [2002] to estimate the vertical mass flux of the Red Sea, which is further removed from GRACE and steric-corrected altimetry to obtain the horizontal mass flux. The runoff from rivers near the Red Sea is negligible [Siddall et al., 2004]. So the water exchange through the Bab-el-Mandeb, the only

substantial connection to the open ocean, represents the horizontal mass flux of the Red Sea. Sofianos et al. [2002] estimated the freshwater volume budget, temperature and salinity at Bab-el-Mandeb from current-meter arrays and temperature-salinity chain moorings between June 1995 and November 1996. We further estimate the horizontal water mass flux through the Bab-el-Mandeb using water volume fluxes, temperature and salinity data from [Sofianos et al., 2002]. The horizontal water mass flux from these hydrographic observations is converted to equivalent water height for comparison with results from GRACE and steric-corrected altimetry. Considering there are no more than two years' water flux observations at Bab-el-Mandeb and its time range is different from that of altimetry and GRACE, we only calculate the climatological monthly horizontal water mass flux in the Red Sea from hydrographic observations, GRACE, and steric-corrected altimetry.

As shown in Figure 4.22, the climatological horizontal water mass fluxes estimated from steric-corrected altimetry and GRACE (GRGS/CSR) show strong similarities in signatures and magnitudes. The uncertainty assessment of results from steric-corrected altimetry and GRACE indicates that they lie well within the error bars (Figure 4.22). These two independent satellite-based results indicate that the seawater flows into the Red Sea reaching maximum in October/November, which leads the estimate from hydrographic observations about three months. The root-mean-square (RMS) of horizontal mass flux from hydrographic observations (~ 6 cm/month) is only 60% of the size of satellite-based estimates (~ 10 cm/month for GRACE and steric-corrected altimetry).

The discrepancies in amplitude and phase between hydrographic observations and two sets of satellite-based estimates can have several explanations. One main problem is the interannual variability of horizontal mass flux. We calculate the horizontal mass flux series from 2003 to 2011 based on GRACE and steric-corrected altimetry, then retrieve the maximum and minimum values of estimates in the same month of different years, which are shown as the two blue dash-dot lines in Figure 4.22. Most of the flux estimates from hydrographic observations are within the envelope of interannual variability of satellite-based estimates (Figure 4.22). Note that the hydrographic observations at Bab-el-Mandeb were carried out for an 18-month period between June 1995 and November 1996 [Sofianos et al., 2002]. Therefore, the interannual

variability of horizontal mass flux can explain the discrepancies between hydrographic observations and satellite-based estimates in Figure 4.22. Another potential explanation could be the uncertainties in hydrographic observations (i.e., velocity, temperature, and salinity profiles at Bab-el-Mandeb), which might result in the uncertainty in horizontal water flux estimates too. In addition, the vertical water mass flux corrections (i.e., P-E), which are used to isolate the horizontal flux from steric-corrected altimetry and GRACE, could induce the discrepancies too. Seasonal P-E variability peaks in November [Sofianos and Johns, 2002], which agrees with the seasonal horizontal mass flux from steric-corrected altimetry and GRACE. The RMS of seasonal P-E variability is about 3 cm/month based on the results from Sofianos and Johns [2002], which accounts for 30% of seasonal horizontal mass flux variability from steric-corrected altimetry and GRACE. Therefore, the P-E corrections might have a potentially significant impact on the horizontal mass flux estimation from satellite observations too.

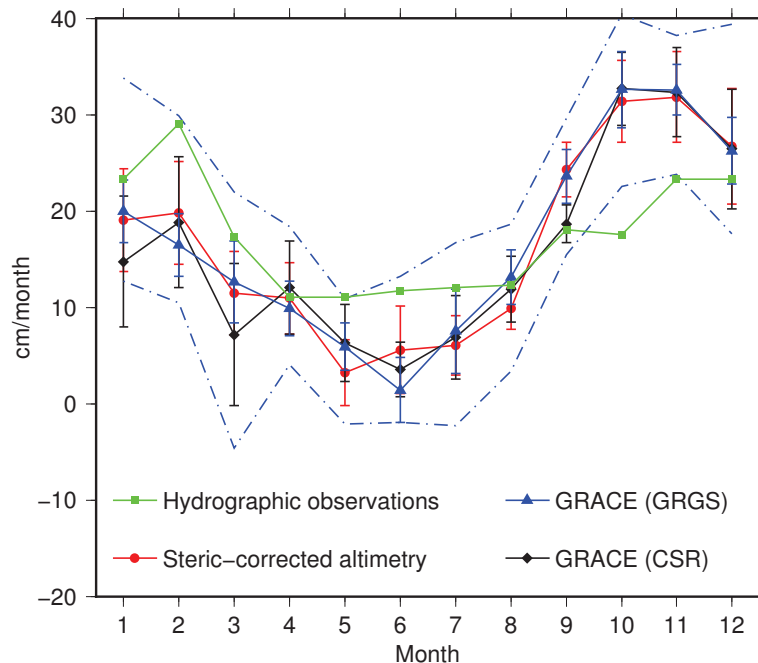


Figure 4.22: The climatological monthly horizontal water mass fluxes in the Red Sea estimated from steric-corrected altimetry, GRACE (GRGS/CSR), and hydrographic observations. The error bars represent the standard deviations of climatological flux estimates in the same month of different years based on the steric-corrected altimetry and GRACE. The two blue dash-dot lines represent the upper and lower bounds of estimates from steric-corrected altimetry and GRACE during 2003-2011.

Although there are discrepancies in amplitude and phase between hydrographic observations and two sets of satellite-based estimates, the mean flux estimates from hydrographic observations, steric-corrected altimetry, GRGS, and CSR are 17.5 cm/month, 16.7 cm/month, 16.8 cm/month, and 16.0 cm/month, respectively, which agree well with each other.

4.3.7 Summary

In this study, we have shown that GRACE satellites successfully detect the significant seasonal water mass variations in the Red Sea, which increase in winter when the Red Sea gains the water mass from the Gulf of Aden and vice versa in summer. The annual amplitude of the mass-induced SLV inferred from GRACE is ~ 18 cm, which agrees well with that from steric-corrected altimetry. The annual steric component of the mean SLV calculated from oceanographic temperature and salinity data is relatively small and peaks about seven months later than mass variations. It indicates that the steric and mass-induced contributions to the annual SLV in the Red Sea counteract each other.

A first comparison of in-situ OBP with GRACE in the Red Sea also reveals large annual seawater mass variations. GRGS GRACE solutions agree with in-situ OBP observations better than CSR solutions both in annual amplitude and phase. However, CSR solutions exhibit higher correlation with in-situ OBP when seasonal cycles and trends are removed.

The climatological monthly horizontal water mass flux estimated from hydrographic observations is in general agreement with that from GRACE and steric-corrected altimetry, while some discrepancies in magnitude and phase is found. Considering the timespan of the hydrographic observations is different from that of two sets of satellite observations, the interannual variability of horizontal water mass flux is most likely to explain these discrepancies. In the future, more than two years' long-term hydrographic observations in the Red Sea would be able to give another independent measure to validate the interannual water mass flux estimated from GRACE satellites and steric-corrected altimetry.

CONCLUSIONS AND FUTURE WORK

5.1 Conclusions

This thesis contains two major parts. In the first part, we investigated the groundwater storage (GWS) variations in North China using GRACE and land surface models, and compared the results with the estimates from in situ groundwater observations, groundwater model, and official bulletins. An important finding of this part is that GRACE successfully observes the seasonal variations of groundwater storage in North China, and isolates the effect of anthropogenic irrigation from that of natural precipitation. From spring to summer, although the precipitation increases, the extensive irrigation for wheat growing results in a significant groundwater depletion in the North China Plain (NCP). After the harvest of wheat in June, the decrease of irrigation demand for the drought-tolerant maize and the abundant precipitation result in the recharge of groundwater aquifers from summer to winter. This seasonal variability of groundwater in the NCP is detected by GRACE for the first time, and there is a good agreement between GRACE and ground observations. GRACE also observes the obvious interannual fluctuations of GWS in the NCP, which is consistent with year-to-year precipitation anomalies. The largest GWS depletion observed by GRACE occurs in the piedmont of NCP, which is confirmed by groundwater observations and groundwater model. It is worthwhile to note that a significant increase of GWS from 2012 to 2013 is detected by GRACE, which corresponds to the abundant precipitation in these two years. Besides the interannual fluctuations,

there exists a long term groundwater depletion in North China, at a rate of $7.1 \pm 1.0 \text{ km}^3/\text{yr}$ from GRACE. However, the groundwater depletion rates in shallow aquifers according to in groundwater observations and official bulletins are 1.2 and 2.0 km^3/yr , respectively, which are significantly lower than the GRACE estimate. We conclude that GRACE observes the important contribution from deep aquifers to the groundwater depletion in the plain and piedmont regions of North China, which was underestimated until now.

In the second part, we focused on regional sea level variations in China seas and in the Red Sea using GRACE, altimetry, and oceanographic data. Large seasonal mass variations in the northern shallow water of South China Sea (SCS) are detected by GRACE and steric-corrected altimetry, while thermosteric sea level variations (SLV) dominate the total SLV in the deep ocean basin of eastern SCS on seasonal timescales. On interannual timescales, sea level fluctuations in the SCS are dominated by the thermosteric effect and driven by El Niño-Southern Oscillation (ENSO) events. More importantly, a systematic drift of steric SLV calculated from oceanographic observations is identified in the SCS, which is confirmed by the comparison with altimetry and GRACE. The altimetric SLV in the East China Sea (ECS) and the Yellow Sea (YS) mainly reflect the thermal expansion and contraction of seawater on seasonal timescales. Nevertheless, GRACE detects intra-seasonal mass variations in the ECS and YS, which agree with steric-corrected altimetry. For the Red Sea, large seasonal variability of seawater mass is also detected by GRACE and steric-corrected altimetry, which is well explained by the water exchange between the Red Sea and the Gulf of Aden driven by the seasonal reversal of monsoon. In-situ bottom pressure records at the eastern coast of the Red Sea confirm the GRACE observations too. In addition, the horizontal water mass flux observed by current-meter arrays at Bab-el-Mandeb, i.e. the mouth of the Red Sea, further validate our GRACE estimates.

5.2 Future Work

Besides GRACE, other geodetic observations can also provide the information on groundwater storage variations. It is important to note that secular extensive groundwater pumping

of deep confined aquifers has resulted in many large-scale cones of depression in the NCP [Liu et al., 2001; Ministry of Land and Resources of China, 2009]. The ground subsidence in cones of groundwater depression can be detected by geodetic observations from Global Navigation Satellite System (GNSS) and Interferometric Synthetic Aperture Radar (InSAR). The ground deformation velocity in the central NCP between 2007 and 2010 was estimated by using differential InSAR technique [Zhang et al., 2013]. A recent study also indicated that the seasonal elastic ground deformation caused by withdraw and recharge of aquifers can be detected by InSAR [Chaussard et al., 2014]. In addition, the existing ground gravity observations in the NCP from the Crustal Movement Observation Network of China (CMONC) can also provide the underground mass variation information, if the vertical deformation effect and surface mass variations can be removed. Assimilating these geodetic observations, which are in different spatial and temporal resolutions, into the groundwater model, will probably improve the estimation of current GWS variations and the prediction of GWS variations in future (personal communication, C. M. Zheng).

Currently, the spatial resolution of GRACE results is limited to 300-500 km, which limits our knowledge on mass variations at the finer spatial scales. The GRACE Follow-On mission, scheduled for launch in 2017, may provide us mass variations of the Earth system in a higher spatial resolution with an experimental interferometric laser ranging system (<http://gracefo.jpl.nasa.gov/>). In addition, more advanced gravity satellite missions (e.g., GRACE II and e.motion) have been proposed by scientific communities [Panet et al., 2013]. Besides these gravity missions, the Surface Water and Ocean Topography (SWOT) satellite, a joint NASA-CNES mission, is planned to be launched in 2019. Over land, SWOT can measure water surface height changes in all wetlands, lakes, and reservoirs whose area exceeds 250 m²; over ocean, SWOT can measure ocean currents and eddies at scales shorter than 200 km (<https://swot.jpl.nasa.gov/>). By analyzing the water surface height variations from SWOT and water mass variations from future gravity satellites in higher spatial resolutions, we can better understand the mass transport and redistribution in the Earth system, e.g., the terrestrial water cycle and sea level variations.

REFERENCES

- A, G., J. Wahr, and S. Zhong (2013), Computations of the viscoelastic response of a 3-d compressible earth to surface loading: an application to glacial isostatic adjustment in antarctica and canada, *Geophysical Journal International*, 192(2), 557–572.
- Ablain, M., A. Cazenave, G. Valladeau, and S. Guinehut (2009), A new assessment of the error budget of global mean sea level rate estimated by satellite altimetry over 1993-2008, *Ocean Science*, 5, 193–201.
- Alsdorf, D., S.-C. Han, P. Bates, and J. Melack (2010), Seasonal water storage on the Amazon floodplain measured from satellites, *Remote Sensing of Environment*, 114(11), 2448–2456.
- Andersen, O. B., S. I. Seneviratne, J. Hinderer, and P. Viterbo (2005), GRACE-derived terrestrial water storage depletion associated with the 2003 European heat wave, *Geophysical Research Letters*, 32(18), L18,405.
- Antonov, J. I., S. Levitus, and T. P. Boyer (2002), Steric sea level variations during 1957-1994: Importance of salinity, *Journal of Geophysical Research: Oceans*, 107(C12), 8013,doi:10.1029/2001JC000,964.
- Argus, D. F., Y. Fu, and F. W. Landerer (2014), Seasonal variation in total water storage in california inferred from gps observations of vertical land motion, *Geophysical Research Letters*, 41(6), 1971–1980.
- Bank, W. (2001), China: Agenda for water sector strategy for north china. vol. 1: Summary report: 141, *Tech. rep.*
- Becker, M., W. Llovel, A. Cazenave, A. Güntner, and J. Crétaux (2010), Recent hydrological behavior of the East African great lakes region inferred from GRACE, satellite altimetry and rainfall observations, *Comptes Rendus Geoscience*, 342(3), 223–233.
- Becker, M., B. Meyssignac, L. Xavier, A. Cazenave, R. Alkama, and B. Decharme (2011), Past terrestrial water storage (1980-2008) in the amazon basin reconstructed from grace and in situ river gauging data, *Hydrology and Earth System Sciences*, 15, 533–546.
- Bettadpur, S. (2007), UTCSR Level-2 gravity field product user handbook, GRACE 327-734, *Tech. rep.*, Center for Space Research, The University of Texas at Austin, Austin.
- Bindoff, N., et al. (2007), Observations: Oceanic climate change and sea level, *Tech. rep.*, Cambridge.

References

- Boening, C., J. Willis, F. Landerer, R. Nerem, and J. Fasullo (2012), The 2011 La Niña: So strong, the oceans fell, *Geophysical Research Letters*, 39, L19,602, doi:10.1029/2012GL053,055.
- Bruinsma, S., J. M. Lemoine, R. Biancale, and N. Vales (2010), CNES/GRGS 10-day gravity field models (release 2) and their evaluation, *Advances in Space Research*, 45(4), 587–601.
- Calafat, F. M., M. Marcos, and D. Gomis (2010), Mass contribution to Mediterranean Sea level variability for the period 1948-2000, *Global and Planetary Change*, 73(3-4), 193–201.
- Cao, G., C. Zheng, B. R. Scanlon, J. Liu, and W. Li (2013), Use of flow modeling to assess sustainability of groundwater resources in the North China Plain, *Water Resources Research*, 49, 159–175.
- Carrère, L., and F. Lyard (2003), Modeling the barotropic response of the global ocean to atmospheric wind and pressure forcing - comparisons with observations, *Geophysical Research Letters*, 30(6), 1275.
- Carter, G. C. (1987), Coherence and time-delay estimation, *Proceedings of the IEEE*, 75(2), 236–255.
- Cazenave, A., and W. Llovel (2010), Contemporary sea level rise, *annual Review of Marine Science*, pp. 145–173.
- Cazenave, A., K. Dominh, S. Guinehut, E. Berthier, W. Llovel, G. Ramillien, M. Ablain, and G. Larnicol (2009), Sea level budget over 2003-2008: A reevaluation from GRACE space gravimetry, satellite altimetry and Argo, *Global and Planetary Change*, 65(1-2), 83–88.
- Chambers, D., and J. Bonin (2012), Evaluation of release-05 grace time-variable gravity coefficients over the ocean, *Ocean Science Discussions*, 9, 2187–2214.
- Chambers, D., J. Wahr, M. Tamisiea, and R. Nerem (2010), Ocean mass from GRACE and glacial isostatic adjustment, *Journal of Geophysical Research*, 115, B11,415, doi:10.1029/2010JB007,530.
- Chambers, D. P. (2006), Evaluation of new grace time-variable gravity data over the ocean, *Geophysical Research Letters*, 33, L17,603, doi:10.1029/2006GL027,296.
- Chambers, D. P., and J. Schroter (2011), Measuring ocean mass variability from satellite gravimetry, *Journal of Geodynamics*, 52(5), 333–343.
- Chambers, D. P., J. Wahr, and R. S. Nerem (2004), Preliminary observations of global ocean mass variations with GRACE, *Geophysical Research Letters*, 31(13), L13,310, doi:10.1029/2004GL020,461.
- Chao, B. F. (1994), The geoid and earth rotation, *Geophysical Interpretations of Geoid*, ed. P. Vanicek and N. Christou, CRC Press, Boca Raton.
- Chao, B. F., and R. S. Gross (1987), Changes in the earths rotation and low-degree gravitational-field induced by earthquakes, *Geophysical Journal of the Royal Astronomical Society*, 91(3), 569–596.

- Chaussard, E., R. Bürgmann, M. Shirzaei, E. J. Fielding, and B. Baker (2014), Predictability of hydraulic head changes and characterization of aquifer-system and fault properties from insar-derived ground deformation, *Journal of Geophysical Research: Solid Earth*, *119*(8), 2014JB011,266.
- Chen, J., C. Wilson, D. Blankenship, and B. Tapley (2009a), Accelerated antarctic ice loss from satellite gravity measurements, *Nature Geoscience*, *2*(12), 859–862.
- Chen, J., C. Wilson, and B. Tapley (2010a), The 2009 exceptional Amazon flood and inter-annual terrestrial water storage change observed by GRACE, *Water Resources Research*, *46*(12), W12,526, doi:10.1029/2010WR009,383.
- Chen, J. L., C. R. Wilson, D. P. Chambers, R. S. Nerem, and B. D. Tapley (1998), Seasonal global water mass budget and mean sea level variations, *Geophysical Research Letters*, *25*(19), 3555–3558.
- Chen, J. L., C. R. Wilson, and K. W. Seo (2006), Optimized smoothing of gravity recovery and climate experiment (grace) time-variable gravity observations, *Journal of Geophysical Research-Solid Earth*, *111*, B06,408, doi:10.1029/2005JB004,064.
- Chen, J. L., C. R. Wilson, B. D. Tapley, and S. Grand (2007a), GRACE detects coseismic and postseismic deformation from the Sumatra-Andaman earthquake, *Geophysical Research Letters*, *34*(13), L13,302.
- Chen, J. L., C. R. Wilson, B. D. Tapley, D. D. Blankenship, and E. R. Ivins (2007b), Patagonia icefield melting observed by gravity recovery and climate experiment (grace), *Geophysical Research Letters*, *34*(22), L22,501, doi: 10.1029/2007GL031,871.
- Chen, J. L., C. R. Wilson, J. S. Famiglietti, and M. Rodell (2007c), Attenuation effect on seasonal basin-scale water storage changes from GRACE time-variable gravity, *Journal of Geodesy*, *81*(4), 237–245.
- Chen, J. L., C. R. Wilson, B. D. Tapley, D. Blankenship, and D. Young (2008), Antarctic regional ice loss rates from GRACE, *Earth and Planetary Science Letters*, *266*(1-2), 140–148.
- Chen, J. L., C. R. Wilson, B. D. Tapley, Z. L. Yang, and G. Y. Niu (2009b), 2005 drought event in the Amazon River basin as measured by GRACE and estimated by climate models, *Journal of Geophysical Research: Solid Earth*, *114*, B05,404, doi:10.1029/2008JB006,056.
- Chen, J. L., C. R. Wilson, B. D. Tapley, L. Longuevergne, Z. L. Yang, and B. R. Scanlon (2010b), Recent la plata basin drought conditions observed by satellite gravimetry, *Journal of Geophysical Research: Atmospheres*, *115*(D22), D22,108.
- Chen, Y., I. Velicogna, J. S. Famiglietti, and J. T. Randerson (2013), Satellite observations of terrestrial water storage provide early warning information about drought and fire season severity in the amazon, *Journal of Geophysical Research: Biogeosciences*, *118*, doi:10.1002/jgrg.20,046.
- Cheng, M. K., and B. D. Tapley (2004), Variations in the earth's oblateness during the past 28 years, *Journal of Geophysical Research-Solid Earth*, *109*, B09,402, doi:10.1029/2004JB003,028.

References

- Cheng, X. H., and Y. Q. Qi (2007), Trends of sea level variations in the South China Sea from merged altimetry data, *Global and Planetary Change*, 57(3-4), 371–382.
- Church, J., et al. (2013), Sea level change, in *Climate Change 2013: The Physical Science Basis. Contribution of Working Group I to the Fifth Assessment Report of the Intergovernmental Panel on Climate Change*, edited by T. Stocker, D. Qin, G.-K. Plattner, M. Tignor, S. Allen, J. Boschung, A. Nauels, Y. Xia, V. Bex, and P. Midgley, chap. 13, p. 1137–1216, Cambridge University Press, Cambridge, United Kingdom and New York, NY, USA.
- Church, J. A., and N. J. White (2006), A 20th century acceleration in global sea-level rise, *Geophysical Research Letters*, 33(1), L01,602.
- Cromwell, D., and D. A. Smeed (1998), Altimetric observations of sea level cycles near the strait of bab al mandab, *International Journal of Remote Sensing*, 19(8), 1561–1578.
- Crowley, J. W., J. X. Mitrovica, R. C. Bailey, M. E. Tamisiea, and J. L. Davis (2006), Land water storage within the congo basin inferred from grace satellite gravity data, *Geophysical Research Letters*, 33(19), L19,402.
- Crétaux, J. F., et al. (2011), Sols: A lake database to monitor in the near real time water level and storage variations from remote sensing data, *Advances in Space Research*, 47(9), 1497–1507.
- Dai, Y. J., and Q. C. Zeng (1997), A land surface model (iap94) for climate studies part i: Formulation and validation in off-line experiments, *Advances in Atmospheric Sciences*, 14(4), 433–460, doi:10.1007/s00376-997-0063-4.
- Davis, J. L., M. E. Tamisiea, P. Elosegui, J. X. Mitrovica, and E. M. Hill (2008), A statistical filtering approach for Gravity Recovery and Climate Experiment (GRACE) gravity data, *Journal of Geophysical Research-Solid Earth*, 113, B04,410, doi:10.1029/2007JB005,043.
- Department of Water Resources in the Hebei Province (DWRHP) (2010), Groundwater Bulletin of Hebei Plain, *Tech. rep.*, Hebei.
- Duan, X. J., J. Y. Guo, C. K. Shum, and W. van der Wal (2009), On the postprocessing removal of correlated errors in GRACE temporal gravity field solutions, *Journal of Geodesy*, 83(11), 1095–1106.
- Ducet, N., P. Le Traon, and G. Reverdin (2000), Global high resolution mapping of ocean circulation from TOPEX/Poseidon and ERS-1 and -2, *Journal of Geophysical Research: Oceans*, 105(C8), 19,477–19,498.
- Dziewonski, A. M., and D. L. Anderson (1981), Preliminary reference earth models, *Physics of the Earth and Planetary Interiors*, 25(4), 297–356.
- Döll, P., F. Kaspar, and B. Lehner (2003), A global hydrological model for deriving water availability indicators: model tuning and validation, *Journal of Hydrology*, 270(1), 105–134.
- Döll, P., H. Müller Schmied, C. Schuh, F. T. Portmann, and A. Eicker (2014), Global-scale assessment of groundwater depletion and related groundwater abstractions: Combining hydrological modeling with information from well observations and grace satellites, *Water Resources Research*, 50(7), 5698–5720.

- Ek, M., K. Mitchell, Y. Lin, E. Rogers, P. Grunmann, V. Koren, G. Gayno, and J. Tarpley (2003), Implementation of Noah land surface model advances in the National Centers for Environmental Prediction operational mesoscale Eta model, *Journal of Geophysical Research*, 108(D22), 8851, doi:10.1029/2002JD003,296.
- Famiglietti, J., M. Lo, S. Ho, J. Bethune, K. Anderson, T. Syed, S. Swenson, C. de Linage, and M. Rodell (2011), Satellites measure recent rates of groundwater depletion in California's Central Valley, *Geophysical Research Letters*, 38, L03,403, doi:10.1029/2010GL046,442.
- Famiglietti, J. S. (2004), Remote sensing of terrestrial water storage, soil moisture and surface waters, in *The State of the Planet: Frontiers and Challenges in Geophysics*, pp. 197–207, American Geophysical Union.
- Fan, Y., and H. van den Dool (2004), Climate prediction center global monthly soil moisture data set at 0.5° resolution for 1948 to present, *Journal of Geophysical Research*, 109, D10,102, doi:10.1029/2003JD004,345.
- Farrell, W. (1972), Deformation of the earth by surface loads, *Reviews of Geophysics*, 10(3), 761–797.
- Fasullo, J. T., C. Boening, F. W. Landerer, and R. S. Nerem (2013), Australia's unique influence on global sea level in 2010-2011, *Geophysical Research Letters*, 40(16), 4368–4373.
- Feng, W., J. M. Lemoine, M. Zhong, and H. T. Hsu (2012), Terrestrial water storage changes in the amazon basin measured by grace during 2002-2010, *Chinese Journal of Geophysics*, 55(3), 814–821.
- Feng, W., J. M. Lemoine, M. Zhong, and H. Hsu (2014), Mass-induced sea level variations in the red sea from grace, steric-corrected altimetry, in situ bottom pressure records, and hydrographic observations, *Journal of Geodynamics*, 78(0), 1–7, doi:http://dx.doi.org/10.1016/j.jog.2014.04.008.
- Fenoglio-Marc, L., J. Kusche, and M. Becker (2006), Mass variation in the mediterranean sea from grace and its validation by altimetry, steric and hydrologic fields, *Geophysical Research Letters*, 33, L19,606, doi:10.1029/2006GL026,851.
- Forootan, E., R. Rietbroek, J. Kusche, M. A. Sharifi, J. L. Awange, M. Schmidt, P. Omondi, and J. Famiglietti (2014), Separation of large scale water storage patterns over iran using grace, altimetry and hydrological data, *Remote Sensing of Environment*, 140, 580–595.
- Foster, S., and P. Chilton (2003), Groundwater: the processes and global significance of aquifer degradation, *Philosophical Transactions of the Royal Society of London. Series B: Biological Sciences*, 358(1440), 1957.
- Foster, S., H. Garduno, R. Evans, D. Olson, Y. Tian, W. Zhang, and Z. Han (2004), Quaternary aquifer of the North China Plain—assessing and achieving groundwater resource sustainability, *Hydrogeology Journal*, 12(1), 81–93.
- Frappart, F., F. Papa, A. Guntner, W. Susanna, G. Ramillien, C. Prigent, B. Rossow, and M. Bonnet (2010), Interannual variations of the terrestrial water storage in the Lower Ob'Basin from a multisatellite approach, *Hydrology and Earth System Sciences*, 14(12), 2443–2453.

References

- Frappart, F., F. Papa, J. da Silva, G. Ramillien, C. Prigent, F. Seyler, and S. Calmant (2012), Surface freshwater storage and dynamics in the amazon basin during the 2005 exceptional drought, *Environmental Research Letters*, 7(4), 044,010.
- Fu, L.-L., and A. Cazenave (2001), *Satellite Altimetry and Earth Sciences*, Academic Pr.
- Fukumori, I. (2002), A partitioned kalman filter and smoother, *Monthly Weather Review*, 130(5), 1370–1383.
- García, D., B. Chao, J. Del Río, I. Vigo, and J. García-Lafuente (2006), On the steric and mass-induced contributions to the annual sea level variations in the Mediterranean Sea, *Journal of Geophysical Research-Oceans*, 111(C9), C09,030, doi:10.1029/2005JC002,956.
- Gill, A. E., and P. P. Niiler (1973), The theory of seasonal variability in ocean, *Deep-Sea Research*, 20(2), 141–177.
- Gregory, J., J. Lowe, and S. Tett (2006), Simulated global-mean sea level changes over the last half-millennium, *Journal of Climate*, 19(18), 4576–4591.
- Grinsted, A., J. Moore, and S. Jevrejeva (2010), Reconstructing sea level from paleo and projected temperatures 200 to 2100 ad, *Climate Dynamics*, 34(4), 461–472.
- Guinehut, S., P. Le Traon, G. Larnicol, and S. Philipps (2004), Combining argo and remote-sensing data to estimate the ocean three-dimensional temperature fields' first approach based on simulated observations, *Journal of Marine Systems*, 46(1-4), 85–98.
- Gunter, B., T. Urban, R. Riva, M. Helsen, R. Harpold, S. Poole, P. Nagel, B. Schutz, and B. Tapley (2009), A comparison of coincident GRACE and ICESat data over Antarctica, *Journal of Geodesy*, 83(11), 1051–1060.
- Hadfield, R. E., N. C. Wells, S. A. Josey, and J. J. M. Hirschi (2007), On the accuracy of North Atlantic temperature and heat storage fields from Argo, *Journal of Geophysical Research: Oceans*, 112(C1), C01,009.
- Han, S. C., C. K. Shum, C. Jekeli, C. Y. Kuo, C. Wilson, and K. W. Seo (2005), Non-isotropic filtering of GRACE temporal gravity for geophysical signal enhancement, *Geophysical Journal International*, 163(1), 18–25.
- Han, S. C., C. K. Shum, M. Bevis, C. Ji, and C. Y. Kuo (2006), Crustal dilatation observed by GRACE after the 2004 Sumatra-Andaman earthquake, *Science*, 313(5787), 658–662.
- Han, S. M., Y. H. Yang, Y. P. Lei, C. Y. Tang, and J. P. Moiwo (2008), Seasonal groundwater storage anomaly and vadose zone soil moisture as indicators of precipitation recharge in the piedmont region of taihang mountain, north china plain, *Hydrology Research*, 39(5-6), 479–495.
- Han, Z. (2003), Groundwater resources protection and aquifer recovery in china, *Environmental Geology*, 44(1), 106–111.
- Ho, C. R., Q. N. Zheng, Y. S. Soong, N. J. Kuo, and J. H. Hu (2000), Seasonal variability of sea surface height in the South China Sea observed with TOPEX/Poseidon altimeter data, *Journal of Geophysical Research-Oceans*, 105(C6), 13,981–13,990.

- Holgate, S., S. Jevrejeva, P. Woodworth, and S. Brewer (2007), Comment on " a semi-empirical approach to projecting future sea-level rise", *Science*, 317(5846), 1866–1866.
- Hu, X. G., J. L. Chen, Y. H. Zhou, C. Huang, and X. H. Liao (2006), Seasonal water storage change of the yangtze river basin detected by grace, *Science in China Series D*, 49(5), 483–491.
- Ichikawa, H., and R. C. Beardsley (2002), The current system in the yellow and east china seas, *Journal of Oceanography*, 58(1), 77–92.
- Ishii, M., and M. Kimoto (2009), Reevaluation of historical ocean heat content variations with time-varying XBT and MBT depth bias corrections, *Journal of Oceanography*, 65(3), 287–299.
- Ishii, M., M. Kimoto, K. Sakamoto, and S. I. Iwasaki (2006), Steric sea level changes estimated from historical ocean subsurface temperature and salinity analyses, *Journal of Oceanography*, 62(2), 155–170.
- Jacob, T., J. Wahr, W. T. Pfeffer, and S. Swenson (2012), Recent contributions of glaciers and ice caps to sea level rise, *Nature*, 482(7386), 514–518.
- Jayne, S. R., et al. (2009), The kuroshio extension and its recirculation gyres, *Deep Sea Research Part I: Oceanographic Research Papers*, 56(12), 2088–2099.
- Jekeli, C. (1981), Alternative methods to smooth the Earth's gravity field, Rep. 327, Dep. of Geod, *Tech. rep.*, Department of Geodetic Science and Surveying, The Ohio State University, Columbus.
- Joodaki, G., J. Wahr, and S. Swenson (2014), Estimating the human contribution to groundwater depletion in the middle east, from grace data, land surface models, and well observations, *Water Resources Research*, 50(3), 2679–2692.
- Kendy, E., D. J. Molden, T. S. Steenhuis, C. Liu, and J. Wang (2003), *Policies drain the North China Plain: Agricultural policy and groundwater depletion in Luancheng County, 1949-2000*, vol. 71, Int. Water Manage. Inst.
- Kendy, E., Y. Zhang, C. Liu, J. Wang, and T. Steenhuis (2004), Groundwater recharge from irrigated cropland in the north china plain: case study of luancheng county, hebei province, 1949–2000, *Hydrological Processes*, 18(12), 2289–2302.
- Kerr, Y. H., P. Waldteufel, J. P. Wigneron, J. Martinuzzi, J. Font, and M. Berger (2001), Soil moisture retrieval from space: the soil moisture and ocean salinity (smos) mission, *Geoscience and Remote Sensing, IEEE Transactions on*, 39(8), 1729–1735.
- King, M., R. Bingham, P. Moore, P. Whitehouse, M. Bentley, and G. Milne (2012), Lower satellite-gravimetry estimates of antarctic sea-level contribution, *Nature*, 491(7425), 586–589.
- Klees, R., E. A. Zapreeva, H. C. Winsemius, and H. H. G. Savenije (2007), The bias in GRACE estimates of continental water storage variations, *Hydrology and Earth System Sciences Discussions*, 11, 1227–1241.

References

- Konikow, L. (2011), Contribution of global groundwater depletion since 1900 to sea-level rise, *Geophysical Research Letters*, 38(17), L17,401, doi:10.1029/2011GL048,604.
- Koster, R., and M. Suarez (1992), Modeling the land surface boundary in climate models as a composite of independent vegetation stands, *Journal of Geophysical Research*, 97(D3), 2697–2715.
- Kuo, C. (2006), Determination and characterization of 20th century global sea level rise, *Tech. Rep. No. 478*, Ohio State University.
- Kuo, C. Y., C. K. Shum, J. Y. Guo, Y. C. Yi, A. Braun, I. Fukumori, K. Matsumoto, T. Sato, and K. Shibuya (2008), Southern Ocean mass variation studies using GRACE and satellite altimetry, *Earth Planets and Space*, 60(5), 477–485.
- Kusche, J. (2007), Approximate decorrelation and non-isotropic smoothing of time-variable GRACE-type gravity field models, *Journal of Geodesy*, 81(11), 733–749.
- Kusche, J., and E. J. O. Schrama (2005), Surface mass redistribution inversion from global GPS deformation and Gravity Recovery and Climate Experiment (GRACE) gravity data, *Journal of Geophysical Research: Solid Earth*, 110(B9), B09,409.
- Lambeck, K., and S. M. Nakiboglu (1984), Recent global changes in sealevel, *Geophysical Research Letters*, 11(10), 959–961.
- Lambeck, K., T. Esat, and E. Potter (2002), Links between climate and sea levels for the past three million years, *Nature*, 419(6903), 199–206.
- Lee, T., I. Fukumori, D. Menemenlis, Z. Xing, and L. Fu (2002), Effects of the Indonesian throughflow on the Pacific and Indian Oceans, *Journal of Physical Oceanography*, 32(5), 1404–1429.
- Lemoine, J. M., S. Bruinsma, S. Loyer, R. Biancale, J. C. Marty, F. Perosanz, and G. Balmino (2007), Temporal gravity field models inferred from GRACE data, *Advances in Space Research*, 39(10), 1620–1629.
- Leuliette, E., and R. Scharroo (2010), Integrating Jason-2 into a multiple-altimeter climate data record, *Marine Geodesy*, 33(S1), 504–517.
- Leuliette, E., and J. Willis (2011), Balancing the sea level budget, *Oceanography*, 24(2), 122–129.
- Leuliette, E. W., and L. Miller (2009), Closing the sea level rise budget with altimetry, argo, and grace, *Geophysical Research Letters*, 36(4), L04,608.
- Levitus, S., J. Antonov, and T. Boyer (2005), Warming of the world ocean, 1955–2003, *Geophysical Research Letters*, 32(2), L02,604, doi:10.1029/2004GL021,592.
- Levitus, S., J. I. Antonov, T. P. Boyer, R. A. Locarnini, H. E. Garcia, and A. V. Mishonov (2009), Global ocean heat content 1955–2008 in light of recently revealed instrumentation problems, *Geophysical Research Letters*, 36, 5.
- Li, L., J. D. Xu, and R. S. Cai (2002), Trends of sea level rise in the South China Sea during the 1990s: An altimetry result, *Chinese Science Bulletin*, 47(7), 582–585.

- Liang, X., D. Lettenmaier, E. Wood, and S. Burges (1994), A simple hydrologically based model of land surface water and energy fluxes for general circulation models, *Journal of Geophysical Research*, 99(D7), 14,415–14,428.
- Liu, C., X. Zhang, and Y. Zhang (2002), Determination of daily evaporation and evapotranspiration of winter wheat and maize by large-scale weighing lysimeter and micro-lysimeter, *Agricultural and Forest Meteorology*, 111(2), 109–120.
- Liu, C. M., J. J. Yu, and E. Kendy (2001), Groundwater exploitation and its impact on the environment in the north china plain, *Water International*, 26(2), 265–272.
- Lombard, A., D. Garcia, G. Ramillien, A. Cazenave, R. Biancale, J. M. Lemome, F. Flechtner, R. Schmidt, and M. Ishii (2007), Estimation of steric sea level variations from combined GRACE and Jason-1 data, *Earth and Planetary Science Letters*, 254(1-2), 194–202.
- Long, D., B. R. Scanlon, L. Longuevergne, A. Y. Sun, D. N. Fernando, and H. Save (2013), Grace satellite monitoring of large depletion in water storage in response to the 2011 drought in texas, *Geophysical Research Letters*, 40(13), 3395–3401.
- Longuevergne, L., B. Scanlon, and C. Wilson (2010), Grace hydrological estimates for small basins: Evaluating processing approaches on the high plains aquifer, usa, *Water Resour. Res.*, 46, W11,517, doi:10.1029/2009WR008,564.
- Lyman, J. M., J. K. Willis, and G. C. Johnson (2006), Recent cooling of the upper ocean, *Geophysical Research Letters*, 33(18), L18,604.
- Matsuo, K., and K. Heki (2010), Time-variable ice loss in asian high mountains from satellite gravimetry, *Earth and Planetary Science Letters*, 290(1-2), 30–36.
- Meysignac, B., and A. Cazenave (2012), Sea level: A review of present-day and recent-past changes and variability, *Journal of Geodynamics*, 58(0), 96–109.
- Ministry of Land and Resources of China (MLR) (2009), Groundwater regime in major cities of China, *Tech. rep.*, Beijing.
- Ministry of Water Resources of China (MWR) (2010), Bulletin of Groundwater in the North China Plain, *Tech. rep.*, Beijing.
- Minster, J. F., A. Cazenave, Y. V. Serafini, F. Mercier, M. C. Gennero, and P. Rogel (1999), Annual cycle in mean sea level from Topex-Poseidon and ERS-1: inference on the global hydrological cycle, *Global and Planetary Change*, 20(1), 57–66.
- Mitchum, G. T., R. S. Nerem, M. A. Merrifield, and W. R. Gehrels (2010), Modern sea-level-change estimates, in *Understanding Sea-Level Rise and Variability*, pp. 122–142, Wiley-Blackwell.
- Moiwo, J. P., Y. H. Yang, H. L. Li, S. M. Han, and Y. K. Hu (2009), Comparison of GRACE with in situ hydrological measurement data shows storage depletion in Hai River basin, Northern China, *Water Sa*, 35(5), 663–670.
- Munk, W. (2003), Ocean freshening, sea level rising, *Science*, 300(5628), 2041–2043.

References

- Murray, S. P., and W. Johns (1997), Direct observations of seasonal exchange through the bab el mandab strait, *Geophysical Research Letters*, *24*(21), 2557–2560.
- Nerem, R., D. Chambers, C. Choe, and G. Mitchum (2010), Estimating mean sea level change from the TOPEX and Jason altimeter missions, *Marine Geodesy*, *33*(S1), 435–446.
- Oleson, K. W., et al. (2013), Technical Description of version 4.5 of the Community Land Model (CLM), *Tech. rep.*, National Center for Atmospheric Research, Boulder.
- Panet, I., V. Mikhailov, M. Diament, F. Pollitz, G. King, O. de Viron, M. Holschneider, R. Biancale, and J. M. Lemoine (2007), Coseismic and post-seismic signatures of the Sumatra 2004 December and 2005 March earthquakes in GRACE satellite gravity, *Geophysical Journal International*, *171*(1), 177–190.
- Panet, I., et al. (2013), Earth system mass transport mission (e. motion): A concept for future earth gravity field measurements from space, *Surveys in Geophysics*, *34*(2), 141–163.
- Pattullo, J., W. Munk, R. Revelle, and E. Strong (1955), The seasonal oscillation in sea level, *Journal of Marine Research*, *14*(1), 88–156.
- Patzert, W. (1974), Wind-induced reversal in Red Sea circulation, *Deep-Sea Research*, *21*, 109–121.
- Paulson, A., S. J. Zhong, and J. Wahr (2007), Inference of mantle viscosity from grace and relative sea level data, *Geophysical Journal International*, *171*, 497–508, doi: 10.1111/j.1365–246X.2007.03,556.x.
- Peltier, W. R. (1986), Deglaciation-induced vertical motion of the north american continent and transient lower mantle rheology, *Journal of Geophysical Research: Solid Earth*, *91*(B9), 9099–9123.
- Peltier, W. R. (2004), Global glacial isostasy and the surface of the ice-age earth: The ice-5G (VM2) model and grace, *Annual Review of Earth and Planetary Sciences*, *32*, 111–149.
- Peltier, W. R. (2009), Closure of the budget of global sea level rise over the grace era: the importance and magnitudes of the required corrections for global glacial isostatic adjustment, *Quaternary Science Reviews*, *28*(17-18), 1658–1674.
- Ponte, R. M. (1993), Variability in a homogeneous global ocean forced by barometric pressure, *Dynamics of Atmospheres and Oceans*, *18*(3-4), 209–234.
- Ponte, R. M. (1999), A preliminary model study of the large-scale seasonal cycle in bottom pressure over the global ocean, *Journal of Geophysical Research: Oceans*, *104*(C1), 1289–1300.
- Qu, T., H. Mitsudera, and T. Yamagata (2000), Intrusion of the North Pacific waters into the South China Sea, *Journal of Geophysical Research: Oceans*, *105*(C3), 6415–6424.
- Rahmstorf, S. (2007), A semi-empirical approach to projecting future sea-level rise, *Science*, *315*(5810), 368–370.

- Ramillien, G., A. Lombard, A. Cazenave, E. R. Ivins, M. Llubes, F. Remy, and R. Biancale (2006), Interannual variations of the mass balance of the Antarctica and Greenland ice sheets from GRACE, *Global and Planetary Change*, 53(3), 198–208.
- Rodell, M., and J. Famiglietti (2002), The potential for satellite-based monitoring of groundwater storage changes using GRACE: the High Plains aquifer, Central US, *Journal of Hydrology*, 263(1-4), 245–256.
- Rodell, M., et al. (2004), The global land data assimilation system, *Bulletin of the American Meteorological Society*, 85(3), 381–394.
- Rodell, M., J. L. Chen, H. Kato, J. S. Famiglietti, J. Nigro, and C. R. Wilson (2007), Estimating groundwater storage changes in the Mississippi River basin (USA) using GRACE, *Hydrogeology Journal*, 15(1), 159–166.
- Rodell, M., I. Velicogna, and J. S. Famiglietti (2009), Satellite-based estimates of groundwater depletion in India, *Nature*, 460(7258), 999–1002.
- Roemmich, D., and W. B. Owens (2000), The Argo Project: Global ocean observations for understanding and prediction of climate variability, *Oceanography*, 13(2), 45–50.
- Sakura, Y., C. Tang, R. Yoshioka, and H. Ishibashi (2003), *Intensive Use of Groundwater in Some Areas of China and Japan*, Intensive Use of Groundwater: Challenges and Opportunities, AA Balkema, Netherland, Rotterdam, Netherland.
- Sasgen, I., Z. Martinec, and K. Fleming (2007), Wiener optimal combination and evaluation of the Gravity Recovery and Climate Experiment (GRACE) gravity fields over Antarctica, *Journal of Geophysical Research: Solid Earth*, 112, B04,401, doi:10.1029/2006JB004,605.
- Scanlon, B., I. Jolly, M. Sophocleous, and L. Zhang (2007), Global impacts of conversions from natural to agricultural ecosystems on water resources: Quantity versus quality, *Water Resources Research*, 43, W03,437, doi:10.1029/2006WR005,486.
- Scanlon, B. R., L. Longuevergne, and D. Long (2012), Ground referencing GRACE satellite estimates of groundwater storage changes in the California Central Valley, US, *Water Resources Research*, p. doi:10.1029/2011WR011312.
- Schmidt, M., S. C. Han, J. Kusche, L. Sanchez, and C. K. Shum (2006), Regional high-resolution spatiotemporal gravity modeling from GRACE data using spherical wavelets, *Geophysical Research Letters*, 33(8), L08,403.
- Schmith, T., S. Johansen, and P. Thejll (2007), Comment on "a semi-empirical approach to projecting future sea-level rise", *Science*, 317(5846), 1866.
- Schrama, E. J. O., B. Wouters, and R. Rietbroek (2014), A mascon approach to assess ice sheet and glacier mass balances and their uncertainties from grace data, *Journal of Geophysical Research: Solid Earth*, 119(7), 6048–6066.
- Schutz, B. E., H. J. Zwally, C. A. Shuman, D. Hancock, and J. P. DiMarzio (2005), Overview of the ICESat Mission, *Geophysical Research Letters*, 32(21), L21S01.

References

- Shah, T., D. Molden, S. R., and S. D. (2000), *The global groundwater situation: Overview of opportunities and challenges*, Int. Water Manage. Inst., Colombo, Sri Lanka.
- Sheffield, J., C. R. Ferguson, T. J. Troy, E. F. Wood, and M. F. McCabe (2009), Closing the terrestrial water budget from satellite remote sensing, *Geophysical Research Letters*, *36*(7), L07,403.
- Shepherd, A., et al. (2012), A reconciled estimate of ice-sheet mass balance, *Science*, *338*(6111), 1183–1189.
- Shum, C. K., C.-Y. Kuo, and J.-Y. Guo (2008), Role of antarctic ice mass balance in present-day sea-level change, *Polar Science*, *2*(2), 149–161.
- Siddall, M., D. Smeed, S. Matthiesen, and E. Rohling (2002), Modelling the seasonal cycle of the exchange flow in bab el mandab (red sea), *Deep Sea Research Part I: Oceanographic Research Papers*, *49*(9), 1551–1569.
- Siddall, M., D. A. Smeed, C. Hemleben, E. J. Rohling, I. Schmelzer, and W. R. Peltier (2004), Understanding the Red Sea response to sea level, *Earth and Planetary Science Letters*, *225*(3-4), 421–434.
- Siebert, S., J. Burke, J. M. Faures, K. Frenken, J. Hoogeveen, P. Doll, and F. T. Portmann (2010), Groundwater use for irrigation - a global inventory, *Hydrology and Earth System Sciences*, *14*(10), 1863–1880.
- Smeed, D. (1997), Seasonal variation of the flow in the strait of bah al mandab, *Oceanologica Acta*, *20*(6), 773–781.
- Sofianos, S., and W. Johns (2002), An oceanic general circulation model (ogcm) investigation of the red sea circulation, 1. exchange between the red sea and the indian ocean, *Journal of Geophysical Research*, *107*(C11), 3196.
- Sofianos, S. S., and W. E. Johns (2001), Wind induced sea level variability in the Red Sea, *Geophysical Research Letters*, *28*(16), 3175–3178.
- Sofianos, S. S., W. E. Johns, and S. P. Murray (2002), Heat and freshwater budgets in the Red Sea from direct observations at Bab el Mandeb, *Deep-Sea Research Part II-Topical Studies in Oceanography*, *49*(7-8), 1323–1340.
- Strassberg, G., B. R. Scanlon, and M. Rodell (2007), Comparison of seasonal terrestrial water storage variations from GRACE with groundwater-level measurements from the High Plains Aquifer (USA), *Geophysical Research Letters*, *34*, L14,402, doi:10.1029/2007GL030,139.
- Strassberg, G., B. R. Scanlon, and D. Chambers (2009), Evaluation of groundwater storage monitoring with the GRACE satellite: Case study of the High Plains aquifer, central United States, *Water Resources Research*, *45*, W05,410, doi:10.1029/2008WR006,892.
- Su, X., J. Ping, and Q. Ye (2011), Terrestrial water variations in the north china plain revealed by the grace mission, *Science China Earth Sciences*, *54*(12), 1965–1970, doi: 10.1007/s11430-011-4280-4.

- Swenson, S., and J. Wahr (2002), Methods for inferring regional surface-mass anomalies from Gravity Recovery and Climate Experiment (GRACE) measurements of time-variable gravity, *Journal of Geophysical Research: Solid Earth*, 107(B9), 2193, doi:10.1029/2001JB000,576.
- Swenson, S., and J. Wahr (2006), Post-processing removal of correlated errors in GRACE data, *Geophysical Research Letters*, 33(8), L08,402, doi:10.1029/2005GL025,285.
- Swenson, S., and J. Wahr (2007), Multi-sensor analysis of water storage variations of the Caspian Sea, *Geophysical Research Letters*, 34, L16,401, doi:10.1029/2007GL030,733.
- Swenson, S., P. Yeh, J. Wahr, and J. Famiglietti (2006), A comparison of terrestrial water storage variations from GRACE with in situ measurements from Illinois, *Geophysical Research Letters*, 33(16), 16,401.
- Swenson, S., J. Famiglietti, J. Basara, and J. Wahr (2008a), Estimating profile soil moisture and groundwater variations using GRACE and Oklahoma Mesonet soil moisture data, *Water Resources Research*, 44(1), W01,413.
- Swenson, S., D. Chambers, and J. Wahr (2008b), Estimating geocenter variations from a combination of GRACE and ocean model output, *Journal of Geophysical Research: Solid Earth*, 113(B8), B08,410, doi:10.1029/2007JB005,338.
- Taboada, F., and R. Anadon (2010), Critique of the methods used to project global sea-level rise from global temperature, *Proceedings of the National Academy of Sciences*, 107(29), E116–E117.
- Tamanyu, S., H. Muraoka, and T. Ishii (2009), Geological interpretation of groundwater level lowering in the north china plain, *Bulletin of the Geological Survey of Japan*, 60(1/2), 105–115.
- Tapley, B. D., S. Bettadpur, J. C. Ries, P. F. Thompson, and M. M. Watkins (2004), GRACE measurements of mass variability in the Earth system, *Science*, 305(5683), 503–505.
- Tiwari, V. M., J. Wahr, and S. Swenson (2009), Dwindling groundwater resources in northern India, from satellite gravity observations, *Geophysical Research Letters*, 36, L18,401, doi:10.1029/2009GL039,401.
- Tomczak, M., and J. Godfrey (1994), *Regional Oceanography: An Introduction*, Pergamon, New York.
- Tregoning, P., K. Lambeck, and G. Ramillien (2008), GRACE estimates of sea surface height anomalies in the Gulf of Carpentaria, Australia, *Earth and Planetary Science Letters*, 271(1-4), 241–244.
- Velicogna, I., and J. Wahr (2006a), Acceleration of Greenland ice mass loss in spring 2004, *Nature*, 443(7109), 329–331.
- Velicogna, I., and J. Wahr (2006b), Measurements of time-variable gravity show mass loss in Antarctica, *Science*, 311(5768), 1754–1756.

References

- Vermeer, M., and S. Rahmstorf (2009), Global sea level linked to global temperature, *Proceedings of the National Academy of Sciences*, 106(51), 21,527–21,532.
- Vermeer, M., and S. Rahmstorf (2010), Reply to Taboada and Anadón: Critique of sea-level rise study invalid, *Proceedings of the National Academy of Sciences*, 107(29), E118.
- Voss, K. A., J. S. Famiglietti, M. Lo, C. de Linage, M. Rodell, and S. C. Swenson (2013), Groundwater depletion in the Middle East from GRACE with implications for transboundary water management in the Tigris-Euphrates-Western Iran region, *Water Resources Research*, 49(2), 904–914.
- Wada, Y., L. P. H. van Beek, C. M. van Kempen, J. W. T. M. Reckman, S. Vasak, and M. F. P. Bierkens (2010), Global depletion of groundwater resources, *Geophysical Research Letters*, 37, L20,402, doi:10.1029/2010GL044,571.
- Wada, Y., L. P. H. van Beek, F. C. Sperna Weiland, B. F. Chao, Y.-H. Wu, and M. F. P. Bierkens (2012), Past and future contribution of global groundwater depletion to sea-level rise, *Geophysical Research Letters*, 39(9), L09,402.
- Wahr, J., M. Molenaar, and F. Bryan (1998), Time variability of the Earth's gravity field: Hydrological and oceanic effects and their possible detection using GRACE, *Journal of Geophysical Research-Solid Earth*, 103(B12), 30,205–30,229.
- Wahr, J., S. Swenson, V. Zlotnicki, and I. Velicogna (2004), Time-variable gravity from GRACE: First results, *Geophysical Research Letters*, 31(11), L11,501, doi:10.1029/2004GL019,779.
- Wahr, J., S. Swenson, and I. Velicogna (2006), Accuracy of GRACE mass estimates, *Geophysical Research Letters*, 33(6), L06,401, doi:10.1029/2005GL025,305.
- Wahr, J., D. A. Smeed, E. Leuliette, and S. Swenson (2014), Seasonal variability of the red sea, from satellite gravity, radar altimetry, and in situ observations, *Journal of Geophysical Research: Oceans*, 119(8), 5091–5104.
- Wakata, Y. (2009), Seasonal variability of the sea surface height in the East China Sea along the China coast: A model study, *Journal of Oceanography*, 65(2), 281–286.
- Wang, H., L. Jia, H. Steffen, P. Wu, L. Jiang, H. Hsu, L. Xiang, Z. Wang, and B. Hu (2013), Increased water storage in North America and Scandinavia from GRACE gravity data, *Nature Geoscience*, 6(1), 38–42.
- Wang, J., J. Huang, A. Blanke, Q. Huang, and S. Rozelle (2007), The development, challenges and management of groundwater in rural china, in *Groundwater in Developing World Agriculture: Past, Present and Options for a Sustainable Future*, edited by M. Giordano and T. Shah, pp. 37–62, International Water Manage Institute, Colombo, Sri Lanka.
- Wang, X., C. de Linage, J. Famiglietti, and C. S. Zender (2011), Gravity Recovery and Climate Experiment (GRACE) detection of water storage changes in the Three Gorges Reservoir of China and comparison with in situ measurements, *Water Resources Research*, 47(12), W12,502.

- Welch, P. D. (1967), The use of fast fourier transform for the estimation of power spectra: A method based on time averaging over short, modified periodograms, *Audio and Electroacoustics, IEEE Transactions on*, 15(2), 70–73.
- Williams, S. D. P., P. Moore, M. A. King, and P. L. Whitehouse (2014), Revisiting grace antarctic ice mass trends and accelerations considering autocorrelation, *Earth and Planetary Science Letters*, 385(0), 12–21.
- Willis, J., J. Lyman, G. Johnson, and J. Gilson (2007), Correction to " recent cooling of the upper ocean", *Geophysical Research Letters*, 34(16), 16,601.
- Willis, J. K., D. P. Chambers, and R. S. Nerem (2008), Assessing the globally averaged sea level budget on seasonal to interannual timescales, *Journal of Geophysical Research-Oceans*, 113(C6), C06,015, doi:10.1029/2007JC004,517.
- Willis, J. K., J. M. Lyman, G. C. Johnson, and J. Gilson (2009), In situ data biases and recent ocean heat content variability, *Journal of Atmospheric and Oceanic Technology*, 26(4), 846–852.
- Willis, J. K., D. P. Chambers, C. Y. Kuo, and C. K. Shum (2010), Global sea level rise: Recent progress and challenges for the decade to come, *Oceanography*, 23(4), 26–35.
- Wouters, B., and D. Chambers (2010), Analysis of seasonal ocean bottom pressure variability in the Gulf of Thailand from GRACE, *Global and Planetary Change*, 74(2), 76–81.
- Wu, X., M. B. Hefflin, E. R. Ivins, D. F. Argus, and F. H. Webb (2003), Large-scale global surface mass variations inferred from gps measurements of load-induced deformation, *Geophysical Research Letters*, 30(14), 1742.
- Xavier, L., M. Becker, A. Cazenave, L. Longuevergne, W. Llovel, and O. C. R. Filho (2010), Interannual variability in water storage over 2003-2008 in the Amazon Basin from GRACE space gravimetry, in situ river level and precipitation data, *Remote Sensing of Environment*, 114(8), 1629–1637.
- Xie, S.-P., Q. Xie, D. Wang, and W. T. Liu (2003), Summer upwelling in the south china sea and its role in regional climate variations, *Journal of Geophysical Research: Oceans*, 108(C8), 3261.
- Yang, H., and A. Zehnder (2001), China's regional water scarcity and implications for grain supply and trade, *Environment and Planning A*, 33(1), 79–96.
- Yang, Y., M. Watanabe, X. Zhang, X. Hao, and J. Zhang (2006), Estimation of groundwater use by crop production simulated by dssat-wheat and dssat-maize models in the piedmont region of the north china plain, *Hydrological Processes*, 20(13), 2787–2802, doi:10.1002/hyp.6071.
- Yang, Y., Y. Yang, J. Moiwo, and Y. Hu (2010), Estimation of irrigation requirement for sustainable water resources reallocation in North China, *Agricultural water management*, 97(11), 1711–1721.

References

- Yeh, P., S. Swenson, J. Famiglietti, and M. Rodell (2006), Remote sensing of groundwater storage changes in Illinois using the Gravity Recovery and Climate Experiment (GRACE), *Water Resources Research*, 42, W12,203, doi:10.1029/2006WR005,374.
- Yi, S., and W. Sun (2014), Evaluation of glacier changes in high-mountain asia based on 10year grace r105 models, *Journal of Geophysical Research: Solid Earth*, 119(3), 2013JB010,860.
- Zektser, I., and G. Everett Lorne (2004), Groundwater resources of the world: and their use, *Tech. rep.*, UNESCO IHP-VI Series on Groundwater No 6, UNESCO, Paris, France.
- Zeng, N., J.-H. Yoon, A. Mariotti, and S. Swenson (2008), Variability of basin-scale terrestrial water storage from a PER water budget method: The Amazon and the Mississippi, *Journal of Climate*, 21(2), 248–265.
- Zhang, K., L. L. Ge, X. J. Li, and A. H. M. Ng (2013), Monitoring ground surface deformation over the north china plain using coherent alos palsar differential interferograms, *Journal of Geodesy*, 87(3), 253–265.
- Zhang, Z. J., and Y. H. Fei (2009), *Atlas of groundwater sustainable utilization in North China Plain*, China Cartographic Publishing House, Beijing.
- Zhang, Z. Z., B. F. Chao, Y. Lu, and H. T. Hsu (2009), An effective filtering for grace time-variable gravity: Fan filter, *Geophysical Research Letters*, 36, L17,311, doi:10.1029/2009GL039,459.
- Zhong, M., J. Duan, H. Xu, P. Peng, H. Yan, and Y. Zhu (2009), Trend of china land water storage redistribution at medi- and large-spatial scales in recent five years by satellite gravity observations, *Chinese Science Bulletin*, 54(5), 816–821.
- Zhuang, W., S.-P. Xie, D. Wang, B. Taguchi, H. Aiki, and H. Sasaki (2010), Intraseasonal variability in sea surface height over the south china sea, *Journal of Geophysical Research: Oceans*, 115(C4), C04,010.

VITA

FENG Wei was born in Xuzhou, Jiangsu Province of P. R. China on 18 October 1984, the son of FENG Chaoxuan and ZHOU Baohong. He received his Bachelor of Engineering degree in Surveying Engineering from Hohai University, Nanjing in 2007. In September of 2007, Wei began his graduate studies at the Graduate University of Chinese Academy of Sciences, Peking. In 2009, he became a PhD candidate at the Institute of Geodesy and Geophysics, Wuhan. While in Wuhan he met LU Jianshuang, whom he married in 2014. In 2011, he became a joint PhD candidate between the Institute of Geodesy and Geophysics and the Paul Sabatier University, supported by the Sino-French Joint PhD Scholarship Program. Wei's research has appeared in *Water Resources Research* and *Journal of Geodynamics* and has been presented at meetings of the American Geophysical Union and the European Geosciences Union, among others.

Permanent address: 340 Xudong Road, Wuhan, China, 430077

This dissertation was typed with L^AT_EX[†] by the author.

[†]L^AT_EX is a document preparation system based on Donald E. Knuth's T_EX typesetting language.

